Investigation of New Devices and Characterization Techniques in the III-V Semiconductor System

Thesis by

Xiao-chang Cheng

In Partial Fulfillment of the Requirements

for the Degree of

Doctor of Philosophy

California Institute of Technology

Pasadena, California

1999

(Submitted May 4, 1999)

To my parents

Acknowledgements

I am grateful to my advisor, Tom McGill, for having faith in me and providing numerous opportunities throughout my graduate career. Over the years, I have come to appreciate Tom's incredible sharp instincts for finding interesting research directions and his ability to accommodate a diverse group of talented individuals. I am constantly amazed by his flexibility and yet hold great admiration for the instances when he stuck to the principles. If I showed up years ago at the door of graduate school with scarcely any idea about "state of the art" research operations, Tom is the person who changed that.

I have benefited tremendously from my associations with former and current members of the McGill group. I am indebted to Doug Collins and David Chow for showing me the art of molecular beam epitaxy. Doug has been my initiation to the world of experimental semiconductor physics whereas David is the consummate professional and a role model for any aspiring young researcher. I am also grateful to Andy Hunter and Gerry Picus. Without their guidance, much of the avalanche photodiode work in this thesis would not have been possible. I have to thank Erik Daniel for riding out the frustration in antimonide processing together and laying down the foundation work for the tunnel switch diode simulation. Erik is one of the most generous people around and I have picked up many things from him, not the least of which is a taste for Jackie Chan movies. I must also thank Rob Miles for introducing me to the world of scanning probe microscopy. Rob built the ballistic electron emission microscopy set-up described in this thesis, which enabled much of the ensuing characterization work. I would also like to thank David Ting, who has been a constant influence in the group and has reached out to me on numerous occasions. Ogden Marsh and Jim McCaldin have also had a constant presence in the research background. Ogden has provided many useful tips and his sunny disposition has been infectious. Over the years, I have also enjoyed interactions with group members Harold Levy, Yixin Liu,

Ron Marquardt, Johanes Swenberg, Mike Wang, Peo Petterson, and Chris Springfield.

Among current members of the McGill group, I am most grateful to Eric Piquette for his gentlemanly manner, which I came to admire during our co-tenure in the clean room. I have enjoyed my collaborations with Alicia Alonzo and appreciated very much her defensive stand for the III-V MBE system. Zvonimir Bandic has been a reliable source of enthusiasm and his openness has been refreshing. I am also grateful to fellow Canadian Paul Bridger, who has been the optics guru in the group and provided numerous experimental advices. I have also benefited from my associations with the younger graduate students, including Joe Jones, Bob Beach, Cory Hill, Xavier Cartoixa, Matthew Barton, and Rob Strittmatter. Cory has been very helpful as the group system administrator and is always on the spot when computer difficulties arise. Xavier is responsible for the simulation work in the tunnel switch diode part of this thesis, while Matt has contributed towards the characterization of the TSD devices. I hope greater things lay ahead for this talented bunch of individuals.

I would like to thank Marcia Hudson, Gloria Pendlay, and Tim Harris for their excellent administrative work. I would also like to acknowledge the National Science and Engineering Research Council of Canada for providing financial support during my stay at Caltech. Many thanks go back to Bob Fedosejevs and Jim McMullin for opening the door of research to me during my undergraduate days at the University of Alberta.

I would like to thank Jiang Wen and Xu Weihua, whose friendship I will always treasure. Special thanks must go to Song Yang, who has changed my life at Caltech. Without her love and support, this thesis would not have been possible. Finally, I would like to thank my parents and sister. Their unconditional, unbounded love and support have been a true blessing.

List of Publications

Work related to this thesis has been or will be presented in the following papers:

Tunnel Switch Diode Based on AlSb/GaSb Heterojunctions,
X-C. Cheng, X. Cartoixà, M. A. Barton, C. J. Hill, and T. C. McGill, submitted to Applied Physics Letters.

Near Infrared Avalanche Photodiodes with $Al_{0.04}Ga_{0.96}Sb$ and GaSb/AlSb Superlattice Gain Layers,
X-C. Cheng and T.C. McGill, submitted to the Journal of Applied Physics.

Molecular Beam Epitaxy Growth of Antimonide Avalanche Photo Detectors with InAs/AlSb Superlattice as the n-type Layer,
X-C. Cheng and T.C. McGill, to be published in the Journal of Crystal Growth.

Avalanche Photo Detectors in the InAs/GaSb/AlSb Material System by Molecular Beam Epitaxy,
X-C. Cheng and T.C. McGill, SPIE International Symposium on Optoelectronics, 1999.

Ballistic Electron Emission Microscopy Spectroscopy Study of AlSb and InAs/AlSb Superlattice Barriers,
X-C. Cheng and T.C. McGill, Journal of Vacuum Science and Technology B **16**, pp 2291-2295, 1998.

Mapping of $Al_xGa_{1-x}As$ Band Edges by Ballistic Electron Emission Spectroscopy,
X-C. Cheng, D. A. Collins, and T.C. McGill, Journal of Vacuum Science and Technology A **15**, pp 2063-2068, 1997.

Work not included in this thesis has been or will be presented in the following papers:

Strain in wet thermally oxidized square and circular mesas,
A.C. Alonzo, X-C. Cheng, and T.C. McGill, in preparation.

Effect of cylindrical geometry on the wet thermal oxidation of AlAs,
A.C. Alonzo, X-C. Cheng, and T.C. McGill, Journal of Applied Physics **84**, pp. 6901-6905, 1998.

Abstract

This thesis concerns the investigation of novel devices and material characterization techniques in the III-V semiconductor system. In the first part of the thesis, we demonstrate that novel devices, such as avalanche photodiodes and tunnel switch diodes, can be fabricated from InAs/GaSb/AlSb heterostructures by molecular beam epitaxy (MBE). In the second part of the thesis, ballistic electron emission microscopy (BEEM) is employed to examine the local band offset in these heterostructures, which is often found to be crucial in device design.

In the avalanche photodiode study, devices with near infrared response out to 1.74 μm were demonstrated. Two types of devices were investigated: those with a bulk $Al_{0.04}Ga_{0.96}Sb$ multiplication region and those with a GaSb/AlSb superlattice multiplication region. Both types of devices were implemented in a MBE grown p^-n^+ structure that uses a selectively doped InAs/AlSb superlattice as the n-type layer. This particular structure was optimized through several design, fabrication, characterization cycles. It was found that the photodiode dark current depended critically on the InAs/AlSb superlattice period and the resulting band offset at the p^-n^+ heterojunction. The InAs/AlSb superlattice was henceforth optimized by using a three stage design. The ionization rates in bulk multiplication layer devices were measured and found to be consistent with hole impact ionization enhancement in $Al_{0.04}Ga_{0.96}Sb$. However, direct comparison with superlattice multiplication layer devices revealed the latter to be more promising due to more effective dark current suppression from the larger band gap of the superlattice multiplication layer.

The second device studied is the tunnel switch diode. We have fabricated the first such device in the antimonide material system and obtained characteristic "S" shaped I-V curves from these devices. The epilayer and barrier dependence of tunnel diode switching were studied and found to deviate significantly from the punch-through model of operation. In addition, the device I-V curve was observed to "hop" between

two branches when subjected to high levels of stress. We speculate that this was due to instability associated with mobile charges in the AlSb tunnel barrier. A computer model was used to simulate the device behavior and generated results consistent with the observed dependence of switching on tunnel barrier thickness.

In the second part of the thesis, III-V heterostructures were characterized by using ballistic electron emission microscopy (BEEM). BEEM images were shown to reveal sub surface features in $Al_xGa_{1-x}As$ epilayers, whereas BEEM spectroscopy was used to map out the shift in Γ, X, and L band edges with material composition in $Al_xGa_{1-x}As$. BEEM spectroscopy was also applied to device relevant antimonide heterostructures such as AlSb barriers and InAs/AlSb superlattices. It was found that electron transport in AlSb was dictated by the conduction band minium near the X point, and there is large local variation in the AlSb Schottky barrier height. These results were in good correlation with the observed barrier characteristics of AlSb. Due to the small bandgap of InAs/AlSb superlattice and the associated high level of noise current, only the shortest period superlattice was examined by BEEM. The resulting band offset agreed with the calculated value and demonstrated that BEEM spectroscopy can be applied to structures with a large number of hetero-interfaces.

Contents

List of Figures

List of Tables

Chapter 1 Introduction

1.1 Thesis Overview

This thesis concerns the investigation of novel devices and material characterization techniques in the III-V semiconductor system. The bulk of the work is carried out in the lattice matched InAs/GaSb/AlSb system, where new device possibilities arise from the unique broken gap band alignment of InAs/GaSb and the small bandgaps of these materials. In the first part of the thesis, we demonstrate that novel devices, such as avalanche photodiodes and tunnel switch diodes, can be fabricated from InAs/GaSb/AlSb heterostructures by molecular beam epitaxy (MBE). In the second part of the thesis, ballistic electron emission microscopy (BEEM) is employed to examine the local band offset in these heterostructures, which is often found to be a crucial factor in device design.

The antimonide avalanche photodiode forms a major part of the device study. This is an interesting device due to its near infrared responsivity, ionization ratio enhancement possibilities and integration potential. The design, growth, fabrication, and characterization procedures are covered in detail in Chapters 2, 3, and 4, which also serve to illustrate the background work common to subsequent heterostructure studies. Two types of avalanche photodiodes will be described: those with a bulk $Al_{0.04}Ga_{0.96}Sb$ multiplication region and those with a GaSb/AlSb superlattice multiplication region. Both types of devices were implemented in a MBE grown p^-n^+ structure that used a selectively doped InAs/AlSb superlattice as the n-type layer. This particular structure was refined through several design, fabrication, characterization cycles. It was found that the photodiode dark current depended critically on the InAs/AlSb superlattice period and the resulting band offset at the p^-n^+ heterojunction. The InAs/AlSb superlattice was henceforth optimized by using a three stage design.

The ionization rates in bulk $Al_{0.04}Ga_{0.96}Sb$ multiplication layer devices were measured by using a two wavelength photo response scheme. The results were consistent with hole impact ionization enhancement in $Al_{0.04}Ga_{0.96}Sb$. However, the ionization enhancement advantage was largely compromised by the high level of dark current found in the bulk device. In comparison, the superlattice multiplication devices was deemed more promising because the dark current was more effectively suppressed by barriers in the superlattice multiplication region while impact ionization may still be enhanced by separate band offset adjustment.

The tunnel switch diode is the second antimonide device studied. Compared to the avalanche photodiode, this is a much simpler device from a fabrication standpoint. Yet it's no less interesting due to its unique "S" shaped current-voltage (I-V) characteristics. In Chapter 5, we demonstrate first time measurement of such I-V behavior from an antimonide heterostructure. The epilayer and barrier dependence of tunnel diode switching were studied and found to deviate significantly from the punch-through model of operation. In addition, the devices exhibited "hopping" between two current voltage branches when subjected to high levels of stress. We speculate that this is due to instability associated with mobile charges in the AlSb tunnel barrier. A computer model was used to simulate the device behavior and generated results consistent with experimental findings about the barrier thickness dependence of switching.

The rest of the thesis (Chapters 6, 7 and 8) concerns the characterization of III-V heterostructures by BEEM, which is a scanning tunneling microscopy (STM) based technique capable of imaging the buried surface and yielding local band structure information. The $Al_xGa_{1-x}As$ system was studied first as a testing ground for the technique (Chapter 7). BEEM imaging was shown to reveal sub surface features in $Al_xGa_{1-x}As$ samples, while BEEM spectroscopy was used to study the local variation of Γ, X, and L band edges in $Al_xGa_{1-x}As$. The shift in these band edges with material composition was also mapped out by using BEEM spectroscopy.

Following the $Al_xGa_{1-x}As$ study, BEEM was applied to device relevant antimonide heterostructures such as AlSb barriers and InAs/AlSb superlattices (Chapter 8). The

Al on AlSb Schottky barrier height was measured and found to be dictated by the conduction band minimum near the X point. The barrier height exhibited a large local variation, in correlation with the observed barrier characteristics of AlSb. Due to the smaller bandgap of InAs/AlSb superlattices and the associated high level of noise current, only the shortest period superlattice was examined by BEEM. The resulting band offset agreed with the calculated value and demonstrated that BEEM spectroscopy can be applied to structures with a large number of hetero-interfaces.

1.2 Motivation

1.2.1 InAs/GaSb/AlSb system

The motivation for this thesis study grew out of the versatility of III-V semiconductor heterojunction systems. Compared to the Si system, which has been extensively developed and enjoys a much more mature technology base, the III-V system derives its advantages from the compound nature of its constituent material. The unique properties of these materials, i.e., direct bandgap, high carrier mobility, can be tailored to specific applications through bandgap engineering techniques.

To date, most of the III-V research efforts have focused on the lattice matched $Al_xGa_{1-x}As$ system, which has yielded commercial injection lasers [1] and high speed transistors [2]. As part of this thesis study, the band structure of the $Al_xGa_{1-x}As$ system was characterized on a local scale by using ballistic electron emission microscopy (BEEM). The major part of the thesis, however, is devoted to the less well known system of InAs, GaSb and AlSb, which share a common lattice constant at around 6.1 Å.

The versatility of this system can be seen by examining Fig. 1.1(a), which shows the band alignment of various component materials. The most striking feature in this diagram is the presence of broken gap type II band alignment in addition to the type I band alignment found in the $Al_xGa_{1-x}As$ system. The unique heterojunction band offset between InAs and GaSb has resulted in a resonant inter band tunneling

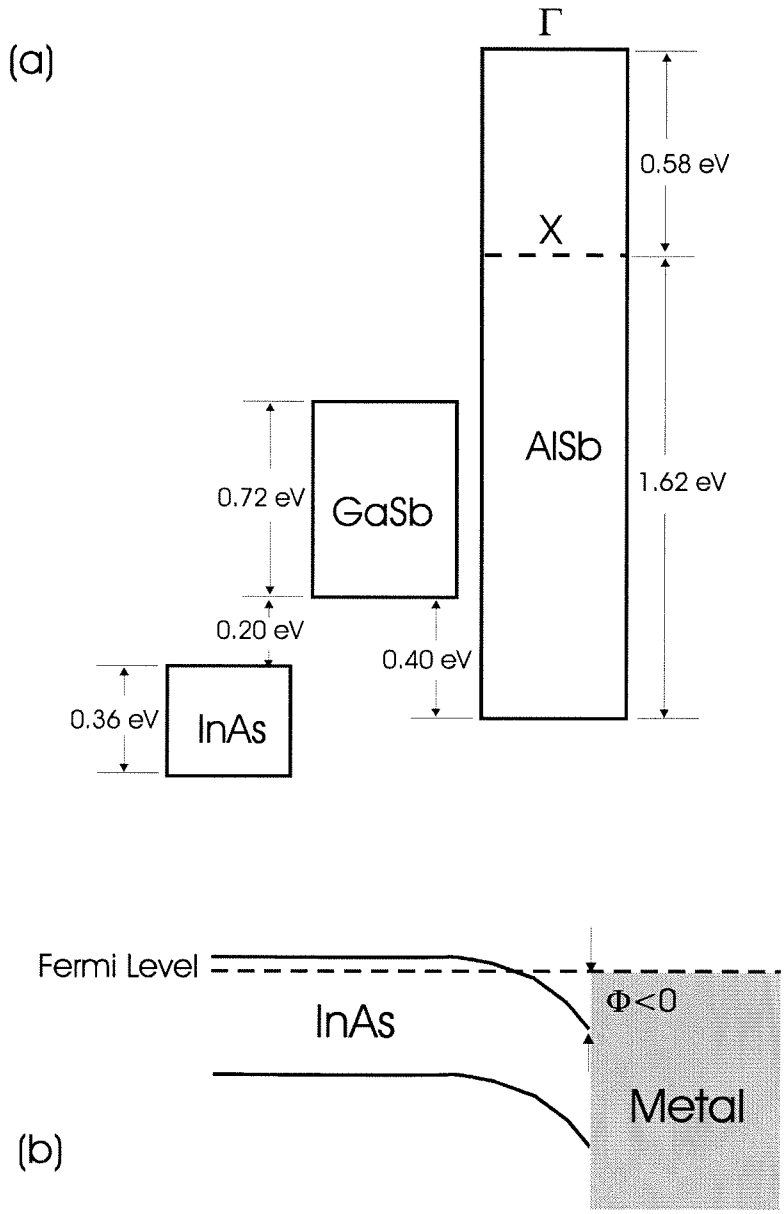

Figure 1.1: InAs/GaSb/AlSb lattice matched system. (a) Band alignment. (b) Negative Schottky barrier between InAs and metal.

(RIT) diode with oscillations up to 712 GHz [3]. In addition to the wide variety of band offsets available, these materials have a number of advantages: InAs has the unusual property of forming a negative Schottky barrier when brought in contact with most metals (Fig. 1.1(b)) [4]. Hence it makes an ideal contacting material. It also has a small effective mass ($0.025m_{electron}$) [5], which implies that a stronger quantum confinement effect can be achieved in RIT type applications. Moreover, AlSb has a large bandgap (2.2 eV at the Γ point and 1.6 eV at the conduction minimum near the X point [5]) and can be used as a barrier in many device structures.

Besides the aforementioned quantum effect devices, the single biggest application for the antimonide material system is in the area of infrared sources and detectors. This is in large part due to the small bandgaps of InAs, GaSb, their alloys and superlattices. The most significant developments in this area include InAs/GaSb quantum cascade lasers, which achieve high quantum efficiency because non-radiative recombination due to phonon scattering is suppressed from the type II band alignment [6]. There are also reports of injection lasers [7] in the mid infrared wavelength range and far infrared detectors based on InAs/InGaSb superlattices [8].

While the antimonide material system have distinct advantages in many of these applications, it is also plagued by the immaturity of the technology and a relative lack of understanding on certain materials issues. For example, carrier transport in AlSb is not well understood. While AlSb is an adequate barrier in RIT type structures, it is too leaky as the gate insulator in a three terminal transistor configuration [9]. The challenges in antimonide research thus lie in two directions:

1. Study of new devices that exploit the unique band offset and intrinsic material property of the system.

2. Characterization of the basic material properties in a setting relevant to advancement of device research.

The thesis study therefore is a reflection of attempts to address both of these issues. The main body of the thesis is accordingly split into two part. The first part of the

thesis describes the design, fabrication, and characterization of two new devices in the antimonide system: an avalanche photodiode with response in the near infrared for night vision, and a tunnel switch diode based on AlSb barriers and GaSb pn junctions. Both devices rely on molecular beam epitaxy (MBE) as the fabrication method and employ heterostructures for advantages. It will be seen that basic material issues such as heterojunction band offset and transport mechanism through barriers are keys to the operation of these devices. These issues are examined in great detail in the second part of the thesis, where ballistic electron emission microscopy is employed to study local transport in device-like heterostructures.

1.2.2 Antimonide Avalanche Photodiode

There is much interest in making a near infrared avalanche photodiode in the antimonide system. This is in part due to the narrow bandgap of GaSb, which at 0.72 eV corresponds to a long wavelength cut off of 1.7 μm. By incorporating indium in the GaSb light absorption region, the sensitivity range of the antimonide photodiode can be easily extended to beyond 2.0 μm. Aside from obvious communication applications at the 1.55 μm wavelength, such extended response in the near infrared fills the special niche of night vision.

This can be seen by examining the night spectrum. In a simplified view, there are three natural contributions to the night glow aside from the highly variable human light source: lunar light, star light, and air glow due to transitions of atmospheric ions [10]. The lunar light spectrum is shown in Fig. 1.2. Since it is in fact reflected sunlight, the spectrum resembles that of a 3000 K black body. The star light can also be thought of as agglomerated black body spectrums with temperatures that range from 2000 K to 23000 K. Due to absorption of the atmosphere, the available radiation can be divided roughly into several bands [10]. The absolute intensity of these bands and the relative contributions from the different sources are highly variable depending on the seasonal and weather ambient. An estimate of the average numbers is shown in Table 1.1.

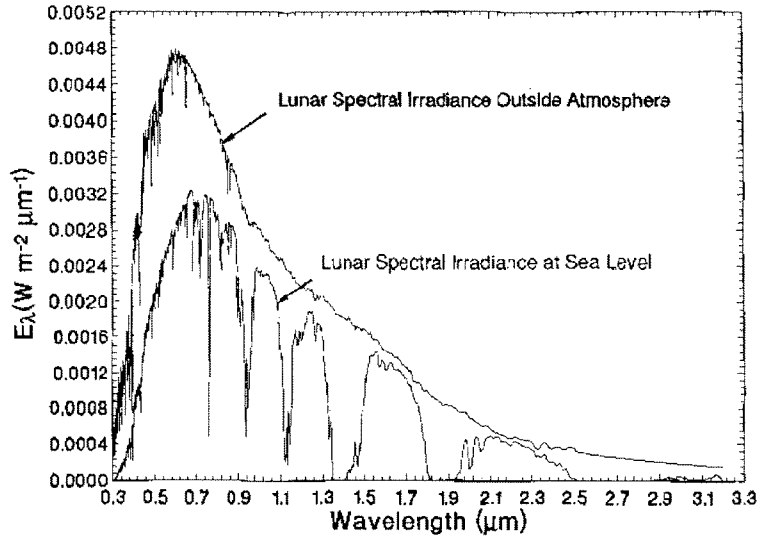

Figure 1.2: Spectrum of lunar light.

It can be seen that there are two bands centered around the wavelength of 1.6 μm and 2.1 μm, which would be captured by an antimonide near infrared photodiode [10]. Further examination of Table 1.1 reveals that the signal in these bands are rather faint. For a detection pixel with a size of 30 μm by 30 μm, an integration time of 30 μs, and a F number of 1, the incident optical power on the pixel front end is on the order of 10^{-12} W. The miniscule amount of power necessitates use of photodetectors of high sensitivity, such as a photo multiplier or its solid state equivalent - the avalanche photodiode.

The antimonide is a good candidate for such a device due to a number of system and materials advantages. Compared to conventional InP based avalanche devices, which fall in the same wavelength range and have been extensively developed for telecommunication applications, the antimonide avalanche photodiode has a distinct advantage in terms of integration potential: by building the antimonide avalanche photodiode on the same chip as an InAs/InGaSb far infrared photodetector [8], it will be possible to create a compact, robust system with multi-color response ideally suited for military type night vision applications.

On the materials level, GaSb has been shown to have larger ionization coefficients

Table 1.1: Intensity of lunar light, star light, and night air glow in the different bands [10].

Band	λ Peak	$\Delta\lambda$	Moon	Star	Night Airglow
	[μm]		[Photons/cm^2·sec]		
1	0.58	0.49	5.83×10^{11}	1.21×10^{9}	4.12×10^{7}
2	1.00	0.16	1.83×10^{11}	1.24×10^{8}	
3	1.24	0.21	2.09×10^{11}	1.15×10^{8}	
4	1.59	0.29	1.99×10^{11}	8.67×10^{7}	4.48×10^{10}
5	2.10	0.43	1.37×10^{11}	6.02×10^{7}	2.24×10^{10}

than InP [11], which will allow the device to have a thinner multiplication region for faster response. More importantly, there has been some experimental evidence and theoretical conjecture that hole ionization in AlGaSb is enhanced when the spin-orbit split-off band difference Δ equals the energy bandgap E_g [12]. This is complemented by the possibility that electron ionization may be enhanced in GaSb/AlGaSb superlattices due to band offset differences [13]. As will be discussed in detail in Chapter 2, the enhanced ionization rate is the single most important property for avalanche operation. It leads to better gain-bandwidth product, smaller excess noise factors, and reduction of microplasmas which are detrimental to the stability of the avalanche action [14].

To date, there have been a number of studies on antimonide avalanche photodiodes, all of which have relied on liquid phase epitaxy (LPE) as the crystal growth method and focused on hole impact ionization enhancement in bulk AlGaSb [12, 16, 15]. The results of these studies indicate a lack of consensus about the resonant hole ionization effect. Hence there is much incentive for a new study with molecular beam epitaxy (MBE) as the device fabrication method. The flexibility of the MBE technique will allow exploration of antimonide avalanche photodiodes with both bulk and superlattice gain mediums. This should further clarify the ionization enhancement issue and maximize the potential of the device through comparison

of the bulk and superlattice approaches.

1.2.3 Antimonide Tunnel Switch Diode

The motivation for the antimonide tunnel switch diode grew out of the need for a two terminal device that has an "S" shaped I-V curve. The usefulness of antimonide electronics depend on high speed operation and possible reduction of circuit complexity from non-linear elements. Since there already exists an antimonide RIT diode with "N" shaped I-V characteristics [17], a new "S" shaped I-V device would complement the RIT device as its circuit dual and enable a wider variety of circuit applications.

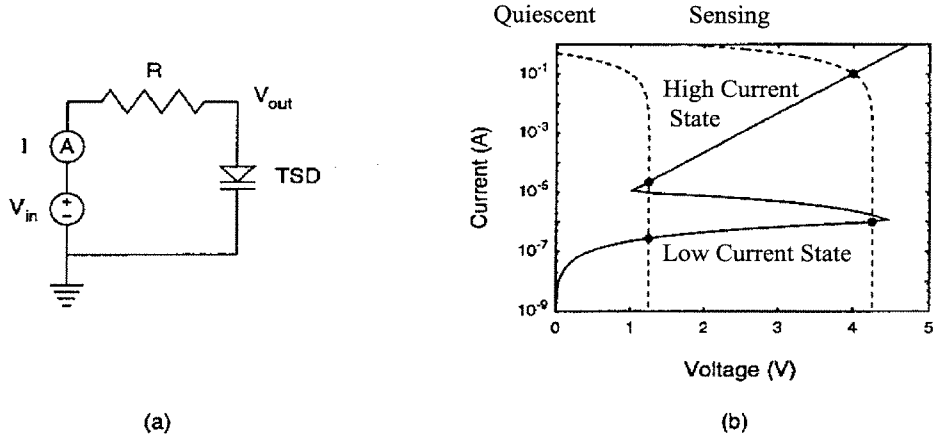

Figure 1.3: Transistorless static random access memory from a tunnel switch diode. (a) Circuit schematic. (b) Load line analysis.

Of particular interest is a transistorless static random access memory (SRAM) element that can be fabricated from the tunnel switch diode alone [18]. Fig. 1.3 shows the basic implementation of this scheme. The memory effect derives from the existence of a high and a low current branch in the I-V characteristics. The logic of the state is read out from the current disparity as the Load line shifts to high voltages. Writing is accomplished by a large voltage swing that switches the TSD to a particular state. Such a memory element would be very fast due to the tunneling nature of the switching. Compared to conventional implementations which requires six transistors per memory cell, the tunnel switch diode element is extremely compact due to its simplicity.

The antimonide tunnel switch diode can also act as the testing ground for tunnel switch diode theory and provide an opportunity to study AlSb barriers in a device setting. While the basic principle of tunnel switch diode is known, its actual operation is highly dependent on the role of the tunnel barrier, which is not well understood. This has been a long standing problem in the silicon implementation of the device [19]. By replacing the SiO_2 tunnel barrier with AlSb, which has a different barrier height and may have deep traps within its bandgap [20], it is hoped that more experimental evidence will be collected to shed light on the role of the tunneling barrier in TSD operation.

1.2.4 Ballistic Electron Emission Microscopy

From the device section of this thesis, it will be seen that basic heterojunction properties such as band offset and Schottky barrier height play prominent roles in device design and often dictate whether or not the device is feasible. While these properties can be ascertained from conventional characterization techniques such as X-ray photoelectron spectroscopy (XPS), photo electric, I-V, and C-V measurements, the results are usually laterally averaged over the whole interface or at least over macroscopic dimensions of more than a few μm. In contrast, ballistic electron emission microscopy (BEEM) provides local mapping of these properties with a theoretical resolution limit as low as 10 Å [21, 22].

The BEEM technique is illustrated in Fig. 1.4. The high resolution of BEEM derives from its scanning tunneling microscopy (STM) origin. By placing a third terminal at the back of the semiconductor sample to collect hot electrons that pass through the buried interface, local electronic properties of the interface can be studied as the STM tip moves to different parts of the surface.

Thus in the second part of this thesis, BEEM is used to investigate semiconductor heterostructures similar to those employed in the device studies. The $Al_xGa_{1-x}As$ system was examined first to clarify ambiguities with regard to its band structure, especially at high Al concentrations. It also served as the testing ground for the

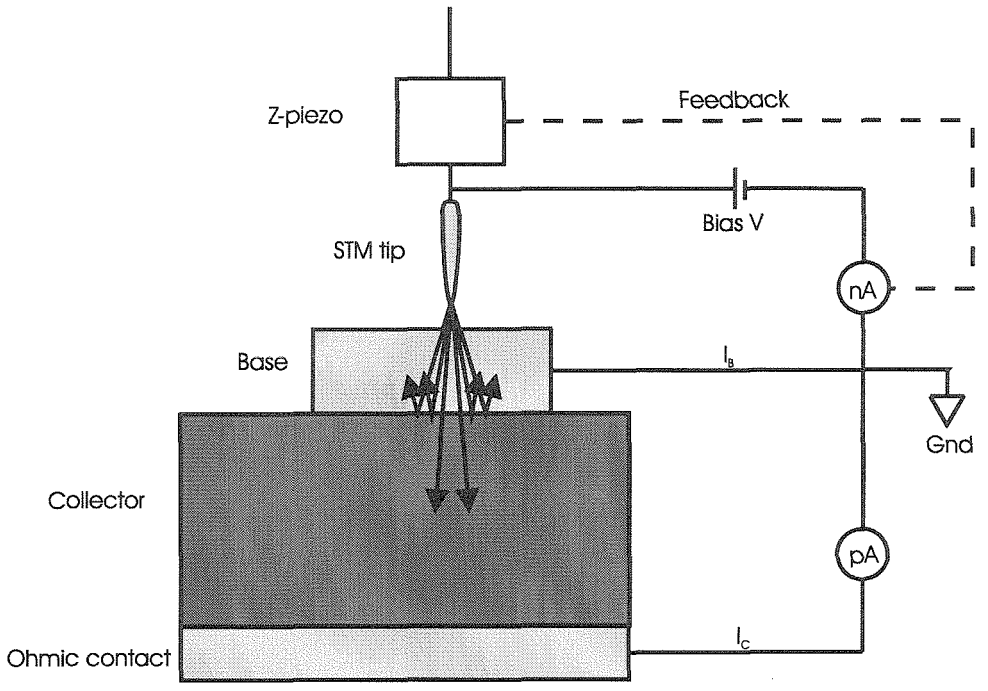

Figure 1.4: Ballistic electron emission microscopy.

BEEM technique so that it can be readily applied to less conventional structures such as the AlSb Schottky barrier or the InAs/AlSb superlattice. The band offset and Schottky barrier information derived from the antimonide study can be applied to device applications, whereas the local variation of these properties are also directly useful as a feed back to the crystal growth process.

1.3 MBE crystal Growth

The underlying link between the device and characterization studies in this thesis is the molecular beam epitaxy (MBE) growth of III-V heterostructures. The flexibility and control inherent to the MBE crystal growth technique is what makes all these studies possible. Since MBE is a well known technique and the detailed growth sequence for each particular structure will be covered in subsequent sections of the thesis, only a few general principles will be outlined below as an introduction.

1.3.1 MBE Environment

Figure 1.5 shows a schematic representation of a MBE machine. The substrate is placed in a fully enclosed steel chamber and surrounded by a number of evaporation crucibles known as Knudsen cells. During growth, the Knudsen cells are heated to specific temperatures so that its elemental content evaporates off at a controlled rate. These elements recombine at the heated, clean substrate surface and fall into the existing crystal template.

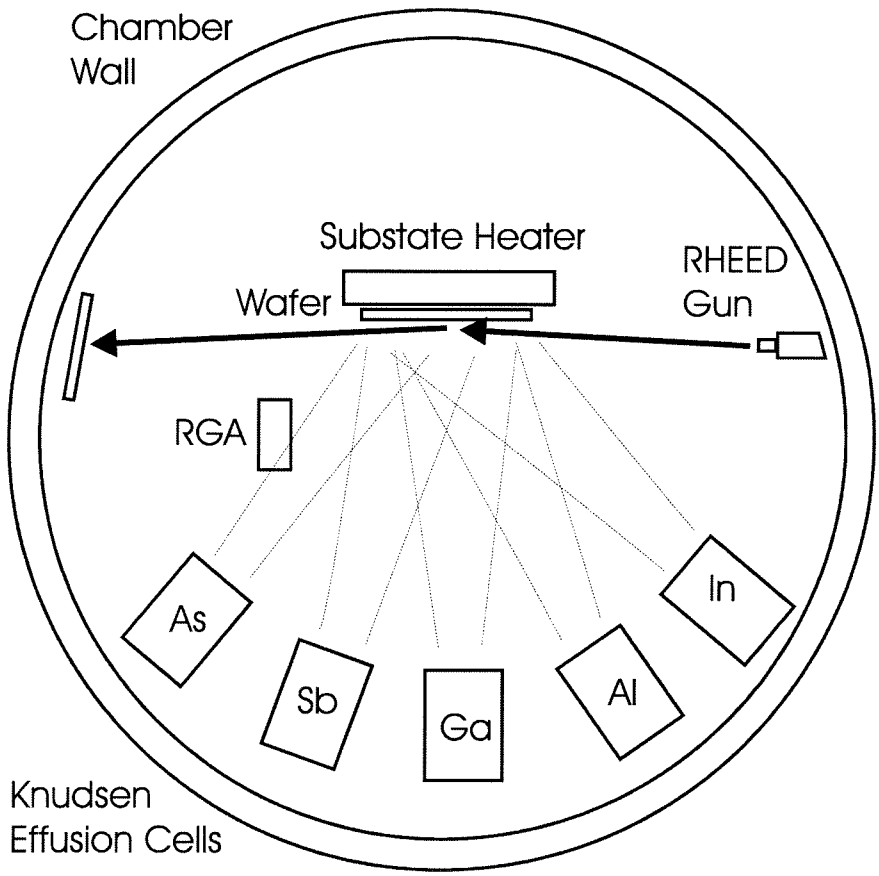

Figure 1.5: Schematic of molecular bean epitaxy set-up.

The distinguishing feature of MBE growth is the stringent requirement it places on the ambient pressure. The background pressure in a well maintained MBE cham-

ber is typically below 10^{-9} Torr. At such a low pressure, it takes several hours for a monolayer of impurities to accumulate on a clean substrate surface [23]. Since the growth rate is on the order of one monolayer per second, MBE allows exquisite control of epilayer thickness. By shuttering the source cells on and off in the correct sequence, atomically sharp interfaces can be achieved. The low background pressure also implies that the mean free path of materials in the growth beam is much larger than the separation between source cells and the substrate. As a result, liquid or gaseous flow patterns do not complicate MBE growth as can be the case in chemical vapor deposition or liquid phase epitaxy. Because of the UHV environment, a number a diagnostic tools can be applied for *in situ* monitoring of the crystal growth process. The most important and commonly available of these are reflection high energy electron diffraction (RHEED) and the residual gas analyzer. As shown in Fig. 1.5, a high energy electron beam (10 keV) is directed at the substrate at a grazing angle in the RHEED set-up. The resulting diffraction pattern provides information on the growth rate, surface reconstruction and morphology of the substrate. This is complemented by the residual gas analyzer which yields information about the chemical species in the growth chamber and can be used to adjust beam fluxes and identify background impurities.

1.3.2 III-V Growth

The MBE growth of semiconductor crystal is optimized by adjusting two main parameters: substrate temperature and source flux. Since III-V compounds preferentially desorb group V elements, the group V flux must be maintained between three to ten times higher than the group III flux to grow a stoichiometric crystal. This ratio increases as the substrate temperature is raised, provided that the temperature does not exceed the "congruent sublimation temperature," at which point the III-V compound becomes unstable [23]. Since the excess V element desorbs, the growth rate is controlled by the III flux and the associated cell temperature. It is generally known that the crystal quality can be improved by using a higher substrate temperature and

minimizing the V flux while still maintaining a V element stabilized growth front [23].

The structures studied in this thesis consisted of GaAs/AlGaAs and InAs/GaSb/AlSb. All of these structures were grown in a Perkin-Elmer 430 MBE chamber equipped with cracked As and Sb cells. The AlGaAs samples were grown on epi-ready (100) GaAs substrate at a substrate temperature of 570 °C, which is slightly below the oxide desorption temperature of GaAs. An As stabilized front was always maintained by keeping a 4×2 RHEED pattern.

Most of antimonide heterostructures were grown on (100) GaSb substrate, which were etched prior to introduction to the UHV environment. The growth temperature for the bulk materials was slightly below the GaSb oxide desorption point at 520 °C, whereas a lower temperature was required for InAs/AlSb superlattice growth in order to reduce cross anion contamination. The RHEED reconstruction patterns for GaSb/AlSb and InAs are 1×3 and 4×2, respectively.

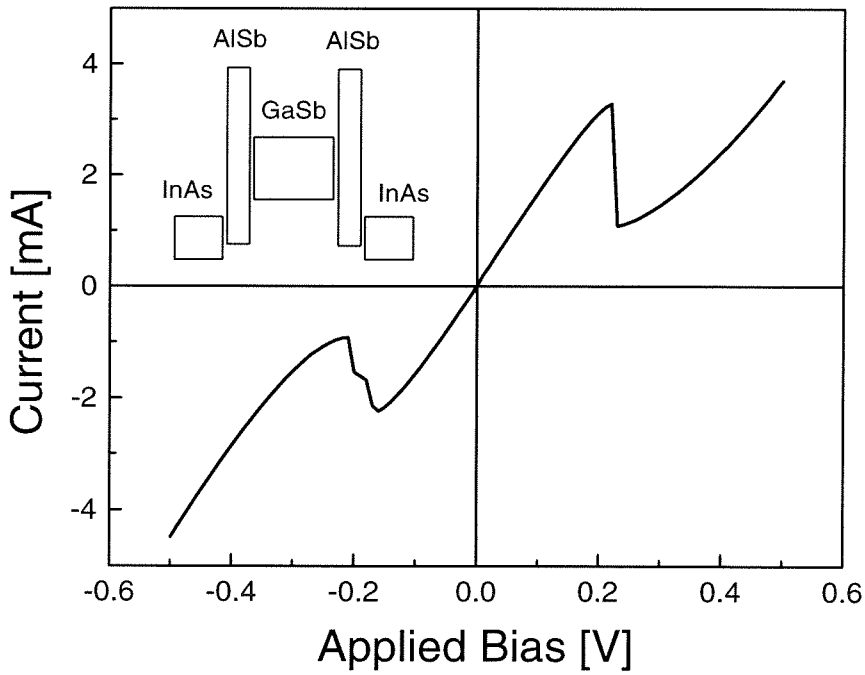

Figure 1.6: Current voltage behavior of antimonide RIT grown on GaAs wafer.

The crystal growth is divided into the arsenide and antimonide groups due to the 8% lattice match between GaAs and GaSb. It is possible, however, to overcome the

lattice match and the resulting misfit dislocations by using a buffer layer [24]. This is demonstrated in Fig. 1.6 which shows the I-V curve of an antimonide RIT diode grown on GaAs substrate. One can also take advantage of the lattice mismatch between these two material systems. As illustrated by the atomic force microscope (AFM) scan in Fig. 1.7, GaSb dots are formed as a result of the surface free energy effect when several monolayers of GaSb are grown on GaAs substrate. Though lacking uniformity, these dots may be a viable way to realize zero dimensional quantum structures. These examples clearly demonstrate the versatility and flexibility of the III-V MBE process.

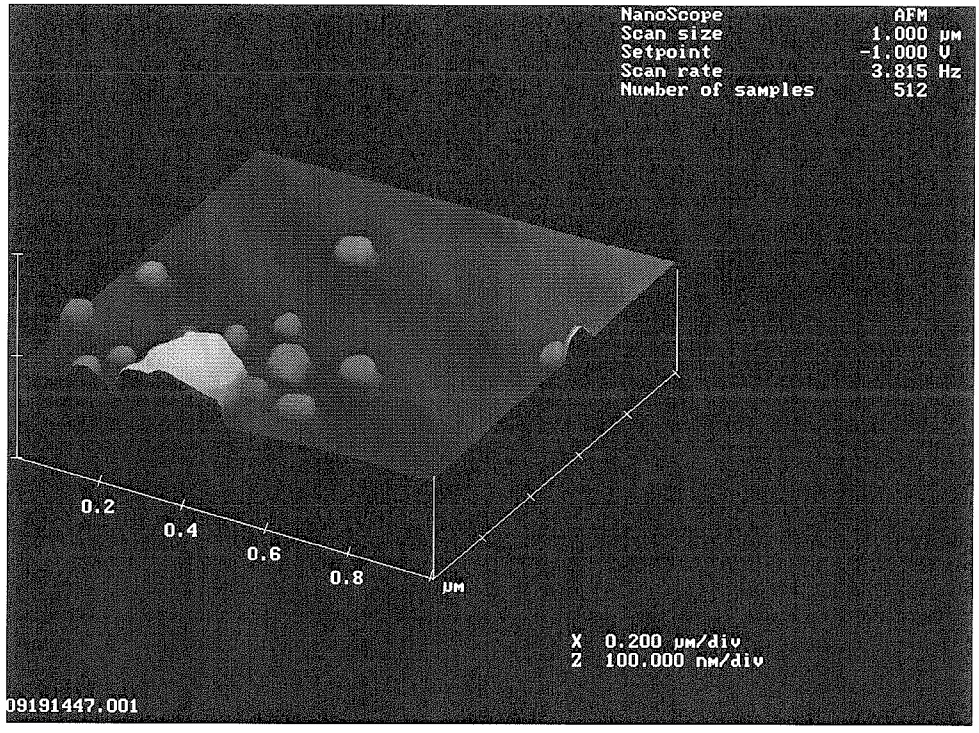

Figure 1.7: AFM scan of dots formed from two monolayers of GaSb deposited on GaAs substrate. Note that the large bright object on the left is a dust particle.

Bibliography

[1] A. Y. Cho and H. C. Casey, Jr., *Appl. Phys. Lett.* **25**, 288 (1974).

[2] M. Abe, T. Mimura, N. Yokoyama, and H. Ishikawa, *IEEE Trans. Electron Devices* **29**, 1088 (1982).

[3] E. R. Brown, J. R. Söderström, C. D. Parker, L. J. Mahoney, K. M. Molvar, and T. C. McGill, *Appl. Phys. Lett.* **58**, 2291 (1991).

[4] A. G. Milnes and A. Y. Polyakov, *Mater. Sci. Engineering* **18**, 237 (1993).

[5] *Semiconductors: Group IV elements and III-V Compounds*, edited by O. Madelung, Spriner-Verlag, Berlin, 1991.

[6] R. Q. Yang and S. S. Pei, *J. Appl. Phys.* **79**, 8197 (1996).

[7] R. H. Miles, D. H. Chow, T. C. Hasenberg, A. R. Kost, and Y-H. Zhang, *Appl. Phys. Lett.* **67**, 3700 (1995).

[8] D. L. Smith and C. Mailhiot, *J. Appl. Phys.* **62**, 2545 (1987).

[9] E. S. Daniel, Thesis, California Institute of Technology, 1997.

[10] G. S. Picus, unpublished, California Institute of Technology, 1997.

[11] F. Osaka, T. Mikawa, and T. Kaneda, *IEEE J. Quantum Electron.* **21**, 1326 (1985).

[12] O. Hildebrand, W. Kuebart, K. W. Benz, and M. H. Pilkuhn, *IEEE J. Quantum Electron.* **17**, 284 (1981).

[13] G. F. Williams, F. Capasso, and W. T. Tsang, *IEEE Trans. Electron Devices* **3**, 71 (1982).

[14] G. E. Stillman and C. M. Wolfe, in *Semiconductors and Semimetals, Volume 12*, edited by R. K. Willard and A. C. Beer, Academic, New York, 1977.

[15] L. Gouskov, B. Orsal, M. Perotin, M. Karin, A. Sabir, P. Coudray, S. Kibeya, and H. Luquet, *Appl. Phys. Lett.* **60**, 3030 (1992).

[16] H. Kuwatsuka, T. Mikawa, S. Miura, N. Yasuoka, Y. Kito, T. Tanahashi, and O. Wada, *Appl. Phys. Lett.* **57**, 249 (1990).

[17] J. R. Söderström, D. H. Chow, and T. C. McGill, *Appl. Phys. Lett.* **55**, 1094 (1989).

[18] H. J. Levy, Thesis, California Institute of Technology, 1995.

[19] P. O. Pettersson, A. Zur, E. S. Daniel, H. J. Levy, O. J. Marsh, and T. C. McGill, *IEEE Trans. Electron Devices* **45**, 286 (1998).

[20] A. Nakagawa, J. J. Pekarik, H. Kroemer, and J. H. English, *Appl. Phys. Lett.* **57**, 1551 (1990).

[21] W. J. Kaiser and L. D. Bell, *Phys. Rev. Lett.* **10**, 1406 (1988).

[22] L. D. Bell and W. J. Kaiser, *Phys. Rev. Lett.* **61**, 2368 (1988).

[23] *The Technology and Physics of Molecular Beam Epitaxy*, edited by E. H. C. Parker, Plenum Press, New York and London, 1985.

[24] J. R. Soderstrom, D. H. Chow, and T. C. McGill, *Mat. Res. Soc. Symp. Proc.* **145**, 409 (1989).

Part I

Novel Devices Based on InAs/GaSb/AlSb Heterostructures

Chapter 2 Avalanche Photodiode Theory

2.1 Introduction to Chapter

The first device investigated in this thesis is the antimonide avalanche photodiode. This chapter describes the basic theory of avalanche photodiode operation and provides the necessary background for the following two chapters. Much of the chapter will be devoted to the importance of impact ionization enhancement, which is the critical factor in avalanche photodiode design and one of the initial driving forces for antimonide avalanche photodiode research. The equally important, and perhaps more practical, subject of dark current suppression is also discussed.

2.2 Basic Operation

The avalanche photodiode consists of a reversed biased pn junction. As shown in Fig. 2.1, incoming photons are absorbed by the semiconductor and generate electron hole pairs. Under high field conditions, these electrons and holes may gain large amount of energy from drift motions in the depletion region. In the so called "impact ionization process," the hot carriers knock off bound electrons upon collision with atoms in the crystal. The end result is that each hot carrier gives up its energy towards the creation of a new electron hole pair. The process repeats itself and the final multiplied current can be several hundred times larger than the initial incoming signal [1].

The signal to noise (S/N) ratio of an avalanche photodiode is given by:

$$\frac{S}{N} = \frac{\frac{1}{2}(q\eta P_0/h\nu)^2 M^2}{2q(I_P F_P + I_D F_D)M^2 B + 4kTB/R} \tag{2.1}$$

where q is the electronic charge, η is the quantum efficiency, P_0 is the incoming signal

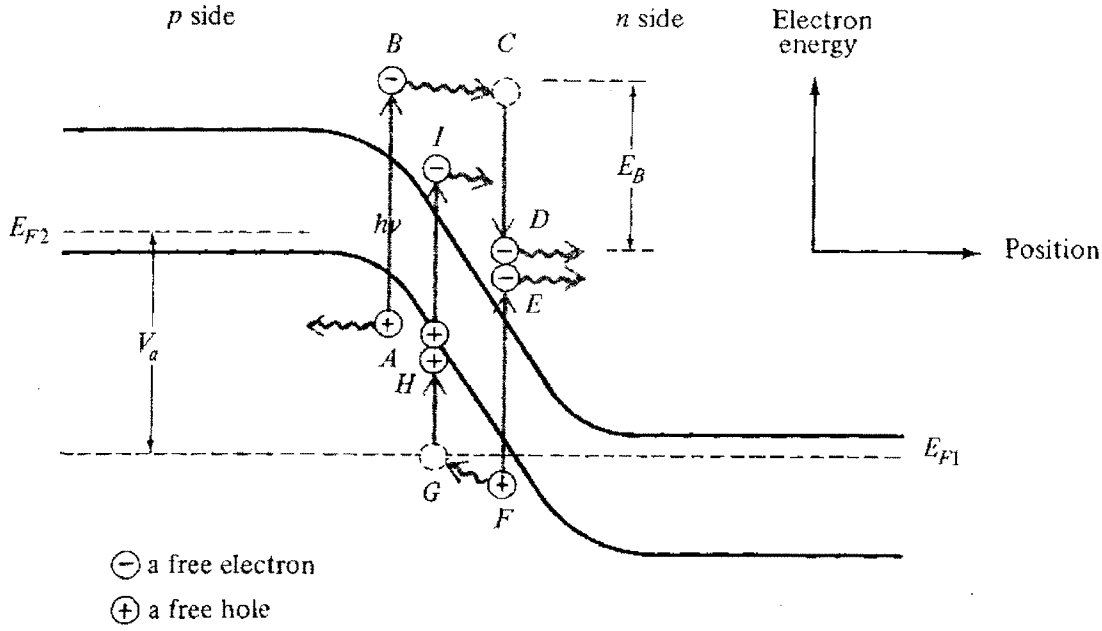

Figure 2.1: Band diagram and basic operation of an avalanche photodiode [1].

power, $h\nu$ is the photo energy, M is the multiplication factor, I_P and I_D are the signal current and dark current, F_P and F_D are the associated excess noise factors, B is the detector band width, kT is the thermal energy, and R is the detector impedance [1]. The larger multiplied signal implies a better S/N ratio and greater detector sensitivity: as the multiplication factor is increased, the Johnson noise term $4kTB/R$ plays a diminished role and the S/N ratio approaches the shot noise limit. However, this is not without penalties. The statistical nature of the avalanche process means that additional noise is introduced as the current is multiplied. This is accounted for by the excess noise factor $F(M)$, which becomes increasingly significant at higher multiplication factors. Thus the avalanche photodiode researcher is concerned about finding ways to reduce the excess noise factor $F(M)$, especially in night vision type applications where high detector sensitivity is desired.

2.3 Impact Ionization Ratio

The side effect due to the statistical nature of the avalanche process is minimized when only one type of carrier dominate the impact ionization process [2]. Hence the most important parameter for the multiplication material is the ratio of electron and hole impact ionization rate (α/β). A large impact ionization ratio will result in more gradual increase of $F(M)$ with multiplication factor M, a higher gain band width product, and reduction of microplama formation, which is detrimental to the stability of avalanche photodiode operation.

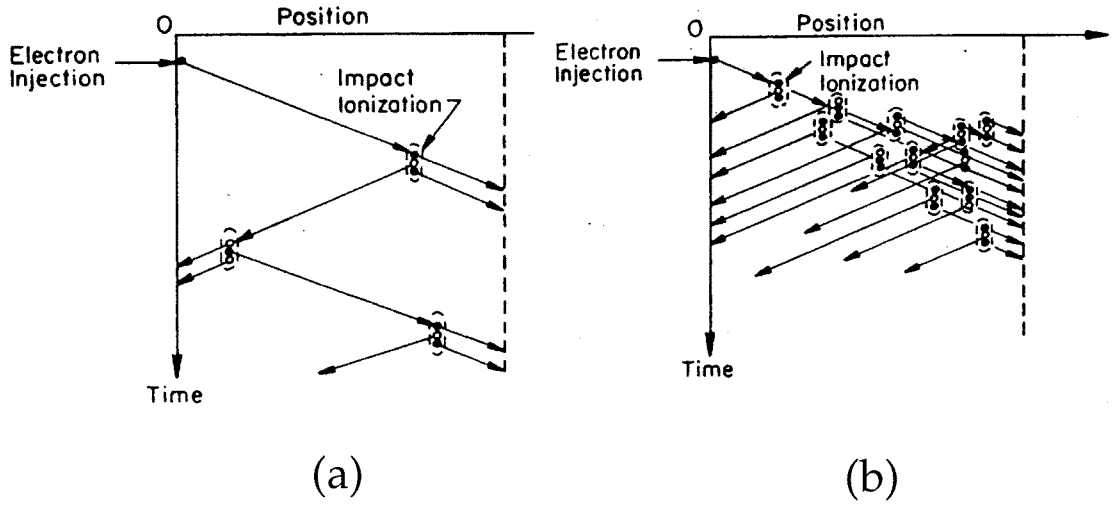

Figure 2.2: Schematic representation of avalanche multiplication process. (a) α=β. (b) β=0.

Intuitively, this can be understood by examining Fig. 2.2, which depicts electrons and holes drifting in opposite directions in the high field region of an avalanche diode. In Fig. 2.2(a), the ionization rates of electrons and holes are equal, whereas in Fig. 2.2(b) only the electrons can impact ionize. Note that the total number of output carriers is the same in both pictures because the gains are the same. To compensate for the lack of hole ionization, the electric field in Fig. 2.2(b) is much higher, which results in higher electron ionization rates and a shorter average ionization path. The process in Fig. 2.2(a) is inherently more noisy and slower because the ionization path has long segments and zig-zags across the depletion region many more times. In

comparison, the ionizations in Fig. 2.2(b) only goes toward one direction and there is much less statistical variation due to the shorter average ionization path.

The mathematics of the avalanche process and resulting dependence of excess noise factor on ionization ratio was first worked out by McIntyre in 1965 [3], whereas the gain bandwidth product dependence was shown to depend critically on impact ionization ratio by Emmons and Lucovsky [4]. The main results of their findings are summarized as follows.

The multiplication factor M is given by

$$M_n = \frac{1}{1 - \int_0^w \alpha exp[-\int_0^x (\alpha - \beta) dx'] dx} \tag{2.2}$$

where w is the width of the depletion region. Note that the electron and hole impact ionization rates α and β are functions of electric field and electron injection from the p side edge ($x = 0$) of the junction is assumed. For hole injection from the n side of the reverse biased pn junction, simply exchange the roles of α and β and change the inner integration limits from $[0, x]$ to $[x, w]$.

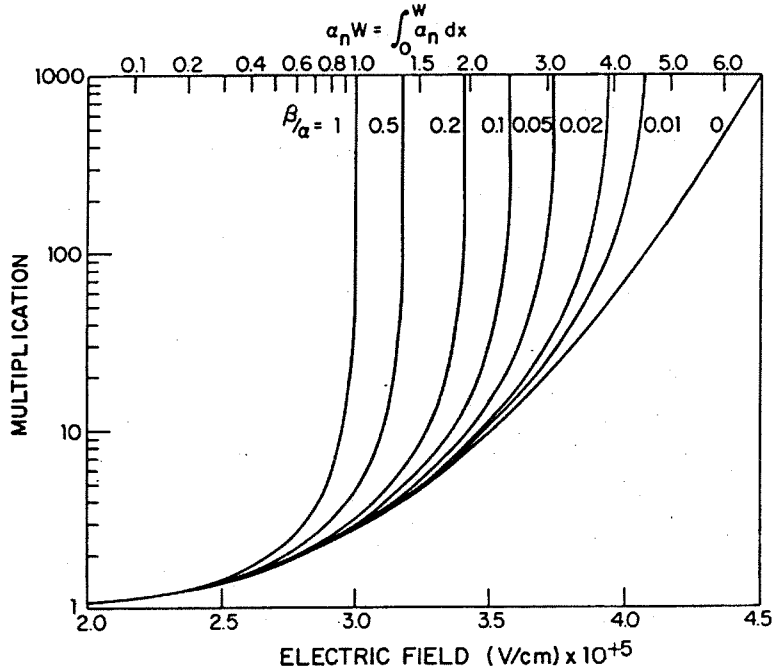

Figure 2.3: Field dependence of multiplication factor for different ionization ratios [5].

The electron multiplication factor is plotted as a function of electric field for various ionization ratios in Fig. 2.3. It can be seen that the multiplication is much more sensitive to the electric field when the ionization rates are nearly equal. Despite high gains at lower field, this is an undesirable scenario because the device is very unstable with respect to field fluctuations which may result from crystal imperfections [5]. In fact, local breakdowns known as "microplasmas" of electrons and holes do form and are detrimental to the noise characteristics of the device [6].

The gain bandwidth product of the avalanche photodiode is given by

$$M\omega = \frac{1}{(W/v_n)(\beta/\alpha)} \tag{2.3}$$

where ω is the cut off frequency, W the depletion width and v_n the saturation velocity of the electron [4]. There is a trade off between gain and bandwidth because the higher gains require more ionization segments (see Fig. 2.2(a)). The resulting extra passage through the depletion region slows down the avalanche process. For the same gain, the device with the higher ionization rate ratio is faster because of the shorter ionization path.

The excess noise factors are given by

$$F_n = M_n((1 - (1 - k)[(M_n - 1)/M_n]^2)) \tag{2.4}$$

$$F_p = M_p((1 - (1 - 1/k)[(M_p - 1)/M_p]^2)) \tag{2.5}$$

where $k = \beta/\alpha$, and M_n and M_p denote electron and hole multiplication factors, respectively [3]. These expressions are plotted in Fig. 2.4 for various values of α/β. Because of the symmetry of these equations in n, p, k, and $1/k$, only one set of curve is required. In this figure, it can be seen that for a low excess-noise factor the electron and hole ionization rates must be greatly different. In addition, the device structure must be designed so that the carrier with the highest ionization rate is injected into the high field region. If the reverse is true, the excess-noise factor will actually be

worse than that for a device with equal ionization rates.

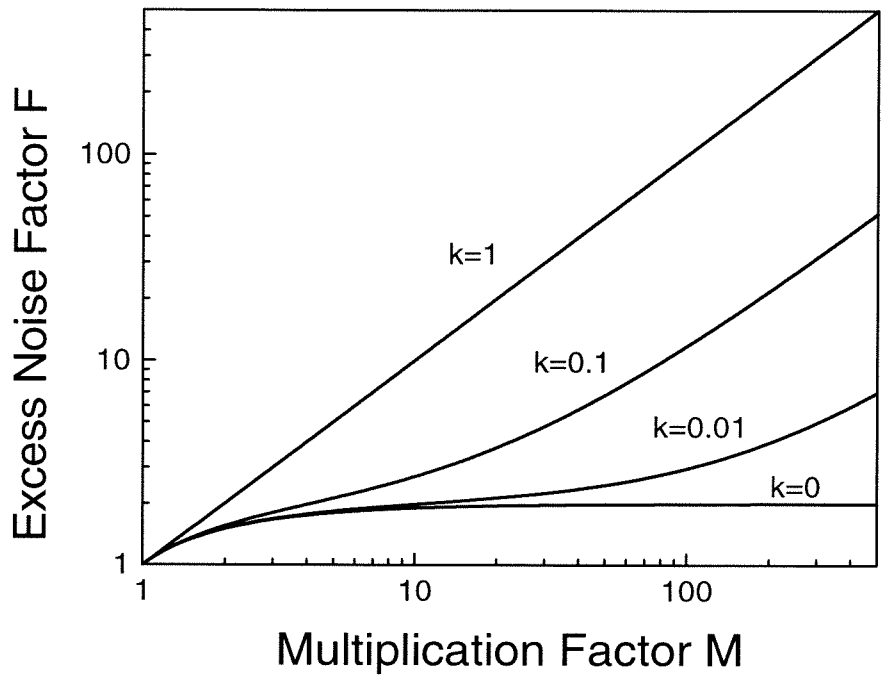

Figure 2.4: Effect of impact ionization ratio on excess noise factor [3].

2.4 Impact Ionization Enhancement

2.4.1 Hole Impact Ionization Enhancement from Spin-orbit Split-off Band Resonance

Much of the interest in antimonide avalanche photodiode is due to the possibility of hole impact ionization enhancement from the spin-orbit split-off band resonance. Such an effect would result in an improved hole to electron impact ionization ratio and better avalanche noise characteristics.

In order to understand this effect, one must take a closer look at the impact ionization process. Figure 2.5 shows an electron initiated impact ionization transition in a band structure exhibiting general features of a zinc blende semiconductor. In the event depicted, an initiating electron makes a transition from state $i(E_i, \mathbf{k_i})$ to

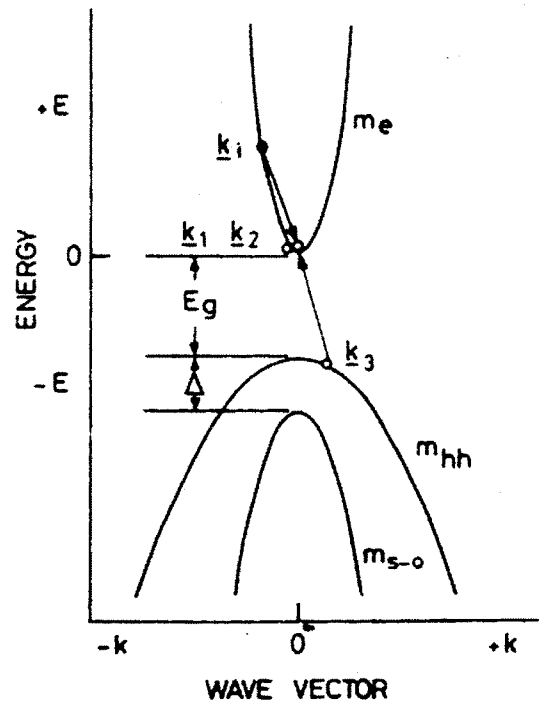

Figure 2.5: Band structure view of an electron initiated impact ionization process [8].

state $1(E_1, \mathbf{k_1})$ promoting an electron to state $2(E_2, \mathbf{k_2})$ and resulting in a hole in the valence band state $3(E_3, \mathbf{k_3})$. A central requirement for this process is conservation of energy. A brief reference to Fig. 2.5 shows that this means that the threshold energy must be at least as large as the bandgap, and one should expect the threshold energy to depend strongly on E_g. Secondly, conservation of momentum must be maintained. Thus the necessary conditions for impact ionization are

$$E(\mathbf{k_i}) = E(\mathbf{k_1}) + E(\mathbf{k_2}) - E(\mathbf{k_3}) \tag{2.6}$$

$$\mathbf{k_i} = \mathbf{k_1} + \mathbf{k_2} - \mathbf{k_3} \tag{2.7}$$

The threshold energy for the process is determined by minimizing the energy of the initial particle with respect to arbitrary variations in the states of the final particles,

subject to the restrictions of conservation of energy and momentum [7]:

$$d\mathbf{k_i} \cdot \nabla_{\mathbf{k}} E(\mathbf{k_i}) = 0 = d\mathbf{k_1} \cdot \nabla_{\mathbf{k}} E(\mathbf{k_1}) + d\mathbf{k_2} \cdot \nabla_{\mathbf{k}} E(\mathbf{k_2}) - d\mathbf{k_3} \cdot \nabla_{\mathbf{k}} E(\mathbf{k_3}) \tag{2.8}$$

$$d\mathbf{k_i} = 0 = d\mathbf{k_1} + d\mathbf{k_2} - d\mathbf{k_3} \tag{2.9}$$

Substituting (2.9) into (2.8) and recognizing $\nabla_{\mathbf{k}} E(\mathbf{k})$ as the group velocity $\mathbf{v}$, we get

$$0 = (\mathbf{v_1} - \mathbf{v_3}) \cdot d\mathbf{k_1} + (\mathbf{v_2} - \mathbf{v_3}) \cdot d\mathbf{k_2} \tag{2.10}$$

For the above relation to be satisfied for arbitrary $d\mathbf{k_1}$ and $d\mathbf{k_2}$ implies:

$$\mathbf{v_1} = \mathbf{v_2} = \mathbf{v_3} \tag{2.11}$$

That is, the group velocities, or slopes of the $E - \mathbf{k}$ diagram, must be equal for all final states.

For a parabolic conduction band with effective mass m_e and a valence band with effective mass m_{hh}, the conditions above yield a threshold energy [8]

$$E_{th} = E_g(1 + \frac{m_e}{m_e + m_{hh}}) \qquad \text{for electrons} \tag{2.12}$$

$$E_{th} = E_g(1 + \frac{m_{hh}}{m_e + m_{hh}}) \qquad \text{for holes} \tag{2.13}$$

The hole initiated process is further complicated by the presence of the spin-orbit split-off band. The three band hole impact ionization process is depicted in Fig. 2.6. The spin-orbit split-off hole initiated process dominated over the light hole or heavy hole initiated process because its threshold energy is much lower. Following derivations similar to the electron process, the threshold energy can be shown to be

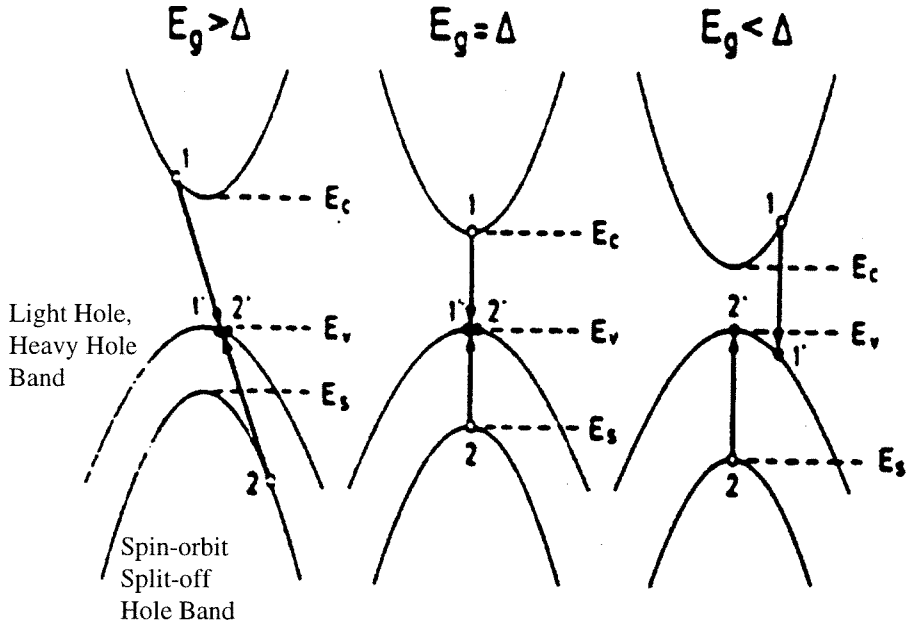

Figure 2.6: Hole initiated impact ionization process involving the spin-orbit split-off band [9].

given by [8]

$$E_{th} = E_g(1 + \frac{m_{so}(1 - \Delta/E_g)}{2m_{hh} + m_e - m_{so}}) \qquad \text{for } \Delta < E_g \tag{2.14}$$

$$E_{th} = \Delta \qquad \text{for } \Delta > E_g \tag{2.15}$$

where Δ is the spin-orbit split-off band offset and m_{so} is the effective mass of the split off band.

These equations make it clear that the spin-orbit splitting can have a pronounced effect on the hole ionization threshold energy by reducing it, while leaving the electron ionization threshold energy unchanged. Since the ionization rate depend exponentially on the threshold energy [2], a strong enhancement of hole/electron ionization ratio is expected in a material where the spin-orbit split-off band difference Δ matches the bandgap energy E_g.

In the $Al_xGa_{1-x}Sb$ system, Δ matches E_g at $x = 0.04 \sim 0.065$, where $E_g \approx 0.75$ eV. This effect was first proposed for avalanche multiplication with limited amount of experimental evidence by Hildebrand et al. [9]. However, other experimental and theoretical studies have since generated contradictory results. In particular, Hidelbrand's findings were supported by Gouskov et al. [10], whereas Kuwatsuka et al. [11] showed that β/α in $Al_{0.06}Ga_{0.94}Sb$ was lower than previously measured and there was no enhancement of β/α at the split-off band resonant condition. Alternative theoretical explanations for the observed effect based on composition disorder has also been proposed [12]. Thus hole ionization enhancement from spin-orbit split-off band resonance in AlGaSb is still an unsolved problem with large technological and scientific consequences.

It should be pointed out that previous studies on the subject have all used liquid phase epitaxy (LPE) as the crystal growth method. Since the effect is possibly material dependent [12], there is clear incentive to study similar device structures fabricated from molecular beam epitaxy.

2.4.2 Electron Impact Ionization Enhancement from Superlattice Band Offset

An alternative way to enhance the impact ionization ratio is to use superlattice structures with large differences in conduction and valence band offset [13]. This effect is illustrated by Fig. 2.7.

Because of the very low doping, the electric field can be regarded as constant across the barrier and well layers in the superlattice. Consider a hot electron accelerating in the large bandgap barrier layer. Upon entering the well it abruptly gains an energy equal to the conduction band edge discontinuity ΔE_c. The effect is that the electron "sees" an ionization energy reduced by ΔE_c. Since the impact ionization rate α increases exponentially with decreasing threshold energy, a large increase in the effective α is expected. When the electron enter the next barrier region, the threshold energy in this material is increased by ΔE_c, decreasing α in the barrier

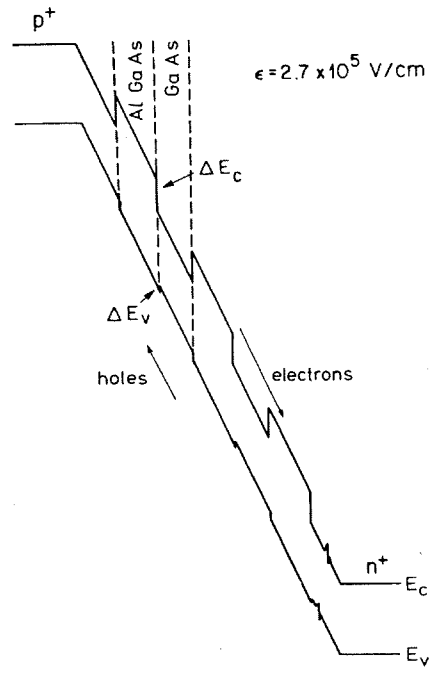

Figure 2.7: Electron impact ionization enhancement in a GaAs/AlGaAs superlattice multiplication layer.

layer. However, since $\alpha_{well} > \alpha_{barrier}$, the exponential dependence on the threshold energy ensure the average α given by

$$\alpha = (\alpha_{well} L_{well} + \alpha_{barrier} L_{barrier})/(L_{well} + L_{barrier}) \tag{2.16}$$

is increased (L denotes layer thicknesses).

In contrast, the hole ionization rate β is not substantially increased because the reduction in hole ionization energy is only the valence band discontinuity ΔE_v, which is made much smaller than ΔE_c. The net result is a large enhancement of α/β.

This approach to ionization ratio enhancement has been successfully demonstrated in AlGaAs [14] and InGaAlAs systems [15]. The scheme has not been adequately exploited in the GaSb/$Al_xGa_{1-x}Sb$ system despite the large band offset differences available. The success of the approach in the AlGaSb system will depend on the transport mechanism in AlSb. If Γ point transport dominates, the effective conduction band offset between AlSb and GaSb will be 1.15 eV, which is much larger than their

valence band offset at 0.45 eV. This would result in a large enhancement of electron to hole ionization ratio in a superlattice structure. However, if electron transports via the X point valley in AlSb, the effective conduction band offset is only 0.55 eV, and the ionization enhancement effect would be diminished.

2.5 Practical Considerations: Dark Current

As mentioned earlier, much of the initial driving force behind the antimonide avalanche photodiode is due to the possibility of ionization ratio enhancement, which results in a better S/N ratio and detector sensitivity. A closer look at the noise contributions and minimum detectivity of the device, however, reveals that the dark current plays just as important a role. In fact, low dark current is the prerequisite for optimal operation of avalanche photodiode.

This can be understood by examining the noise-equivalent-power (NEP) of an avalanche photodiode, which is defined as the incident optical power required to produce a power signal to noise ratio of one in a 1 Hz bandwidth. In essence, the NEP expresses the signal to noise relationship such that the detector sensitivity is better characterized. It's a good indicator of how well the device can be adapted for low signal level applications such as night vision. From the signal to noise relation of an avalanche photodiode, the NEP is derived as

$$NEP = \frac{h\nu}{\eta}[\frac{2}{q}(I_{DB}F_D + \frac{I_{DS}}{M^2} + \frac{2kT}{qRM^2})]^{1/2} \tag{2.17}$$

where $h\nu$ is the photon energy, η is the quantum efficiency, q is the electronic charge, I_{DB} is the bulk dark current, F_D is the excess noise factor associated with I_{DB}, I_{DS} is the surface dark current, M is the multiplication factor, kT is the thermal energy, and R is the detector impedance [2].

The various terms in the expression is plotted as a function of the multiplication factor in Fig. 2.8. It can be seen that the Johnson noise contribution decreases with avalanche gain whereas the contribution from the shot noise term increases with gain.

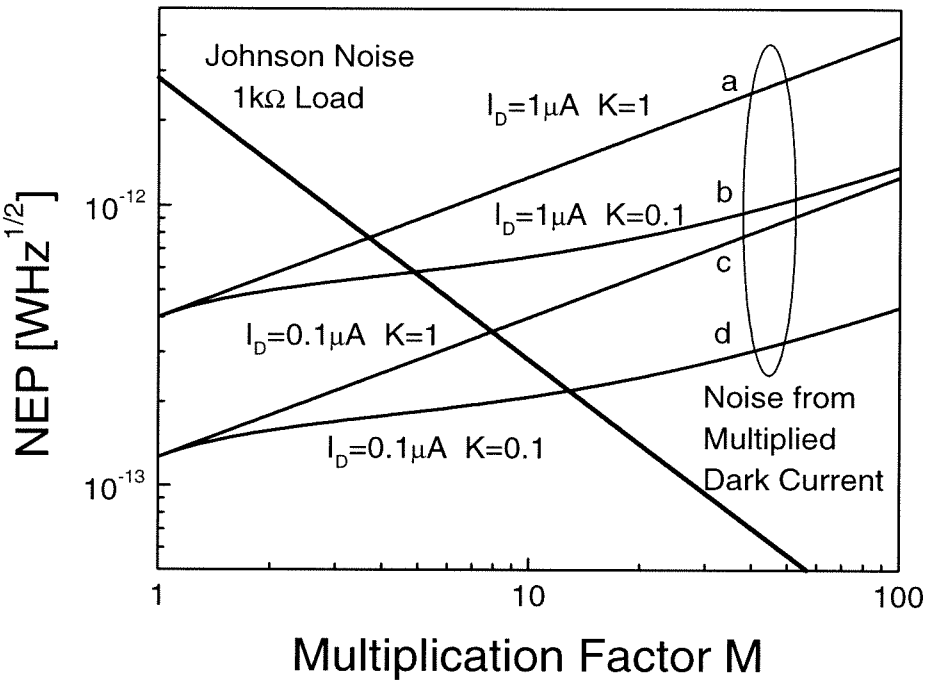

Figure 2.8: Noise equivalent power of an avalanche photodiode.

The detectivity is optimized near the region where these two terms cross each other. Since the Johnson noise comes from the amplifier circuit it is considered part of the system constraint. From the viewpoint of the device designer, a smaller NEP and better sensitivity must be achieved by lowering the shot noise term. This can be done in two ways:

1. Minimize the dark current so that the shot noise contribution starts at a lower level (curves c and d in Fig. 2.8).

2. Improve the ionization ratio so that the excess noise factor increases slower with avalanche gain (curves b and d in Fig. 2.8).

Thus enhancement in ionization ratio alone will only have a secondary effect on the sensitivity of the device. It is crucial that the device dark current is kept as low as possible.

Bibliography

[1] A. Yariv, *Optical Electronics*, Saunders College Publishing, 1991.

[2] G. E. Stillman and C. M. Wolfe, in *Semiconductors and Semimetals, Volume 12*, edited by R. K. Willard and A. C. Beer, Academic, New York, 1977.

[3] R. J. McIntyre, *IEEE Trans. Electron Devices* **13**, 164 (1966).

[4] R. B. Emmons and G. Lucovsky, *Proc. IEEE* **52**, 869 (1964).

[5] P. P. Webb, R. J. McIntyre, and J. Conradi, *RCA Rev.* **35**, 234 (1974).

[6] D. J. Rose, *Phys. Rev.* **105**, 413 (1957).

[7] C. L. Anderson and C. R. Crowell, *Phys. Rev. B* **5**, 2267 (1972).

[8] T. P. Pearsal, R. E. Nahory, and J. R. Chelikowsky, *Symposium on GaAs and Related Compounds: St Louis 1976*, Institute of Physics, London, 1977.

[9] O. Hildebrand, W. Kuebart, K. W. Benz, and M. H. Pilkuhn, *IEEE J. Quantum Electron.* **17**, 284 (1981).

[10] L. Gouskov, B. Orsal, M. Perotin, M. Karin, A. Sabir, P. Coudray, S. Kibeya, and H. Luquet, *Appl. Phys. Lett.* **60**, 3030 (1992).

[11] H. Kuwatsuka, T. Mikawa, S. Miura, N. Yasuoka, Y. Kito, T. Tanahashi, and O. Wada, *Appl. Phys. Lett.* **57**, 249 (1990).

[12] Y. Jiang, M. C. Teich, and W. I. Wang, *J. Appl. Phys.* **67**, 2488 (1990).

[13] G. F. Williams, F. Capasso, and W. T. Tsang, *IEEE Trans. Electron Devices* **3**, 71 (1982).

[14] F. Capasso, W. T. Tsang, A. L. Hutchinson, and G. F. Williams, *Appl. Phys. Lett.* **40**, 38 (1982).

[15] T. Kagawa, Y. Kawamura, H. Asai, M. Naganuma, and O. Mikami, *Appl. Phys. Lett.* **66**, 993 (1989).

Chapter 3 Design, Fabrication, and Characterization of Avalanche Photodiodes

3.1 Introduction to Chapter

The avalanche photodiode work can be viewed as a closed feedback loop consisting of growth, processing, characterization and design. Due to the relative immaturity of the antimonide system, much of the device research is devoted to overcoming materials/fabrication issues and establishing the feedback loop. The experimental procedures and methodologies critical to the realization of antimonide avalanche photodiodes are established in this process and are described in detail in this chapter.

3.2 Device Design

Avalanche photodiodes typically have a PIN configuration with most of the electric field dropped across the intrinsic multiplication region under reverse bias. A p^-n^+ configuration is adapted here because it is difficult to grow AlGaSb layers with low background impurity levels. Due to the low vapor pressure of antimony, Ga tend to occupy Sb vacancies in a AlGaSb crystal and form an anti-site defect which is a double acceptor. Thus unintentionally doped AlGaSb is always p-type [1].

The basic device structure is shown in Fig. 3.1 and consists of three sections: a heavily doped p^+ ($p=2x10^{18}/cm^3$) GaSb contact/absorption layer, an unintentionally doped p^- multiplication layer, and a selectively doped n^+ InAs/AlSb superlattice layer.

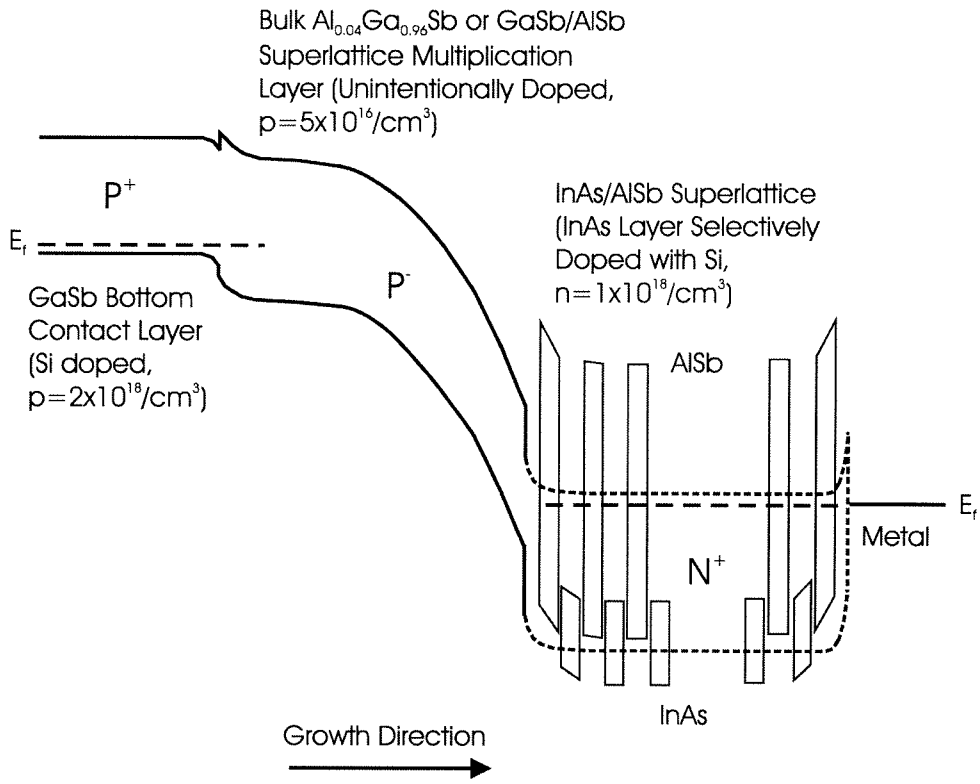

Figure 3.1: Band diagram of the antimonide avalanche photodiode grown by MBE. The device had a p^-n^+ configuration with a p^- bulk $Al_{0.04}Ga_{0.96}Sb$ or GaSb/AlSb superlattice multiplication layer and a selective doped n^+ InAs/AlSb superlattice layer. The device is shown under reverse bias.

3.2.1 Multiplication Layer

The multiplication layer consists of either bulk AlGaSb or GaSb/AlSb superlattices. For bulk AlGaSb multiplication layers, the Al concentration must be adjusted to match the spin-orbit split-off band offset Δ with the bandgap E_g to possibly lower the hole ionization threshold energy [2]. Fig. 3.2 shows the variation of Δ and E_g with Al composition x. It can be seen that the resonant condition occurs approximately for x between 0.04 and 0.065. The composition of 0.04 is chosen by consulting the latest literature [3].

From Hall measurement, the background doping in the AlGaSb layer was found to be $p=5x10^{16}/cm^3$. For an one-sided, abrupt pn junction, the avalanche break down

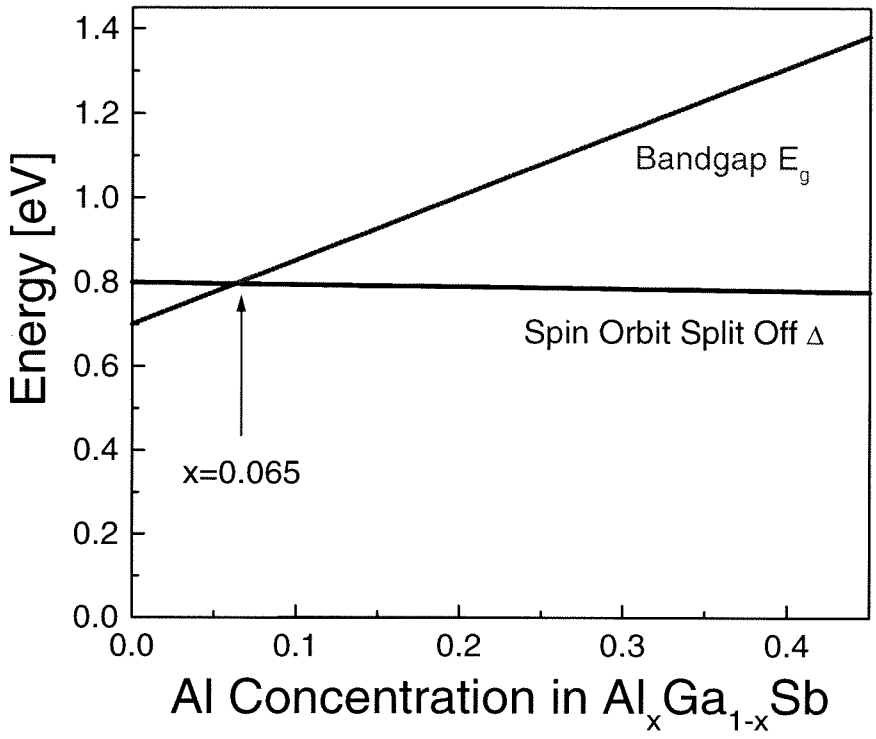

Figure 3.2: Variation of spin-orbit split-off band difference Δ and bandgap E_g with Al composition in $Al_xGa_{1-x}Sb$ [4].

voltage is given by

$$V_B = 60(E_g/1.1)^{3/2}(N_B/10^{16})^{-3/4} \tag{3.1}$$

where E_g is the room temperature bandgap in eV, and N_B is the background doping in cm^{-3} [5]. Given the bandgap of $Al_{0.04}Ga_{0.96}Sb$ at 0.75 eV and the measured doping level, the bulk device is estimated to have an avalanche breakdown voltage of 14 V and a breakdown depletion width of 0.6 μm on the lightly doped side. Thus the $Al_{0.04}Ga_{0.96}Sb$ layer was kept to be at least 0.6 μm thick to maximize the length of the multiplication region. Multiplication layers much thicker than the depletion width will degrade device performance because photo generated carriers in the underlying p-layer will have to traverse a longer path before being swept into the multiplication region.

The superlattice gain layer consists of ten periods of alternating GaSb and AlSb layers. The large conduction band offset (1.15 eV to the Γ point of AlSb, 0.55 eV to the conduction minimum near the X point of AlSb) and comparatively smaller valence band offset (0.45 eV) between these materials indicate potential for electron ionization enhancement. For comparison purposes, the overall thickness of the GaSb/AlSb superlattice gain layer was kept the same as its bulk counterpart at 0.6 μm. This results in a GaSb or AlSb single layer thickness of 300 Å which enables ionizing carriers to gain enough energy at high field conditions (E>10^5/cm) to get out of the well.

3.2.2 InAs/AlSb n-type Superlattice

The InAs/AlSb superlattice n layer is the distinguishing feature of the MBE grown device structure. This approach to n-layer fabrication was first implemented in antimonide mid-infrared lasers [6] and has a number of advantages over conventional ternary or quaternary material. By incorporating Si only in the InAs layer, heavy n-type doping can be achieved without using tellurium, which is highly toxic and a known contaminant to III-V growth. Since the lattice constant of GaSb is between that of InAs and AlSb, the superlattice can be precisely lattice matched to the GaSb substrate by adjusting the InAs and AlSb constituent layer thickness. Variation of the InAs and AlSb layer thicknesses also results in separate tuning of the superlattice conduction and valence band edges, which can be used to optimize the band offset within the device structure. Due to the deeper electron quantum well, the conduction band edge can be tuned over a much wider range, hence the superlattice bandgap is largely dependent on the InAs layer thickness. As illustrated in Fig. 3.3, decreasing the InAs layer thickness from 27 Å to 5 Å results in a 0.4 eV shift in the conduction band edge and an increase of the superlattice bandgap from 0.8 to 1.2 eV [7].

To first order, design constraints for the InAs/AlSb superlattice are due to carrier transport and light absorption considerations. The superlattice is doped at a high level (n=1x10^{18}/cm^3) to form the desired p^-n^+ junction and minimize contact resistance at the surface. When the junction electric field reaches avalanche breakdown

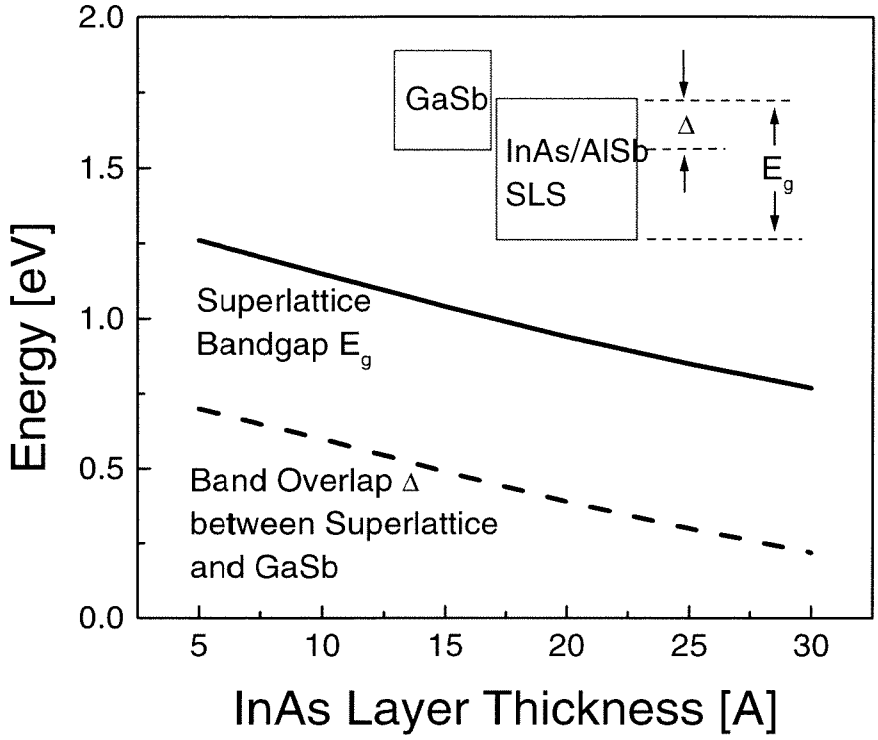

Figure 3.3: Calculated InAs/AlSb superlattice bandgap energy and band overlap with GaSb as a function of the superlattice period thickness [7]. The InAs and AlSb layer thicknesses were assumed to be equal.

levels ($2x10^5$ V/cm), the depletion width on the n-side is on the order of several hundred Å, which is small compared to the overall thickness of the superlattice layer at several thousand Å. Hence bias induced variation in depletion width has only a slight effect on the quantum efficiency of the light absorption process. The superlattice bandgap must also be kept larger than the underlying multiplication layer and the GaSb substrate so that it is transparent to long wavelength photons designed to be absorbed in the p-layer. This will result in electron injection as required in subsequent two wavelength photo characterization experiments (Section 3.5). Given the bandgap of GaSb at 0.72 eV, figure 3.3 indicates that the InAs layer thickness must be kept below 30 Å.

3.3 Growth

3.3.1 Buffer and Multiplication Layers

The avalanche photodiode structures were grown on (100) GaSb wafers, which were etched [8] prior to indium bonding with a solid growth block. Radiatively heated growth blocks were also tried but temperature regulation was a problem due to the small thermal mass of these blocks.

Following oxide desorption under Sb over pressure, a 1 μm thick GaSb buffer layer was deposited at a substrate temperature of 520 °C. The buffer layer was heavily doped with Si and acted as the p^+ bottom contact to the device. The Si cell was subsequently shuttered off during growth of the unintentionally doped multiplication layer. The same substrate temperature was used since the multiplication layer consisted of bulk $Al_{0.04}Ga_{0.96}Sb$. It was raised slightly to 535 °C for growth of GaSb/AlSb superlattice multiplication layers because AlSb required a higher growth temperature [9].

The Sb to Al/Ga flux ratio was typically kept at 3 to 1 as indicated by the residual gas analyzer (RGA). The growth front was smoothed at each hetero interface by a 10 to 30 second Sb soak. A two dimensional growth front was maintained by monitoring the 1×3 reflection high energy electron diffraction (RHEED) pattern characteristic of reconstructed AlGaSb surface.

The composition of the AlGaSb bulk multiplication layer was adjusted by varying the Al and Ga cell temperatures and confirmed by X-ray diffraction studies. As an example, Fig. 3.4 shows a high resolution X-ray scan of a calibration sample. The high quality of the crystal was evidenced by the narrow and symmetric diffraction peaks of the buffer and multiplication layers. Typical full width at half maximum (FWHM) for these peaks were below 30 arc seconds and only slightly larger than that of the GaSb substrate. Such narrow FWHM's allowed easy identification of the closely spaced peaks, and allowed accurate determination of the Al content of these peaks from their positions relative to the substrate peak.

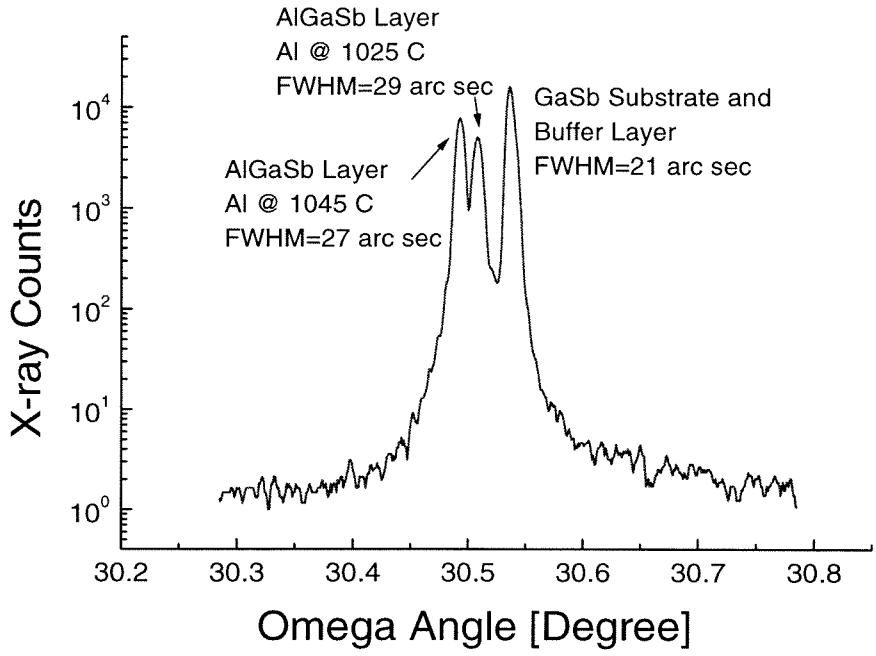

Figure 3.4: X-ray diffraction scan of Al composition calibration sample. The Al composition of the AlGaSb layer was varied by changing the Al cell temperature during MBE growth.

3.3.2 InAs/AlSb Superlattice

The selectively doped InAs/AlSb superlattice was grown following the multiplication layer. N-type doping was easily achieved by opening the Si shutter during growth of the InAs constituent layer. Since this is the last layer in the growth sequence, it is pertinent to maintain a high crystal quality in the layers prior to superlattice growth. Compared to the bulk layers, the superlattice structural quality was much more difficult to maintain due to the short period and mixed anion nature of material.

The difficulties to InAs/AlSb superlattice growth originate from cross incorporation of As and Sb spieces and exchange of these spieces at the InAs/AlSb interface [10]. Arsenic incorporation in the antimonide layers is especially severe because As has a much higher vapor pressure than Sb at a given temperature. During growth of the AlSb layer, there is considerable As background pressure even though the As shutter is closed. For short period superlattices, the situation is worsened because the

shutter times are shorter and there are more individual layers through which crystal imperfections can accumulate.

The X-ray diffraction pattern of an InAs/AlSb superlattice with severe excess As incorporation is shown in Fig. 3.5(a), whereas a well grown crystal is shown in Fig. 3.5(b) for comparison. Note that the superlattice central peak is on the large angle side of the GaSb substrate peak in Fig. 3.5(a) and it is on the small angle side in Fig. 3.5(b). This is the tell-tale sign of arsenic incorporation because the arsenides have smaller lattice constants and larger X-ray diffraction angles. Comparison between the two X-ray scans indicate that less arsenic incorporation results in much better crystal quality as evidenced by the narrower superlattice central peak and existence of higher order satellite peaks in Fig. 3.5(b).

There are two important factors to preventing arsenic incorporation and achieving the result in Fig. 3.5(b): minimize the arsenic flux and lower the substrate temperature as much as possible. The arsenic flux is reduced by using a valved cracker and using the least amount of arsenic flux that still results in an arsenic stabilized InAs growth front (4×2 RHEED pattern). This requires careful calibration since further reduction in arsenic flux results in an indium stabilized growth front (2×4 RHEED pattern) which is detrimental to the crystal quality. Substrate temperature reduction works because the disparity between As and Sb background pressure drops off rapidly with temperature. This strategy is limited by the fact that atoms on the crystal surface lose mobility and three dimensional islanding will result when the growth temperature becomes too low.

Empirically, the arsenic flux was calibrated from trial runs and the ideal growth temperature for the InAs/AlSb superlattice was found to be slightly above the 1×3 to 1×5 transition point of GaSb. The 1×5 RHEED pattern signifies excess amount of antimony on the surface and the transition point is dependent on the antimony flux used. For the antimony flux required in the superlattice growth, the transition typically occured at 420 °C. Hence the substrate was cooled by nearly 100 °C at the start of InAs/AlSb superlattice growth.

The As/Sb exchange reaction at the InAs/AlSb interface was controlled by using

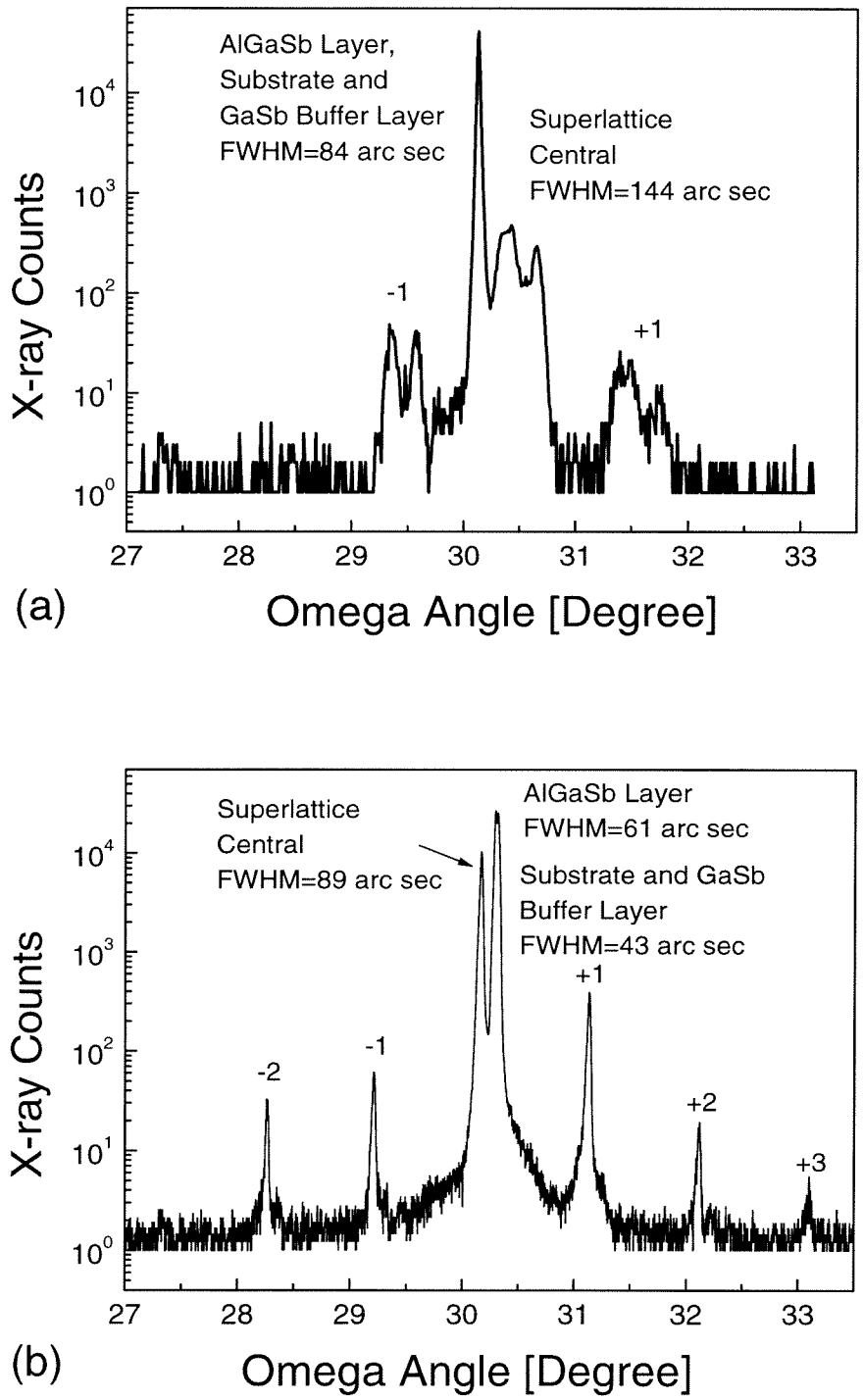

Figure 3.5: X-ray diffraction scan of 27 Å/27 Å InAs/AlSb superlattice (a) grown at a high substrate temperature which resulted in excess As incorporation (b) grown under optimized conditions.

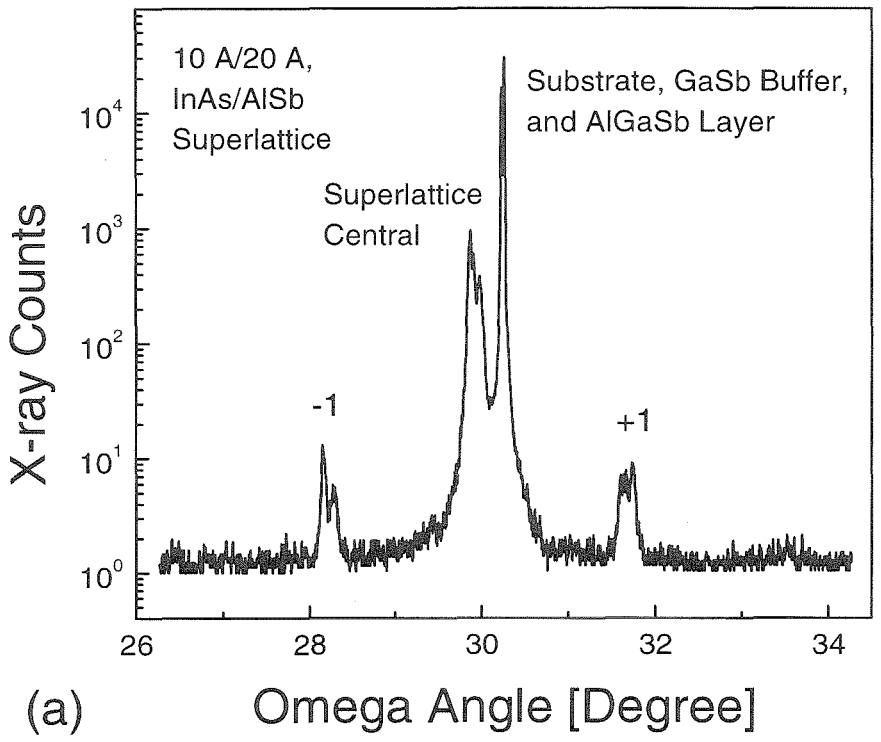

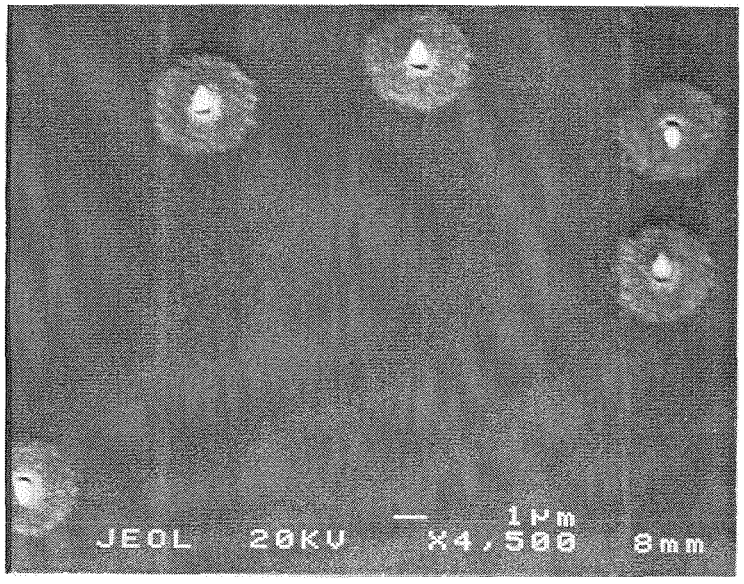

(b)

Figure 3.6: Growth defects may form for short period superlattices despite good X-ray data. (a) X-ray scan of 10 Å/20 Å InAs/AlSb superlattice. (b) SEM scan of the same wafer.

a Sb soak at each hetero interface. X-ray photo electron spectroscopy (XPS) study has indicated that this will result in an InSb like interface [11], which was known to have a lower defect density level [12]. A soaking time of 5 seconds was used because the exchange reaction saturates after a few seconds [11].

With these measures, high crystal quality was consistently achieved. The RHEED pattern remained streaky even for short period superlattices (5 Å, 10 Å) and exhibited sharp 2×4 and 1×3 reconstructions for the InAs and AlSb layers, respectively. X-ray diffraction scans typically yielded second and third order satellite peaks for superlattices with relatively long periods (Fig. 3.5(b)) whereas only the second order peak is visible for short period superlattices (Fig. 3.6(a)). Much of the broadening in the X-ray diffraction peaks are due to drift in substrate temperature and can be further improved with better temperature control. It should be mentioned that good RHEED and X-ray data do not always guarantee defect free wafers. As shown in Fig. 3.6, scanning electron microscopy (SEM) may reveal defect like features even though the corresponding X-ray data looks promising. These defects arise from Ga and In spitting or agglomeration of In, and are highly conductive and detrimental to device performance.

3.4 Processing

3.4.1 Photolithography

To prevent oxidation of the AlSb, all growth runs ended with a 50 Å GaSb capping layer. The wafers were then taken out of the growth chamber and metallized *ex situ* by using a sputter deposition tool. Photolithography was used to define rectangular and circular device mesas that ranged in size from 37 μm to 200 μm. As shown in Fig. 3.7, two types of devices were fabricated with different contact metal configurations. In Fig. 3.7(a), the metal layer was kept at 50 Å so that it was semi-transparent to light. These mesa required only one mask step and was used for preliminary current-voltage and photo response characterization. The device in Fig. 3.7(b) was designed for direct

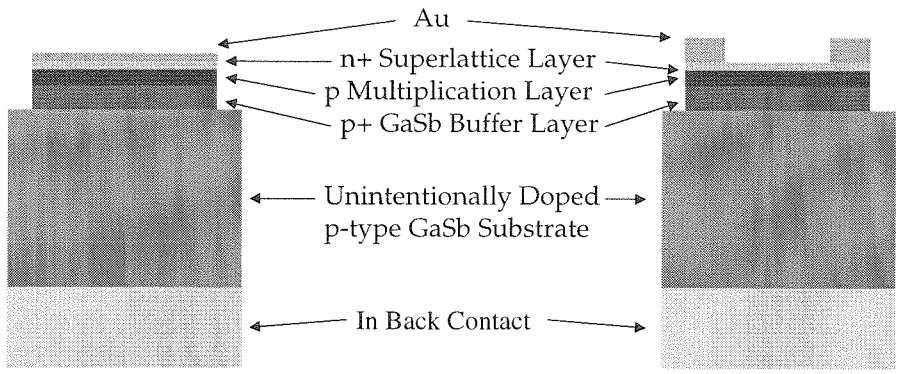

(a) (b)

Figure 3.7: Avalanche photodiode device mesas. (a) Simple mesa with thin metal contact. (b) Mesa designed for direct injection of light through the opening in contact metal.

injection of light into the semiconductor required a two mask process. The mesa had a light sensitive opening surrounded by a ring of contact metal 2000 Å in thickness.

3.4.2 Etching

The etch-down of the device mesas presented a special problem because of the mixed anion nature of the InAs/AlSb superlattice. As shown in Table 3.1, standard wet etch recipes for arsenides and antimonides did not work well. The arsenide etches were stopped by the antimonide layers whereas the antimonide etches did not go through the arsenides. Mixing of these etches was not recommenced due to unforseen chemical reactions that may take place. For example, the sulfuric acid in the arsenic etch may react with the methanol in the antimonide etch and form dimethylene sulfate which is highly toxic [14]. After much experimentation, a satisfactory solution was found by using Cl_2 assisted dry etching. In this process, the sample was immersed in Cl_2 flow while subjected to bombardment by accelerated Ar ions. Etching took place as the high energy ions milled away the material weakened by reactions with Cl_2.

Table 3.1: Summary of etch results.

Etch Type	Result
Br_2:Methanol	Etch very uneven, surface extremely rough
Br_2:HBr:Methanol	Stopped by InAs
Br_2:HNO_3:HCl:Acetic [8]	Stopped by InAs
H_2SO_4:H_2O_2:DI water	Stopped by AlSb
HF:H_2O_2:Tartaric acid [13]	Etches all layers, but results in rough surface
Xe/Cl_2 dry etch	Etches all layers (including metal) with smooth surface

The combination of chemical and physical etching makes the process applicable to arsenides, antimonides, and even metal. The process was also highly anisotropic due to the directional bias of the high energy ions. Typical etch rates were on the order of 1 μm/min for GaSb and 0.1 μm/min for the InAs/AlSb superlattice. As shown in Fig. 3.8, the dry etched sample had a much smoother surface than its wet etched counterpart.

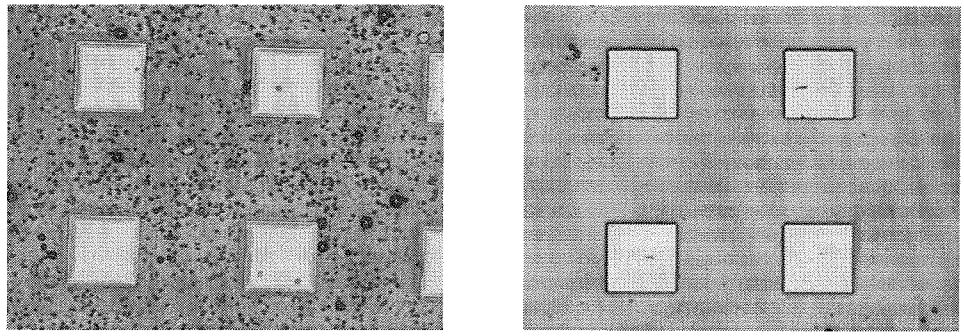

(a) (b)

Figure 3.8: (a) Wet etched surface. (b) Dry etched surface with smoother surface and fewer etch defects.

3.4.3 Passivation

An inherent problem to the dry etching process is the damage on the side walls of the device mesa. This is shown in the cross-sectional SEM scan of the device mesa in Fig. 3.9. The fine striations in the micrograph were created from bombardment of high energy Ar ions and may result in additional surface leakage current.

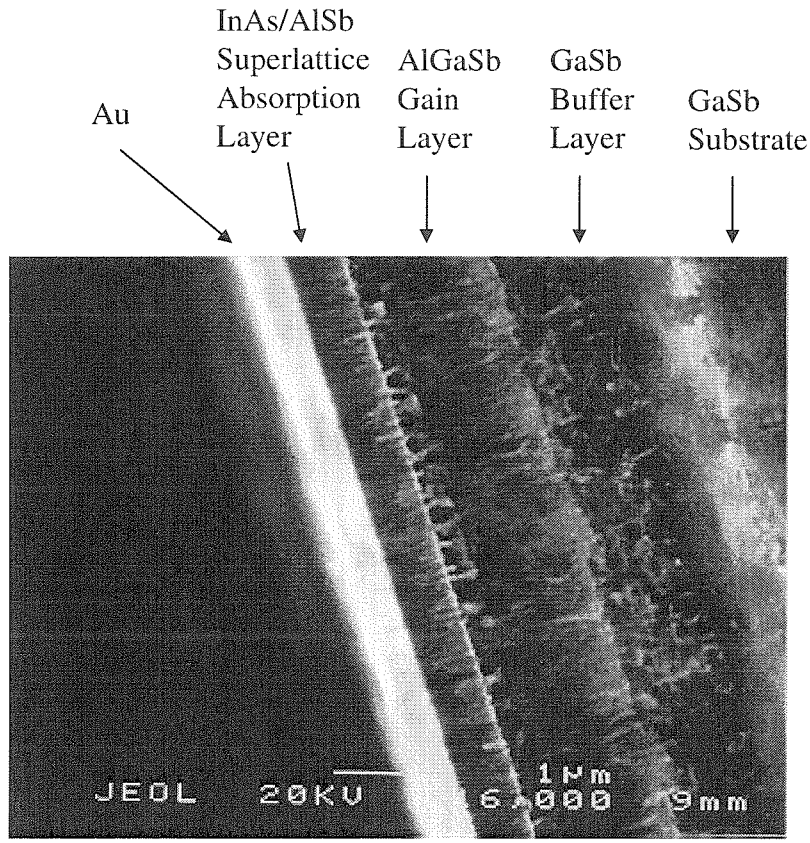

Figure 3.9: Cross-sectional SEM micrograph of the device mesa.

As a remedy, the devices mesas were immersed in HF:H_2O_2:Tartaric acid [13] for 2 minutes following the dry etch. Sulfur passivation was also tried since it was known to passivate III-V surfaces [15]. The procedure involved exposing the device mesas to $(NH_4)_2S$ solutions for up to 5 minutes. The results of these additional processing steps on device dark current are illustrated in Fig. 3.10. It can be seen that the wet etch anneal did not have a noticeable effect on dark current. Sulfur passivation did reduce surface leakage at low reverse bias, but the effect was diminished at high bias.

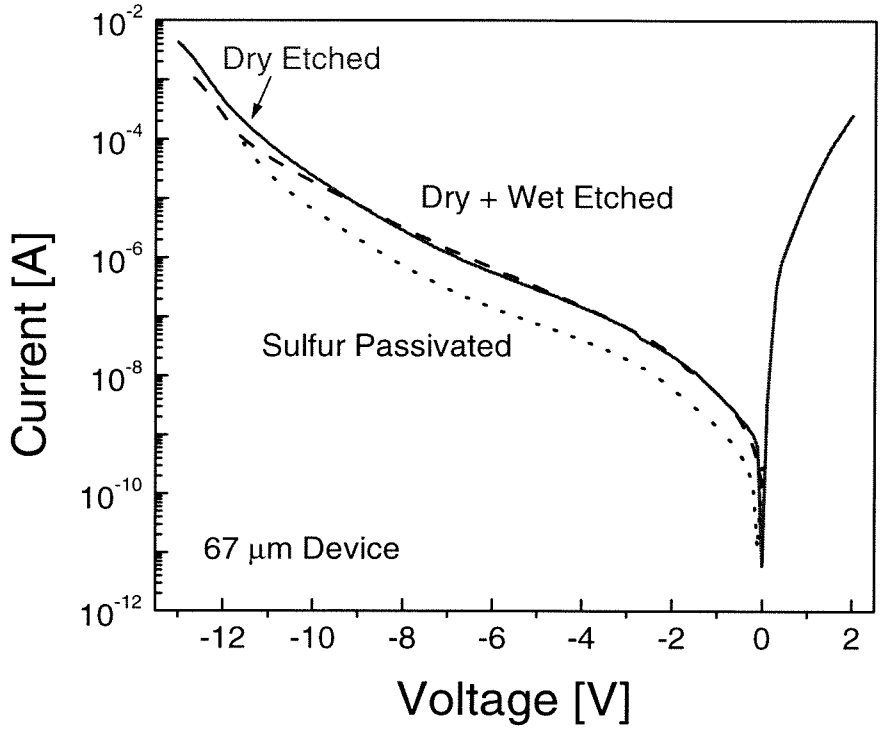

Figure 3.10: Effect of post dry-etching processing steps on device dark current.

These additional processing step did cause deterioration on the chip surface and more variation in individual device I-V characteristics. The effect was especially severe for the $(NH_4)_2S$ soak. Hence the wet etch anneal and sulfur passivation were not included as part of the standard device processing procedure.

3.5 I-V and Photo Response Characterization

The current-voltage (I-V) characteristics of the devices were examined by using a HP 4156 semiconductor parameter analyzer. The I-V curves were taken at room temperature and liquid nitrogen temperatures. The latter required wire bonding onto a device header and dunking the set-up into a liquid nitrogen dewer.

Following I-V characterization, devices with low dark current and good avalanche characteristics were studied for their photo response characteristics. Fig. 3.11 shows a schematic representation of the photo response set-up. In this experiment, the

avalanche photodiodes were excited by using semiconductor lasers. A lock-in scheme at 10 KHz was employed to pick out the multiplied photo signal against the dark current background. The semiconductor laser light was injected via a single mode fiber butt coupled to the top surface of the device mesa. Since the core diameter of the fiber (9 μm) was much less than the mesa diameter ($>$ 37 μm), coupling loss can be prevented as long as the fiber was brought sufficiently close to the device mesa ($<$ 50 μm). This simple light coupling scheme was favored because no re-focusing was needed when a laser of different wavelength was hooked up at the input end of the fiber.

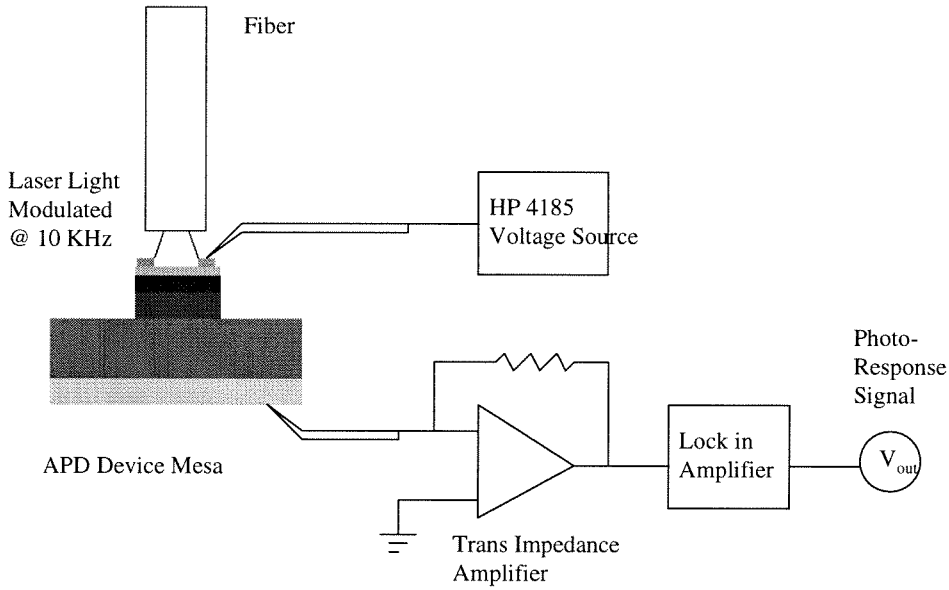

Figure 3.11: Experimental setup for photo response characterization.

In order to measure the electron and hole ionization coefficients of multiplication material, it is necessary to have light absorption in both the p and n regions of the device [16]. This results in electron and hole initiated photo multiplications and different photo gain curves when the electron and hole ionization coefficients are different. The ionization coefficients and their ratio can then be calculated from the coupled pair of photo gain curves if the field profile of the multiplication region is known [16].

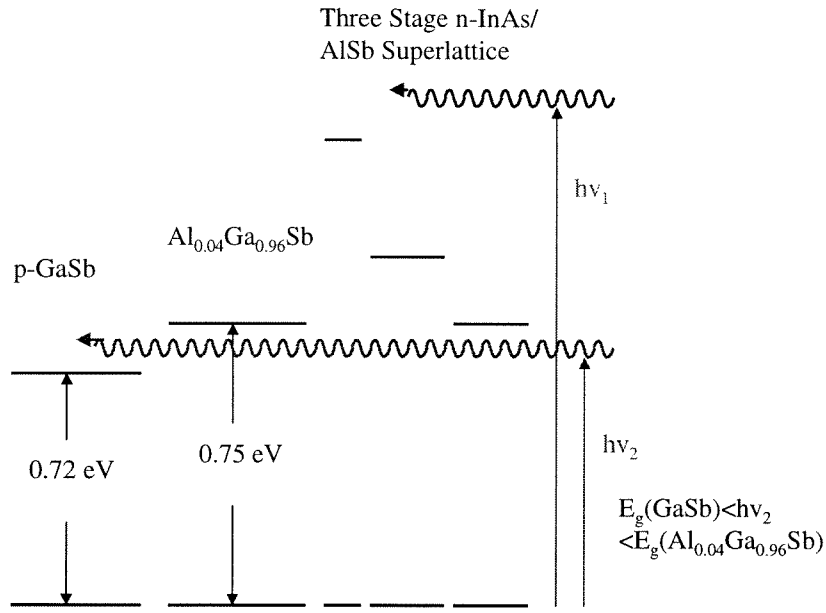

Figure 3.12: Electron and hole carrier injection by using light of different wavelength.

Experimentally, this was accomplished by using semiconductor lasers of different wavelengths. As shown in Fig. 3.12, the 781 nm photons were absorbed in the n-type InAs/AlSb superlattice for hole injection due to its short wavelength, whereas 1645 nm and 1740 nm laser light resulted in electron injection for $Al_{0.04}Ga_{0.96}Sb$ gain layer devices because the energies of the long wavelength photons were below the multiplication layer bandgap and the absorption took place in the underlying p-type GaSb layer.

Bibliography

[1] D. Effer and P. J. Etter, *J. Phys. Chem. Solids* **25**, 451 (1964).

[2] O. Hildebrand, W. Kuebart, K. W. Benz, and M. H. Pilkuhn, *IEEE J. Quantum Electron.* **17**, 284 (1981).

[3] L. Gouskov, B. Orsal, M. Perotin, M. Karin, A. Sabir, P. Coudray, S. Kibeya, and H. Luquet, *Appl. Phys. Lett.* **60**, 3030 (1992).

[4] *Semiconductors: Group IV elements and III-V Compounds*, edited by O. Madelung, Spriner-Verlag, Berlin, 1991.

[5] S. M. Sze, *Physics of Semiconductor Devices*, John Wiley Sons. Inc., New York, 1981.

[6] D. H. Chow, Y. H. Zhang, R. H. Miles, and H. L. Dunlap, *J. Cryst. Growth* **150**, 879 (1989).

[7] J. N. Schulman and R. H. Miles, unpublished.

[8] F. W. O. Da Silva, M. Silga, C. Raisin, and L. Lassabatere, *J. Vac. Sci. Technol. B* **8**, 75 (1990).

[9] D. A. Collins, Thesis, California Institute of Technology, 1993.

[10] D. H. Chow, R. H. Milesand, and A. T. Hunter, *J. Vac. Sci. Technol. B* **10**, 888 (1992).

[11] M. W. Wang, D. A. Collins, R. W. Grant, and T. C. McGill, *J. Vac. Sci. Technol. B* **11**, 1418 (1993).

[12] G. Tuttle, H. Kroemer, and J. H. English, *J. Appl. Phys.* **67**, 3032 (1990).

[13] P. S. Gladkov, Ts. Marinova, V. Krastev, Sh. Dinkov, *J. Electrochem. Soc.* **142**, 2413 (1995).

[14] G. Petzow, *Metallographic Etching*, American Society for Metals, 1976.

[15] M. Perotin, P. Coudray, A. Etcheberry, L. Gouskov, C. Debiemme-Couvy, and H. Luquet, *Mater. Sci. Engineering* **28**, 374 (1994).

[16] G. E. Stillman and C. M. Wolfe, in *Semiconductors and Semimetals, Volume 12*, edited by R. K. Willard and A. C. Beer, Academic, New York, 1977.

Chapter 4 Results of Avalanche Photodiode Study

4.1 Introduction to Chapter

In this chapter the results of antimonide avalanche photodiode research are presented. The material can be roughly divided into two parts. The first part of the chapter describes early effort in dark current reduction and realization of a working device, where the focal point of the research was on the design of the InAs/AlSb superlattice n-type layer. The second part of the chapter describes the photo response characteristics of avalanche photodiodes with bulk and superlattice gain layers and draws comparison between the two approaches.

4.2 Early Results

The very first avalanche photodiode structure examined had a bulk $Al_{0.04}Ga_{0.96}Sb$ multiplication layer and a single stage InAs/AlSb superlattice. The multiplication layer thickness was 1 μm, which ensured that the full depletion width contributed to the avalanche process. The n-type superlattice was 0.5 μm thick and consisted of 100 periods of 27 Å/27 Å, InAs/AlSb layers. The superlattice bandgap was slightly greater than that of GaSb as required in subsequent two wavelength photo response measurements. The relatively long period of the superlattice resulted in good crystal quality as evidenced by the presence of second and third order satellite peaks in the corresponding X-ray diffraction scan (Fig. 3.5 (b)).

The I-V characteristics of this device is shown in Fig. 4.1 and exhibited diode-like behavior. However, the reverse leakage current increased exponentially with bias and reached break down levels (10 mA for a 67 μm device) before avalanche

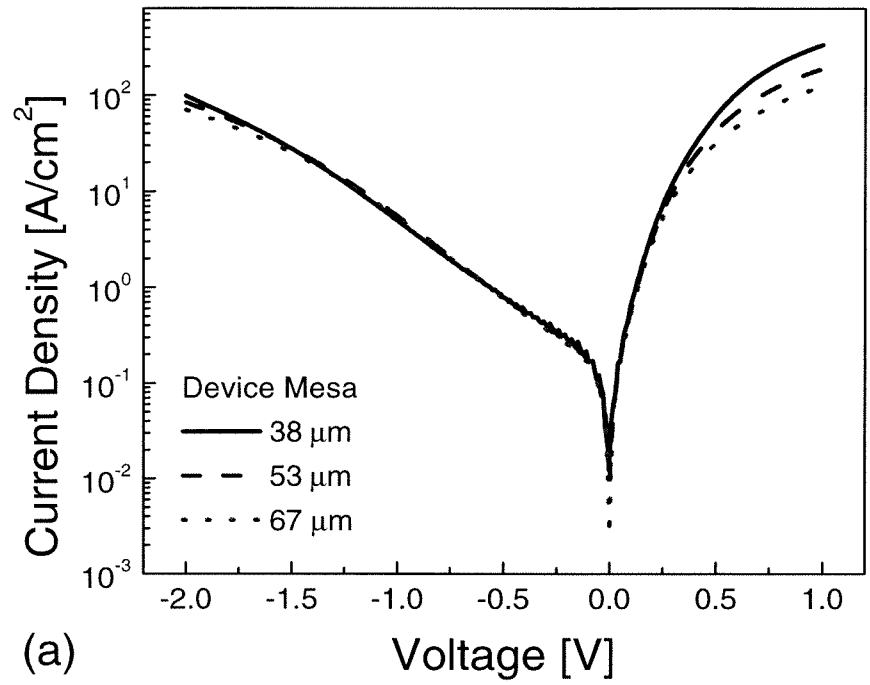

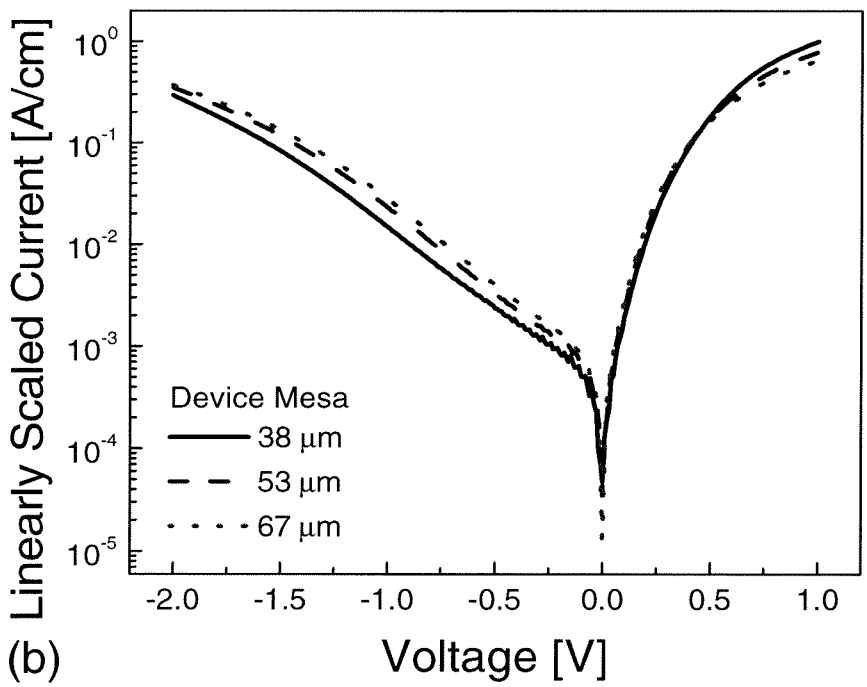

Figure 4.1: Current-voltage characteristics of first avalanche photodiode structures fabricated. (a) Scaling with device area. (b) Scaling with device size.

characteristics could be observed. The high leakage current limited the maximum reverse bias across the device to 2 V, which was an order of magnitude smaller than the expected avalanche break down voltage of 14 V.

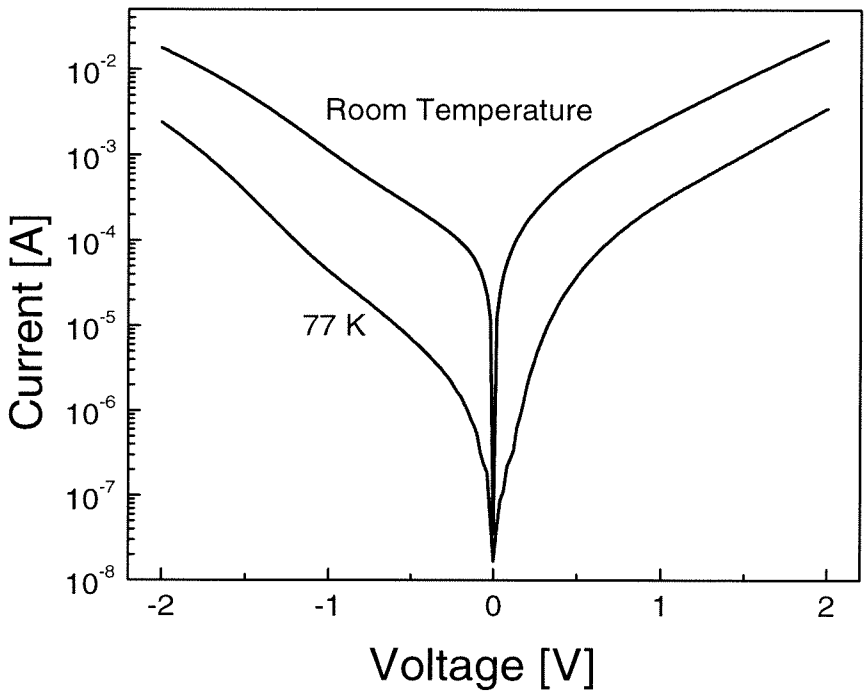

Figure 4.2: Low temperature I-V characteristics of first avalanche photodiodes fabricated.

The origin of the high leakage current was addressed by studying I-V scaling with device size and measuring I-V characteristics at low temperatures. From Fig. 4.1, it can be seen that area scaling dominated the reverse behavior whereas perimeter scaling was more important under forward bias. This indicated that the reverse leakage current had a significant bulk contribution. Given the exponential nature of the reverse current, tunneling across the reverse biased pn junction was suspected as the underlying dark current mechanism. This was confirmed by the low temperature I-V data shown in Fig. 4.2. The reverse current at liquid nitrogen temperature was much smaller than at room temperature but retained the exponential behavior characteristic of tunneling. The break down could not be due to avalanche mechanisms because

the breakdown voltage varied inversely with temperature. At low temperatures, the avalanche breakdown would have happened at a lower voltage due to lack of phonon scattering, i.e. the ionization process is enhanced at low temperatures because the hot carriers are not scattered as much by phonons [1].

4.3 Effect of InAs/AlSb Superlattice Period on Dark Current

The bulk nature of the leakage current indicated that improvements in crystal growth or structural design were necessary. To address the first possibility, the growth conditions were systematically varied to reduce interface defects and improve the general quality of the crystal. Fig. 4.3 shows the I-V curves from two other attempts in comparison with the original result. Curve b was obtained from a wafer grown with a higher Sb/Ga ratio for the avalanche multiplication layer. The higher Sb over pressure should minimize Ga on Sb anti-site defects and reduce the background doping level [2]. Curve C was obtained from a device with the InAs/AlSb superlattice grown at a slightly higher temperature and with a lower Sb/Ga ratio to reduce Sb incorporation. It can be seen that both strategies have produced devices with higher dark currents. In general, deviations from the optimized growth conditions described in Chapter 3 have resulted in worse crystal quality and poorer device characteristics.

These growth experiments indicated that the high dark current was not associated with the crystal quality of the growth and must be due to the inherent property of the structure itself. This hypothesis was confirmed by examining structures with different InAs/AlSb superlattice designs. As shown in Fig. 4.4, changing the constituent layer thicknesses of the superlattice from 27 Å/27 Å to 10 Å/20 Å led to markedly different I-V characteristics. The improvement from the short period superlattice can be understood by examining Fig. 3.3, which shows the calculated variation of the superlattice bandgap and the band overlap between the superlattice and GaSb as a function of superlattice period thickness.

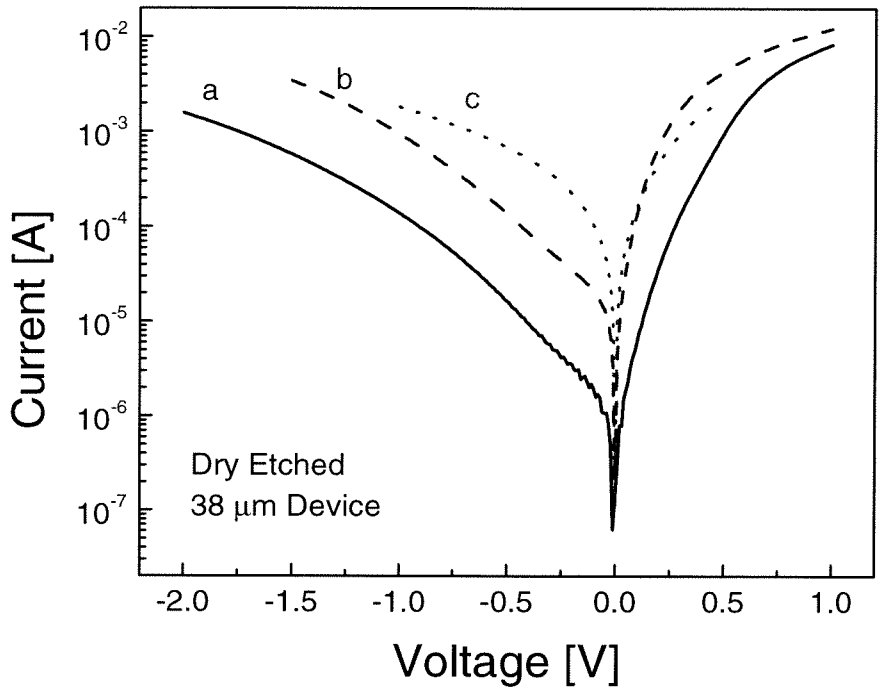

Figure 4.3: Current-voltage characteristics of avalanche photodiodes with $Al_{0.04}Ga_{0.96}Sb$ gain layer and 27 Å/ 27 Å InAs/AlSb superlattice grown under different conditions.

As illustrated in Fig. 4.5, a decrease in the InAs layer thickness leads to narrowing of the electron quantum well and stronger carrier confinement, causing an upward shift in the electron energy level and the conduction band edge. This results in a larger energy gap for the InAs/AlSb superlattice and more band overlap between the n-type superlattice and the multiplication layer. The latter is especially significant since much of the tunneling current originates from the pn heterojunction where the effective bandgap is the smallest in the entire structure. For the 27 Å/27 Å superlattice, the band overlap at the heterojunction is only 0.3 eV, whereas the 10 Å/20 Å structure has a band overlap of 0.58 eV. Using a simplistic model for the tunnel current

$$I \propto exp(-E/kT) \tag{4.1}$$

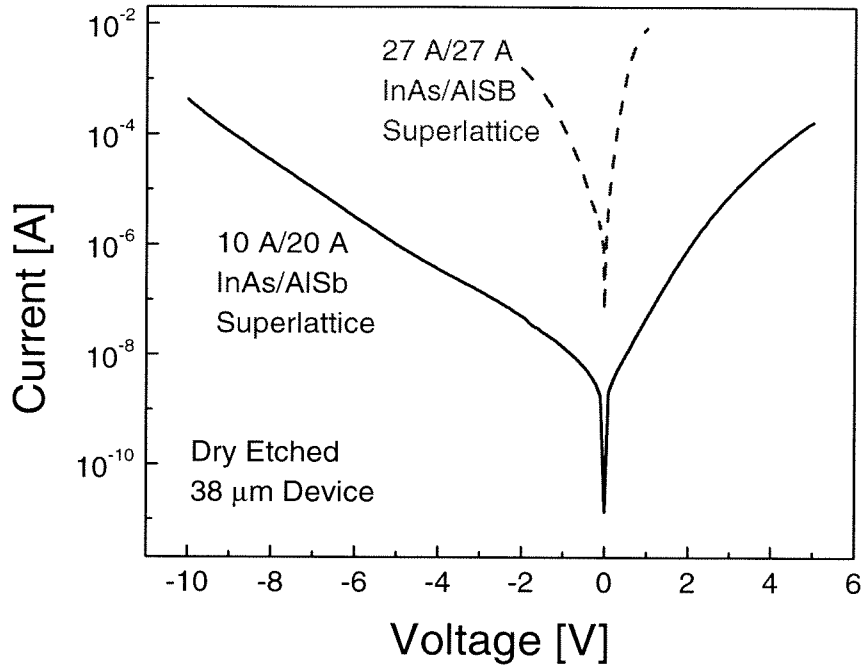

Figure 4.4: Current-voltage characteristics of avalanche photodiodes with $Al_{0.04}Ga_{0.96}Sb$ gain layer and 10 Å/ 20 Å, InAs/AlSb superlattice.

where E is the tunnel barrier (band overlap) and kT is the room temperature thermal energy (25 meV), one concludes that a 0.28 eV change in band overlap should reduce the tunnel current by a factor of 10^4 to 10^5. As shown in Fig. 4.4, this is roughly what was observed.

Note that the InAs layer thickness has a much stronger effect on the conduction band edge and the superlattice bandgap than the AlSb layer thickness. This is due to the much deeper electron quantum wells from the larger conduction band offset between AlSb and InAs (see Fig. 1.1). The shallow hole confinement means that variations in AlSb layer thickness do not significantly alter the valence band edge and the superlattice bandgap.

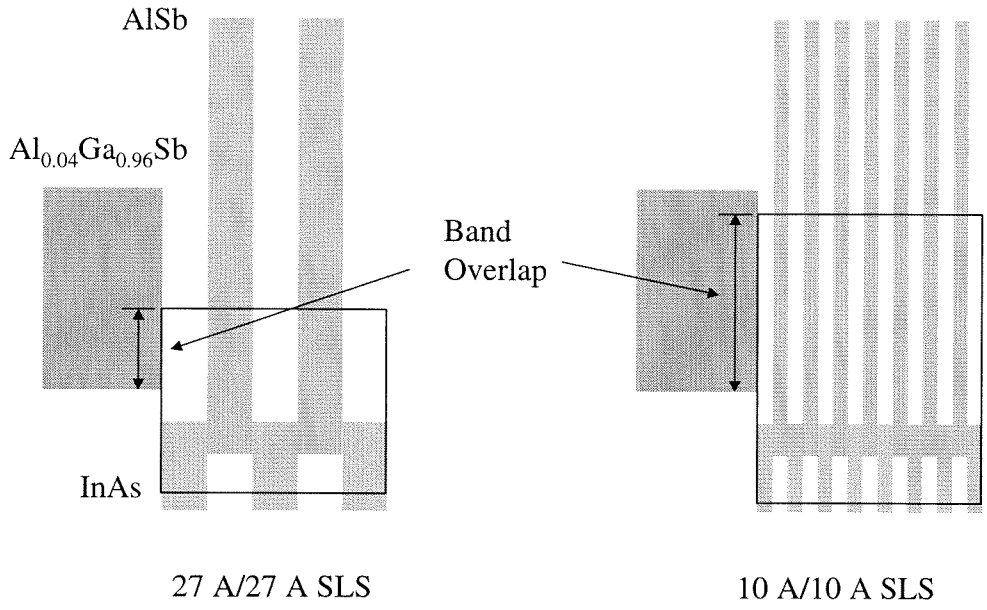

Figure 4.5: Effect of superlattice period on the band alignment between n-type InAs/AlSb superlattice and the $Al_{0.04}Ga_{0.96}Sb$ multiplication layer.

4.4 Optimization of InAs/AlSb Superlattice Design

Despite the reduced dark current, the 10 Å/20Å, InAs/AlSb superlattice retained the exponential reverse I-V behavior characteristic of tunneling. The bulk nature of the dark current was confirmed by scaling studies and the fact that additional processing only has a weak effect on dark current. Moreover, it can be seen from Fig. 4.4 that the forward conduction of the short period superlattice sample was reduced due to the larger superlattice bandgap and Schottky barrier height at the surface.

To further reduce the bulk tunneling current and improve the Schottky contact to the n-type superlattice, an optimized design employing three stages of superlattice was adapted. As shown in Fig. 4.6(a), the multiplication layer was interfaced to a 5 Å/10 Å, InAs/AlSb superlattice to maximize the band overlap at the heterojunction and reduce the tunneling current. Due to the extreme short superlattice period and

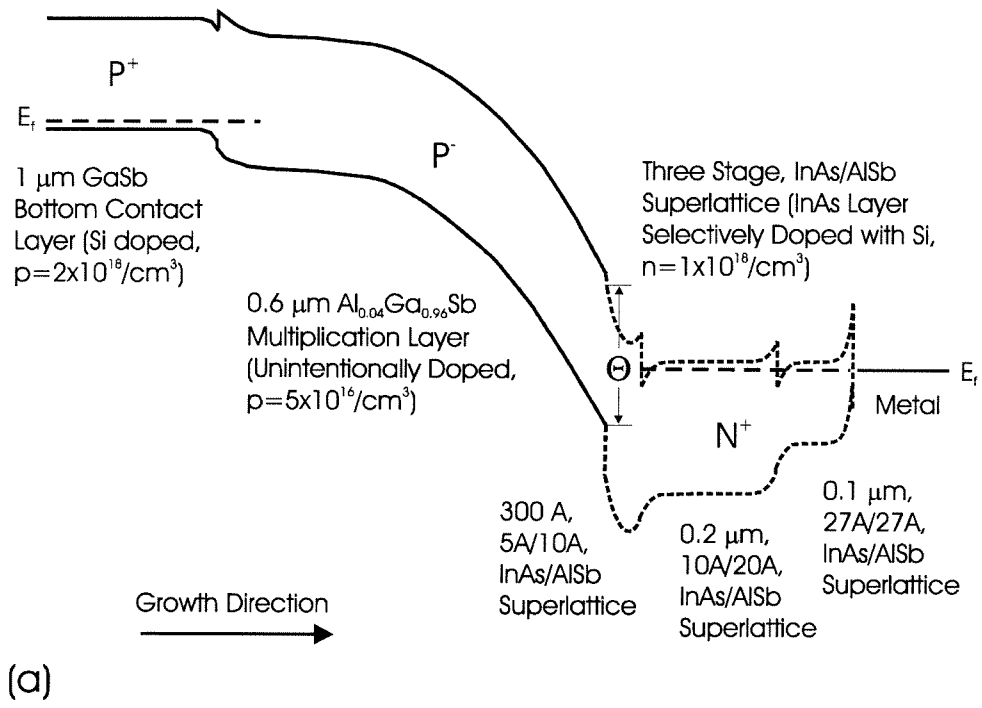

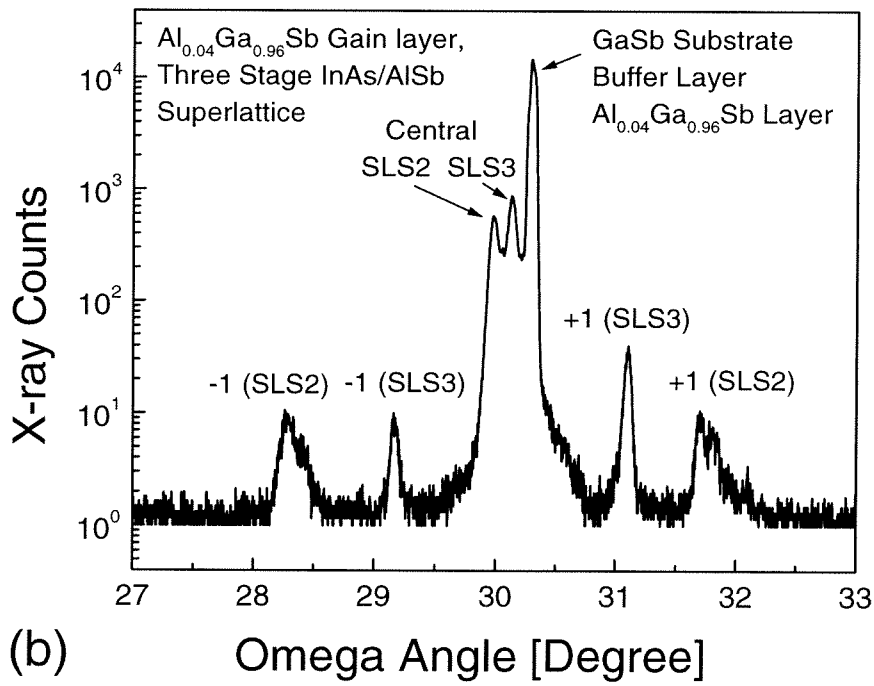

Figure 4.6: (a) Avalanche photodiode structure with $Al_{0.04}Ga_{0.96}Sb$ gain layer and optimized, three stage, n-type InAs/AlSb superlattice. Device is shown under reverse bias. (b) X-ray diffraction scan of the structure.

the large number of interfaces, the overall thickness of the stage was limited to 300 Å so that good crystal quality was maintained for growth of subsequent layers. The second stage consisted of 0.2 μm of 10 Å/20 Å, InAs/AlSb superlattice and served as the transition layer. This was followed by a 0.1 μm thick, 27 Å/27 Å layer with the narrow bandgap necessary for improving contact characteristics at the surface. The X-ray scan of one such structure is shown in Fig. 4.6(b). The high crystal quality of growth was evidenced by the presence of satellite diffraction peaks of the second and third InAs/AlSb superlattice stages.

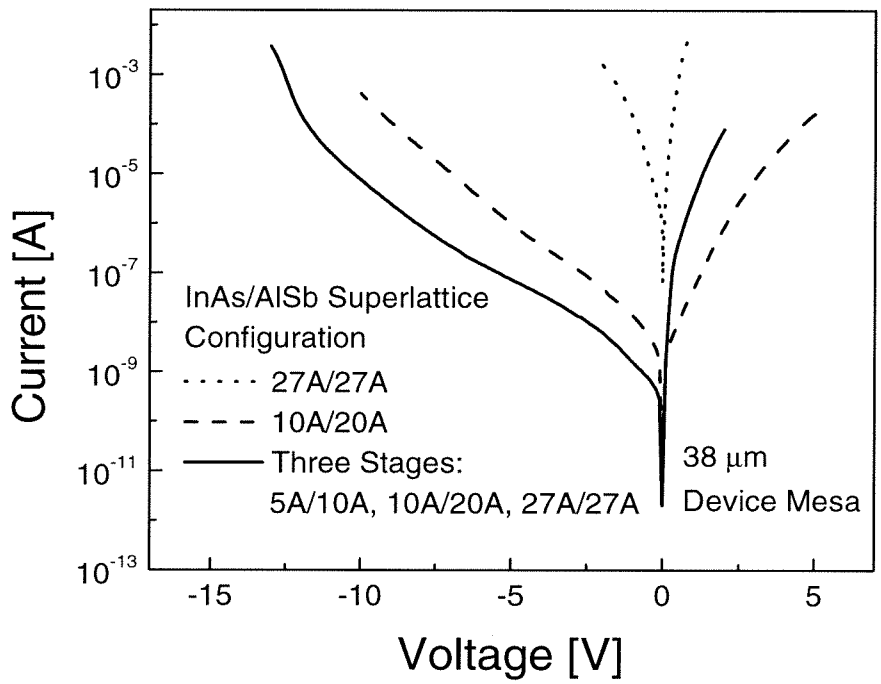

Figure 4.7: Current-voltage characteristics of avalanche photodiodes with $Al_{0.04}Ga_{0.96}Sb$ gain layer and optimized n-type InAs/AlSb superlattice.

The I-V characteristic of the structure is shown in Fig. 4.7, where previous results are also plotted for comparison. It can be seen that the device was more conductive under forward bias due to the smaller bandgap of the 27 Å/ 27 Å superlattice contact layer. The short period superlattice at the interface resulted in a 0.7 eV band overlap with the multiplication region. And the dark current was reduced by another two order of magnitude over the previous iteration due to the 0.12 eV increase in band

overlap. At a reverse bias greater than 10 V, rapid current increase characteristic of avalanching action could be observed. A breakdown voltage of 13 V was consistently obtained and very close to the predicted avalanche break down value of 14 V.

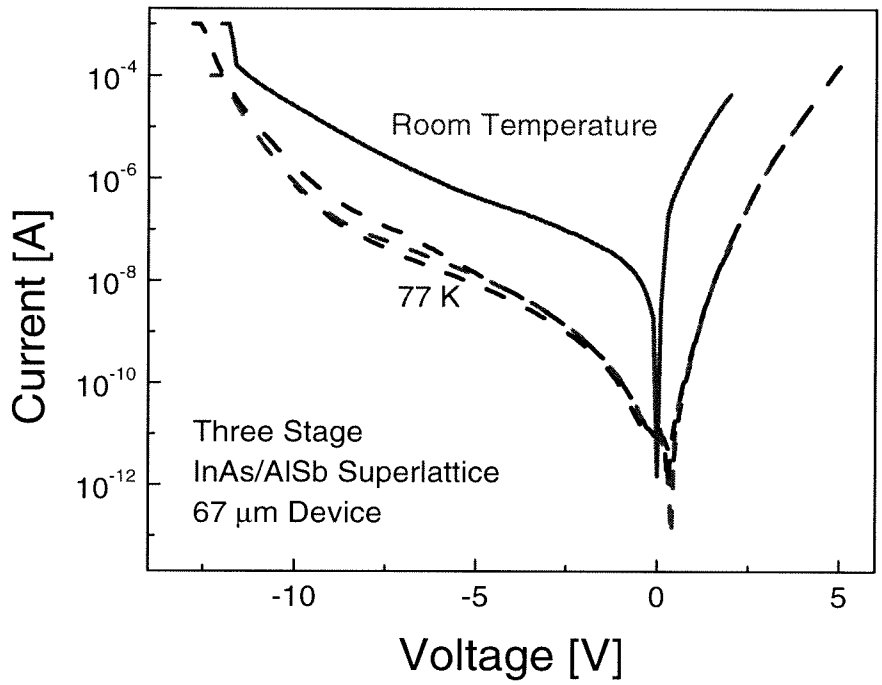

Figure 4.8: Low temperature reverse break down characteristics of avalanche photodiode with $Al_{0.04}Ga_{0.96}Sb$ gain layer and optimized n-type InAs/AlSb superlattice.

To verify the avalanche nature of the break down, I-V data were taken at liquid nitrogen temperatures. As shown in Fig. 4.8, the avalanche onset voltage, i.e. the voltage at which the slope of the I-V curve began to steepen, occurred at a lower bias due to reduced phonon scattering at low temperatures.

4.5 Results from Bulk $Al_{0.04}Ga_{0.96}Sb$ Devices

By adapting the optimized, three stage design for the InAs/AlSb superlattice, the dark current in bulk $Al_{0.04}Ga_{0.96}Sb$ devices was reduced to a low enough level for direct study of avalanche characteristics. The photo gain, associated dark current,

and ionization characteristics of the working device were henceforth measured by using the optical fiber setup described in Section 3.5.

4.5.1 Photo Response Unity Gain Correction

Figure 4.9 shows the unprocessed photo gain data. The 1740 nm photo gain curve was nearly identical to the 1645 nm curve and is not shown here to reduce clutter. The quantum efficiencies for 781 nm, 1645 nm and 1740 nm light were 16%, 10%, and 5% respectively. It can be seen that the quantum efficiency rose slowly as the bias was increased. The effect was most pronounced for 781 nm light and resulted in an inflexion point in the photo gain curve at about 2 V. The drift in quantum efficiency with bias must be carefully corrected if the true avalanche gain is to be measured.

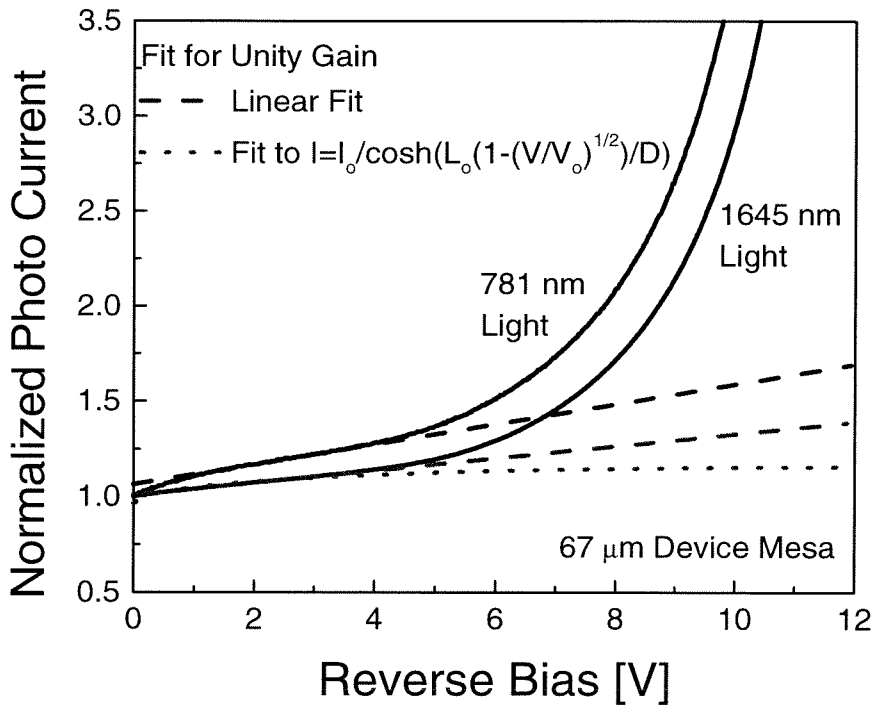

Figure 4.9: Photo response of the $Al_{0.04}Ga_{0.96}Sb$ gain layer device without correction. The curves are fitted at low bias to correct for changes in quantum efficiency with device bias.

Since the 781 nm light was absorbed in the heavily doped n-type InAs/AlSb

superlattice, the increase of quantum efficiency with bias could not be attributed to the bias dependence of the depletion width. The junction depletion width on the n side was no more than several hundred Å even at break down voltages. Given an overall thickness of 0.3 μm for the n-type layer and an absorption length on the order of 0.1 μm, most of the 781 nm light was absorbed near the surface and the slight variation in junction depletion width should have negligible effect on collection efficiency. Instead we attribute this effect to band discontinuity in the InAs/AlSb superlattice. As shown in Fig. 4.6(a), band bending from heavy doping and the multi-stage design of the n-type superlattice resulted in hole barriers in the valance band even though most of the band offset occurred in the conduction band. Such barrier induced light injection inefficiency was even more severe in devices with GaSb/AlSb superlattice multiplication layers as will be discussed in Section 4.6.2. To correct for this effect, the photo gain curve around the inflexion point was fitted to a straight line, which was extended to higher bias regions and taken as the unity gain background.

For 1645 nm and 1740 nm light, the drift in quantum efficiency entailed a different mechanism. Since the long wavelength photons were absorbed in the underlying p-type GaSb buffer layer, the photo-generated electrons must diffuse across the undepleted region of the multiplication layer to be collected. The quantum efficiency varied with bias because the depletion width (and hence the length of the undepleted section) in the lightly doped multiplication region was a strong function of voltage. According to Woods et al. [3],the collected current should vary with voltage according to

$$I = \frac{qG_0}{cosh(L_0 - W)/L_{ph})} \tag{4.2}$$

where L_{ph} is the diffusion length for holes in $Al_{0.04}Ga_{0.96}Sb$, G_0 is the clearing rate of holes at the hetero interface, L_0 is the width of the $Al_{0.04}Ga_{0.96}Sb$ multiplication layer and W is the depletion layer width. The fitted unity gain curve is illustrated in Fig. 4.9 and can be seen to differ only slightly from the straight line fit. For simplicity

and consistency, the straight line fit was again adapted here.

4.5.2 Photo Gain and Dark Current Characteristics

The corrected near-infrared photo gain curve for the device is shown in Fig. 4.10 along with the device dark current characteristics. Maximum gains as high as 30 were observed. The dark current density was typically 6 A/cm^2 at a more moderate gain of 10.

At low bias, the dark current can be seen to increase exponentially with voltage, indicating that tunneling mechanism was at work. At high bias, the dark current rose faster and deviated from the exponential curve. However, the exponential behavior was recovered when the unmultiplied dark current (dark current divided by the photo gain, dashed line in Fig. 4.10(a)) was plotted. This indicates that the reverse leakage at high bias underwent multiplication and must be due to bulk tunneling rather than surface leakage. As shown in Fig. 4.10(b), the additional exponential contribution from tunneling caused the dark current to rise at a faster rate than the photo gain. These observations were supported by scaling I-V scaling studies where the dark current was found to scale with the device area (Fig. 4.14(a)). Thus we conclude that the relative high levels of dark current were due to tunneling from the small bandgap of the $Al_{0.04}Ga_{0.96}Sb$ multiplication layer and were inherent to the bulk device.

4.5.3 Impact Ionization Rates

The ionization rates of the electrons and holes in the bulk gain layer device were measured by using the two wavelength photo injection scheme described in Section 3.5. Figure 4.11(a) shows the experimental photo gains curves for 781 nm and 1645 nm light. The data have been corrected for bias-induced variation in unity gain. If we assume that pure holes were injected from 781 nm light illumination and pure electrons were injected from 1645 nm light illumination, the electron and hole impact ionization rates can be derived from these curves by using the formulas:

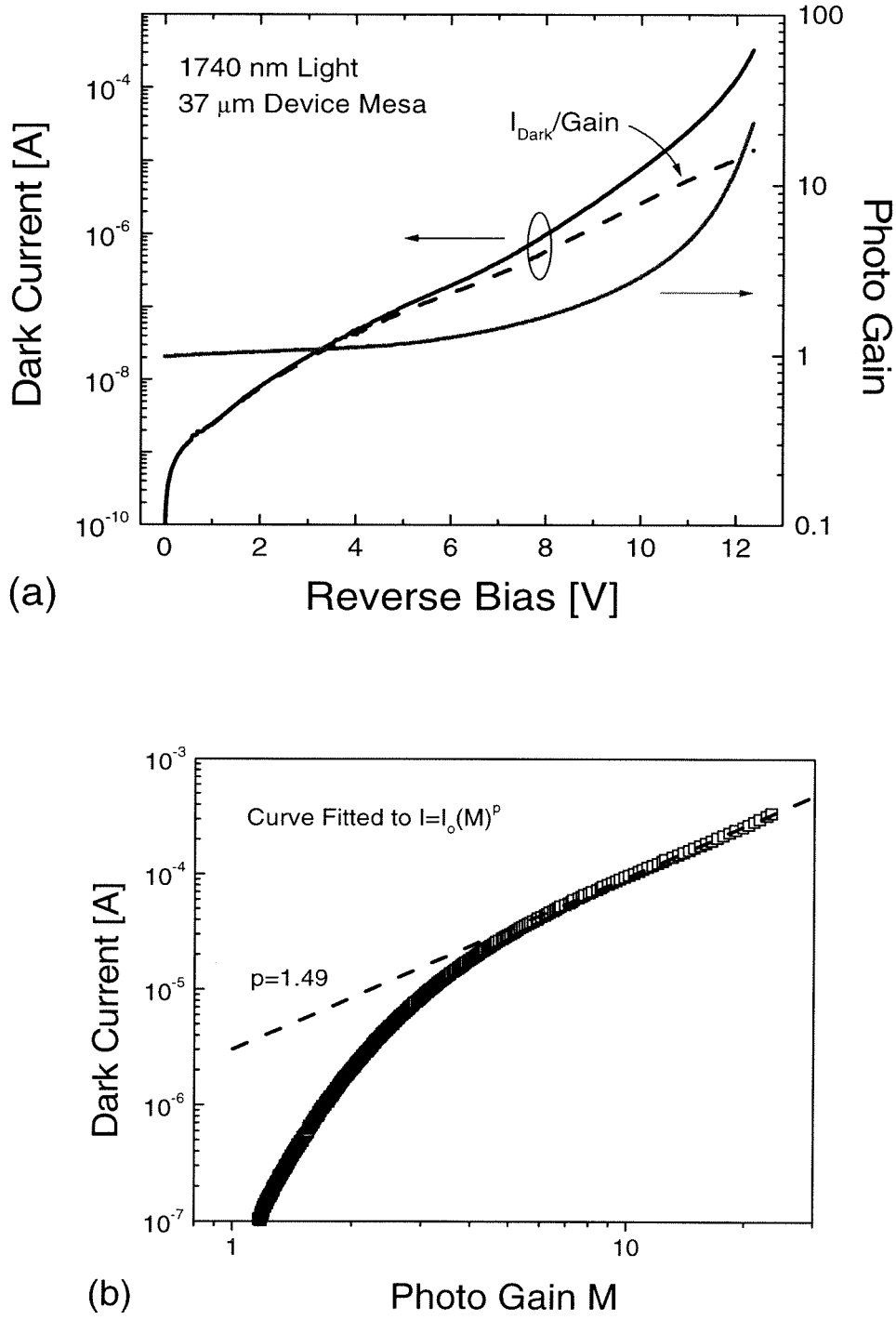

Figure 4.10: (a) Dark current and near infrared photo gain characteristics of avalanche photodiodes with $Al_{0.04}Ga_{0.96}Sb$ as the multiplication layer. The dashed line shows the un-multiplied dark current. (b) Device dark current plotted as a function of the photo gain. The data was fitted to a power law $I=I_o(M)^p$, where p=1 for constant un-multiplied dark current.

$$\alpha(E) = E\frac{1}{M_n(V)M_p(V)}\frac{dM_n(V)}{dV} \tag{4.3}$$

$$\beta(E) = E(\frac{1}{M_p(V)}\frac{dM_p(V)}{dV} - \frac{1}{M_n(V)}\frac{dM_n(V)}{dV}) + \alpha(E) \tag{4.4}$$

where $\alpha(E)$ and $\beta(E)$ are the electron and hole impact ionization rates, $M_n(V)$ and $M_p(V)$ the photo gain at bias V for electron and hole injection, and E the maximum electric field in the abrupt pn junction at bias V [4]. These equations were derived by assuming the field profile of a one sided, abrupt, p^-n^+ junction without punch through, which implies that the depletion width is always smaller than the p^- layer thickness and does not extend into the p^+ contact layer at high reverse bias.

The calculated ionization rates are shown in Fig. 4.11(b) and can be seen to follow the general $\alpha, \beta = exp(-a/bE)$ behavior. This is the expected field dependence for impact ionization rates at high field conditions [5]. However, the opening between the electron and hole ionizations curves was smaller than expected and the measured hole ionization rates were only slightly higher than those of electrons.

There are two explanations for this result. The first possibility is that the long wavelength photons were partially absorbed by the $Al_{0.04}Ga_{0.96}Sb$ multiplication layer or the InAs layers in the n-type superlattice and pure electron injection was not achieved. As shown in Fig. 4.12, under high field conditions, a semiconductor can absorb photons that fall within its bandgap due to the Franz-Keldysh effect [6]. Since the 1645 nm (0.74 eV) and 1740 nm (0.72 eV) photons have energies just below the bandgap of the $Al_{0.04}Ga_{0.96}Sb$ multiplication layer (0.75 eV), partial absorption in the multiplication layer was likely to be important. A second possibility is that quantum efficiency increased more rapidly with bias than was accounted for by the linear correction for unity gain. This was evidenced by the fact that the two corrected photo gain curves in Fig. 4.11(a) lied on top of each other before reaching a nominal

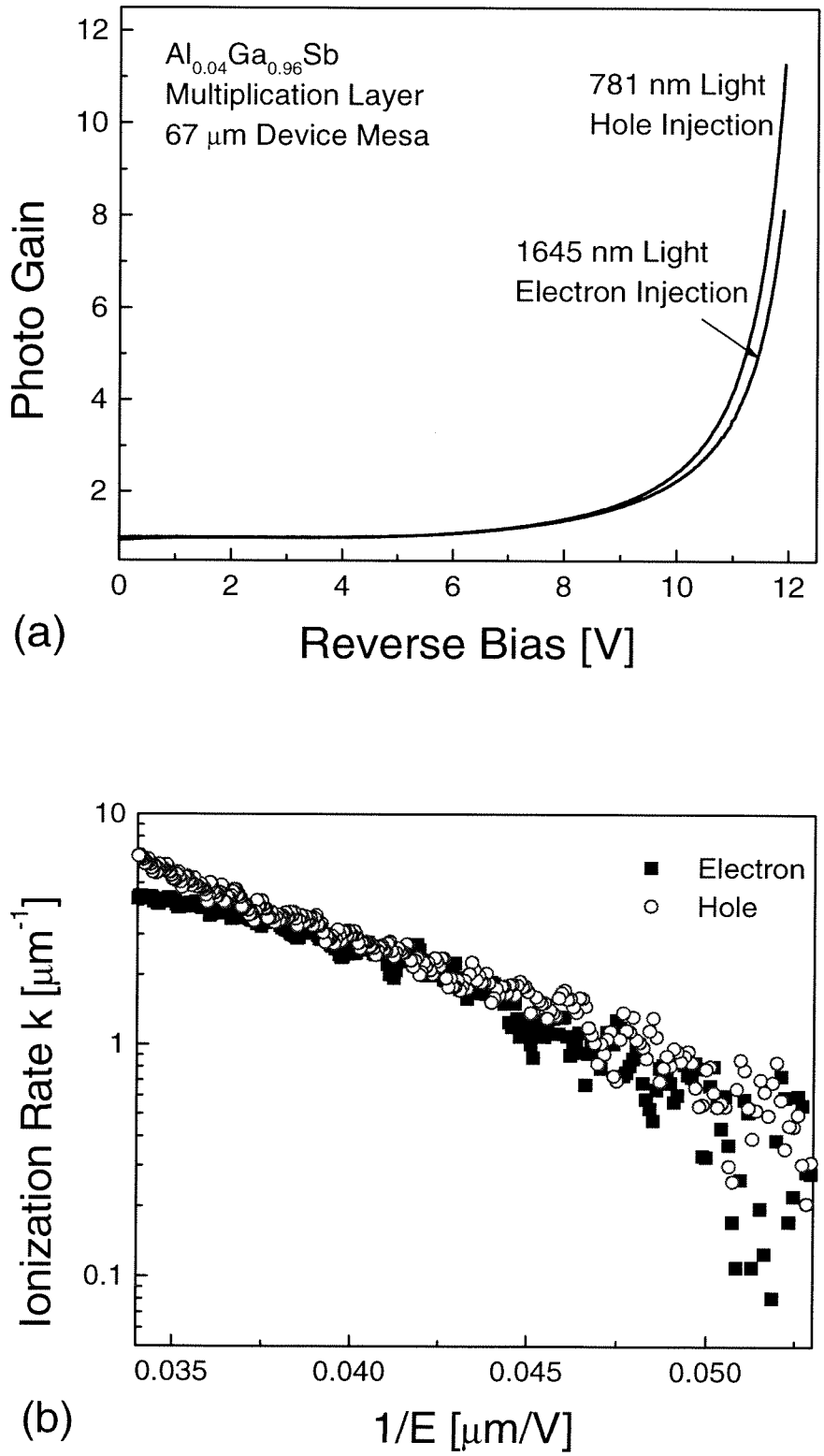

Figure 4.11: (a) Photo gain curves for hole and electron injection using 781 nm and 1645 nm light. (b) Calculated hole and electron impact ionization rates in $Al_{0.04}Ga_{0.96}Sb$. The device was assumed to have an abrupt pn junction.

gain of 2. The observed gain before this point may be due to an increase in quantum efficiency.

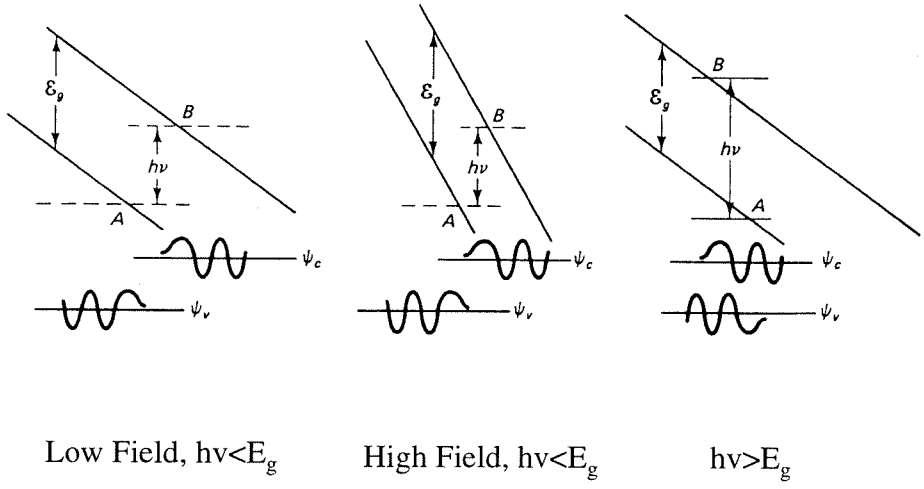

Figure 4.12: Franz-Keldysh absorption of photons by semiconductors. Absorption in the bandgap is possible due to overlapping of wave functions under high field conditions [6].

Despite these short comings, the photo gain curves in Fig. 4.11(a) were consistent with hole ionization enhancement since hole injection always yielded higher photo gains. This result was obtained from a large number of devices under different experimental conditions and can be regarded as partial confirmation of hole ionization enhancement in $Al_{0.04}Ga_{0.96}Sb$.

4.6 Results from Superlattice Devices

Following study of avalanche photodiodes with bulk $Al_{0.04}Ga_{0.96}Sb$ gain layer, devices with superlattice gain regions were fabricated and characterized by using the same methodology. The superlattice multiplication region consisted of 10 periods of alternate GaSb and AlSb layers 300 Å in thickness. The overall thickness of 0.6 μm for the gain layer was the same as the bulk device and enabled direct comparisons between the two types of devices. The optimized, three stage InAs/AlSb superlattice n-type

layer which resulted in low dark current and improved contact resistance for the bulk device was also adapted in the superlattice device.

4.6.1 Photo Gain and Dark Current Characteristics

The near infrared photo gain and dark current characteristics of the superlattice gain layer device are shown in Fig. 4.13. The device yielded an avalanche break down voltage of 18.5 V, which was higher than its bulk counterpart due to the presence of additional AlSb barriers in the gain region. Since long wavelength photons were absorbed by GaSb layers in the superlattice gain region, the two wavelength scheme for measuring impact ionization rates could not be applied. Illuminations by the 781 nm, 1645 nm, and 1740 nm lasers all resulted in hole injection and there was little difference between the photo gain curves except for the quantum efficiency achieved (20%, 5% and 3% at unity gain, respectively). Comparing Fig. 4.13(a) to Fig. 4.10(a) reveals that the avalanche characteristics were much more pronounced for the superlattice device. As shown in Fig. 4.13, gain factors up to 300 were observed in the near infrared for the superlattice device. At a gain factor of 10, the dark current for the 37 μm device was 8 μA, which was an order of magnitude lower than in bulk $Al_{0.04}Ga_{0.96}Sb$ devices and comparable to InGaAs/InAlAs superlattice avalanche photodiodes of similar design [7].

Further examination of the superlattice gain layer characteristics reveals more subtle differences. In contrast to the bulk device, Figure 4.13(b) shows that the superlattice dark current increased slower than the photo gain in the avalanche region. In fact, the un-multiplied dark current stayed constant or decreased with voltage at high bias (dashed line in Fig. 4.13(a)). This indicated that much of the dark current did not undergo multiplication and must be from surface leakage. This suggested that bulk tunneling current had been suppressed due to the presence of AlSb barriers in the superlattice gain region.

The comparative merits of the superlattice and bulk gain layer devices are best illustrated in Fig. 4.14, which plots on a log-log scale the leakage currents for both

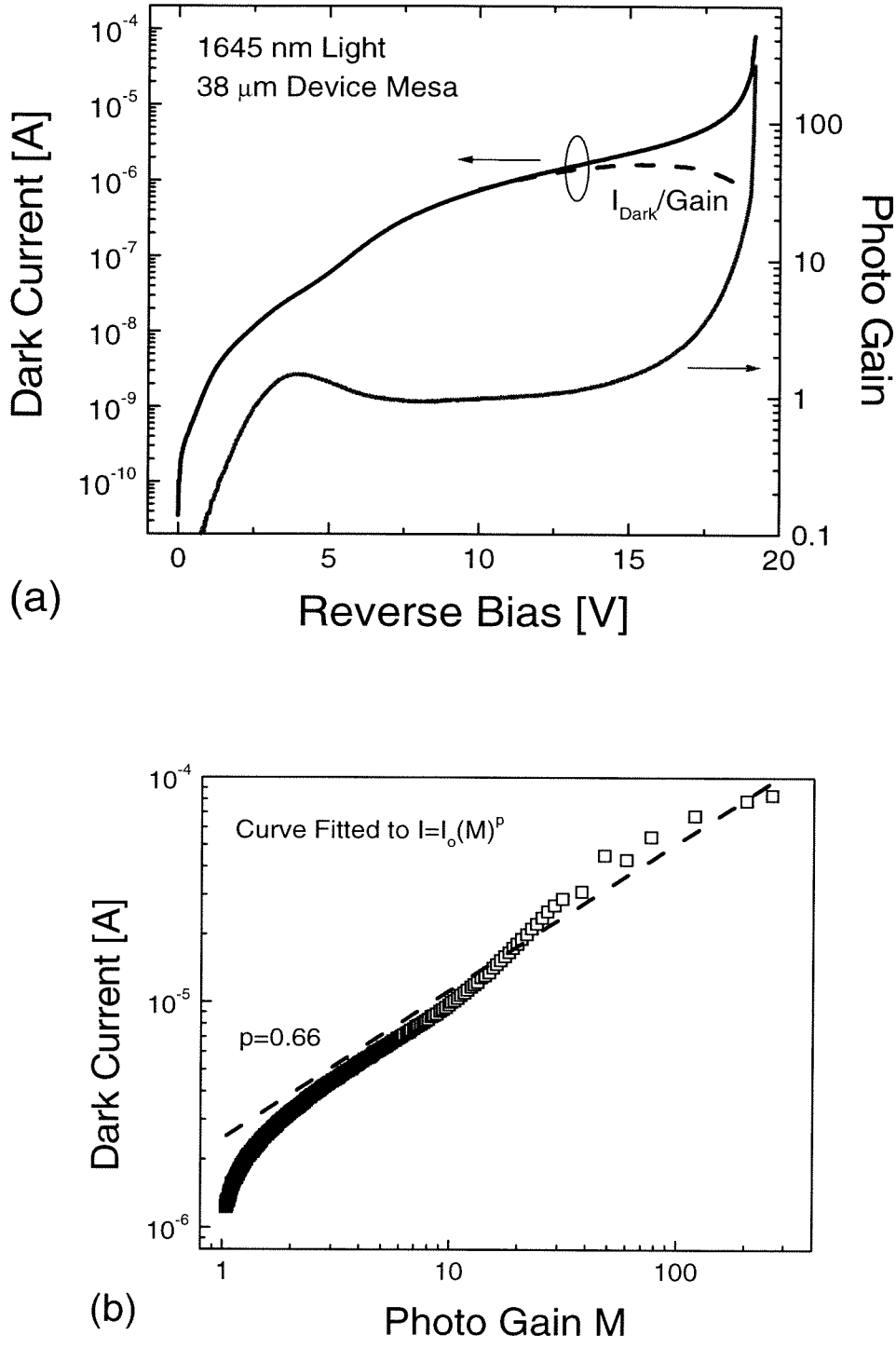

Figure 4.13: (a) Dark current and photo gain characteristics of avalanche photodiodes with a 10 period, 300 Å/300 Å, GaSb/AlSb superlattice multiplication layer. The dashed line shows the un-multiplied dark current. (b) Device dark current plotted as a function of the photo gain. The data was fitted to a power law $I=I_o(M)^p$, where p=1 for constant un-multiplied dark current.

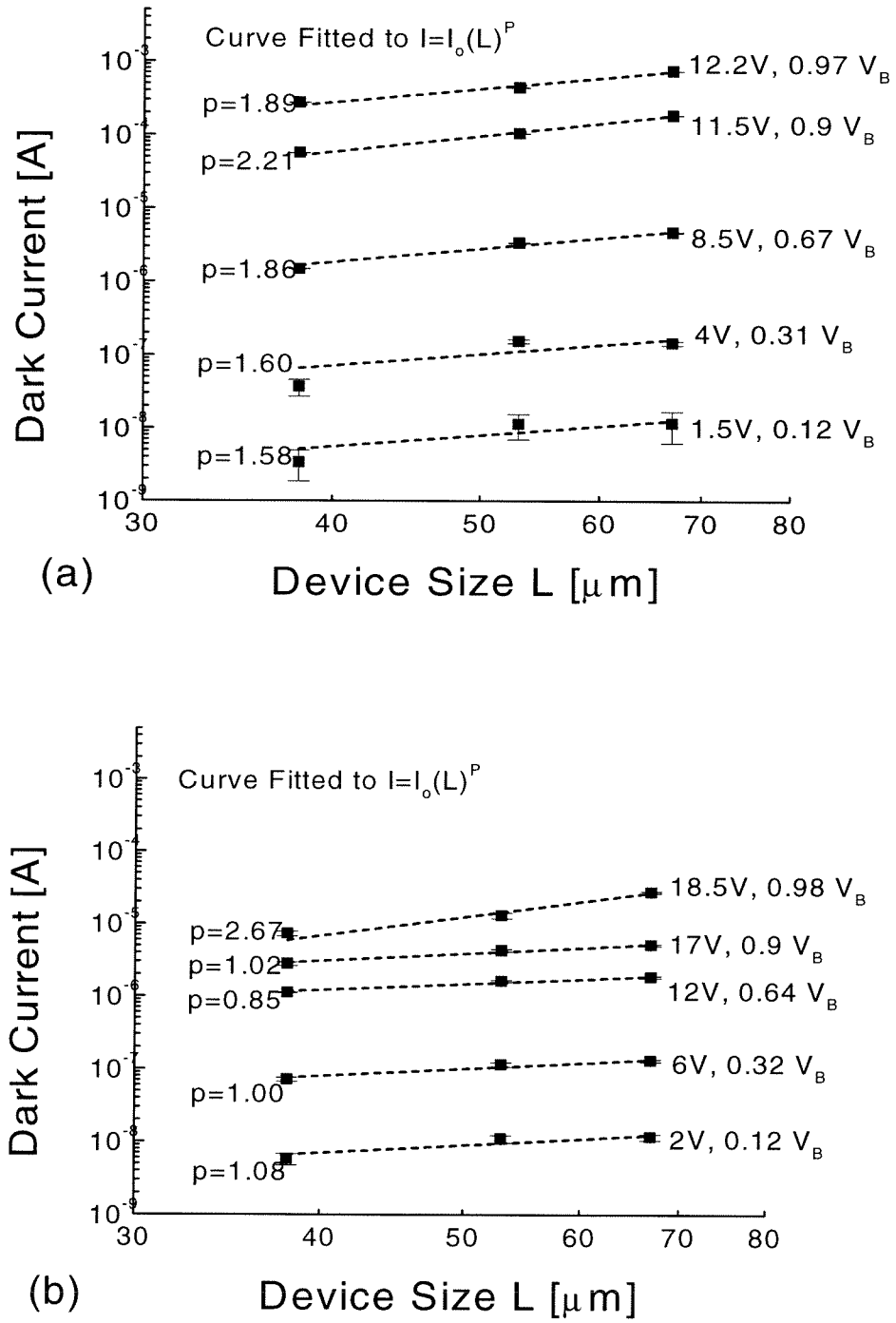

Figure 4.14: Dark current scaling with device size for APD's with (a) $Al_{0.04}Ga_{0.96}Sb$ multiplication layer and (b) GaSb/AlSb superlattice multiplication layer. The data is fitted to a power law $I=I_o(L)^p$, where L is the device size. The curve fit should yield p=2 for perfect scaling with device area and p=1 for perfect scaling with device perimeter.

types devices against device mesa size at different voltages. The slope of the curve indicated whether the leakage current scaled with device area or perimeter, and can be viewed as an index on the relative importance of bulk and surface leakage current. It can be seen that bulk tunneling current is significant in $Al_{0.04}Ga_{0.96}Sb$ devices due to the smaller bandgap of the multiplication layer. The superlattice dark current was much lower and varied linearly with device size until the very onset of avalanche break down. The surface character of the observed dark current implies that the fundamental limit in leakage suppression was not yet reached. With better processing and passivation techniques, the surface leakage can be readily reduced and the superlattice device performance further improved.

4.6.2 Quantum Efficiency at Low Bias

The superlattice gain layer exhibited quantum efficiency characteristics significantly different from its bulk counterpart. There was a strong dependence of collection efficiency on device bias at low voltages due to the presence of AlSb barriers in the multiplication region. As shown in Fig. 4.15, a bias as high as 10 V was needed to overcome the barrier and reach unity gain. This effect was similar to the heterostructure induced injection inefficiency for 781 nm light as discussed in Section 4.5.1. It is much more pronounced here because the carriers can become trapped in GaSb quantum wells and the band alignment in the multiplication region has a stronger dependence on voltage due to its low background doping level.

The carrier trapping effect also resulted in variations in quantum efficiency and photo gain with light intensity. As illustrated in Fig. 4.15, a higher reverse bias was needed to achieve the same quantum efficiency as the input light intensity was increased. The apparent photo gain also decreased when the device was under stronger illumination. This is because the photo-generated electrons and holes drifted in different directions and can become partially trapped in GaSb quantum wells at opposite ends of the multiplication region. The accumulation of these carriers tended to screen the applied electric field and reduce the carrier ionization rates, resulting in smaller

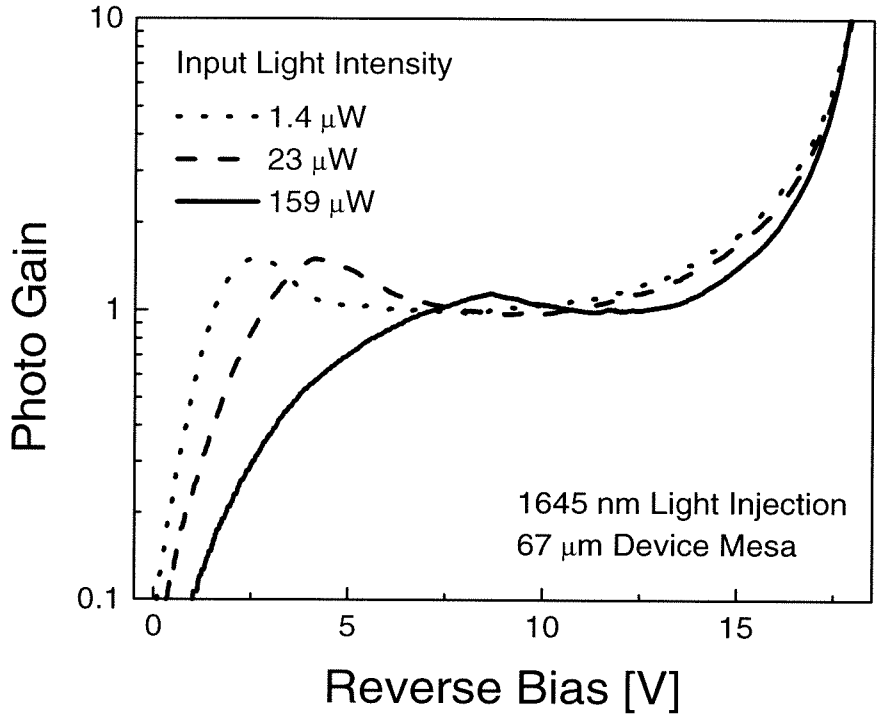

Figure 4.15: Photo response of the GaSb/AlSb superlattice avalanche photodiode at different light intensity levels. The data was obtained by using a 1645 nm laser light. Similar results were obtained from 781 nm and 1740 nm light sources.

photo gains at higher input light intensity [8].

It should also be mentioned that a small negative resistance region was observed in the photo gain curve at low levels of light injection. The resulting peak in photo gain curve became less prominent and shifted to a higher voltage when the input light intensity was increased. An explanation does not yet exist for this interesting phenomenon.

4.7 Summary and Conclusion

In summary, we have demonstrated antimonide avalanche photodiodes with sensitivity in the near infrared out to 1.74 μm. Devices with bulk $Al_{0.04}Ga_{0.96}Sb$ and GaSb/AlSb superlattice gain layers were both realized in a MBE grown structure

with a selectively doped, InAs/AlSb superlattice as the n-type layer. The avalanche photodiode dark current was found to critically depend on the n-type superlattice design and the resulting band offset at the p^-n^+ heterojunction. Early efforts were plagued by large tunneling current due the small band overlap between the n-type superlattice and the multiplication layer. This was remedied by using a InAs/AlSb superlattice with a three stage design which led to substantial improvements in device dark current and contact characteristics.

The ionization coefficients of the $Al_{0.04}Ga_{0.96}Sb$ gain layers were measured by using a two wavelength photo response setup. The result was consistent with hole impact ionization enhancement as was predicted by the spin-orbit split-off band resonance argument. However, the ionization measurement was to a certain extent compromised due to possible mixing of carrier injection and bias-induced quantum efficiency effect. Moreover, the $Al_{0.04}Ga_{0.96}Sb$ gain layer device exhibited a relative high level of dark current which tended to negate the detector sensitivity advantage gained from impact ionization enhancement. The results of the ionization and dark current study leads to the conclusion that hole ionization enhancement from spin-orbit split-off band resonance in $Al_{0.04}Ga_{0.96}Sb$ will be of only limited use because a high level of dark current is inherently associated with the narrow bandgap of the $Al_{0.04}Ga_{0.96}Sb$ multiplication layer.

Impact ionization rates in GaSb/AlSb superlattice gain layer devices were not measured due to absorption of long wavelength light by GaSb layers in the gain region and variation of photo gain with illumination intensity. However, the superlattice gain layers resulted in devices with much lower dark current and more pronounced avalanche characteristics. The observed dark current was due to surface leakage and can be readily improved from better processing and passivation. The superlattice multiplication layer was found to be more promising than its bulk counterpart because tunneling current is readily suppressed by barriers in the gain region while impact ionization may still be enhanced by separate band offset adjustment.

Bibliography

[1] S. M. Sze, *Physics of Semiconductor Devices*, John Wiley Sons. Inc., New York, 1981.

[2] K. F. Longenbach and W. I. Wang, *Appl. Phys. Lett.* **59**, 26 (1991).

[3] M. H. Woods, W. C. Johnson, and M. A. Lampert, *Solid–State Electron.* **16**, 381 (1973).

[4] G. E. Stillman and C. M. Wolfe, in *Semiconductors and Semimetals, Volume 12*, edited by R. K. Willard and A. C. Beer, Academic, New York, 1977.

[5] P. A. Wolff, *Phys. Rev.* **95**, 1415 (1954).

[6] S. Wang, *Fundamentals of Semiconductor Theory and Device Physics*, Prentice-Hall, Englewood Cliffs, NJ, 1989.

[7] T. Kagawa, Y. Kawamura, H. Asai, M. Naganuma, and O. Mikami, *Appl. Phys. Lett.* **66**, 993 (1989).

[8] R. E. Cavicchi, D. V. Lang, D. Gerhsoni, A. M. Sergent, H. Temkin, and M. B. Panish, *Phys. Rev. B* **38**, 13474 (1988).

Chapter 5 Tunnel Switch Diodes Based on AlSb/GaSb Heterojunctions

5.1 Introduction to Chapter

The second device investigated in this thesis is a tunnel switch diode (TSD) based on AlSb/GaSb heterojunctions. This chapter describes the design, growth, and characterization process which resulted in the first such device in the antimonide system. The device current-voltage characteristics and the effect of current stressing are examined in detail in order to deduce the TSD switching mechanism. These results are correlated with drift diffusion simulations which have been modified to account for the presence of a tunneling contact.

5.2 Motivation and Background

The tunnel switch diode, also known as the metal insulator semiconductor switch (MISS) [1] or controlled inversion device (CID) [2], was first discovered by Yamamoto while studying the properties of metal/SiO_2/n-Silicon/p-Silicon structures [3]. As shown in Fig 5.1, the device is characterized by a "S" shaped current-voltage (I-V) curve with a negative differential resistance (NDR) region much like that of a thyristor. It was found that the TSD can be switched between the high and low impedance branches of the I-V curve very rapidly. Switching times of less than 2 ns were obtained for large area devices [4].

Following the initial discovery, silicon TSD devices with tunnel barriers consisting of SiC [5], plolysilicon [6], amorphous silicon [7] and Ge [8] were also fabricated. The device has found unique applications in circuit design due to its large non-linearity, inherent speed, and integration capability which arises from its vertical structure. For

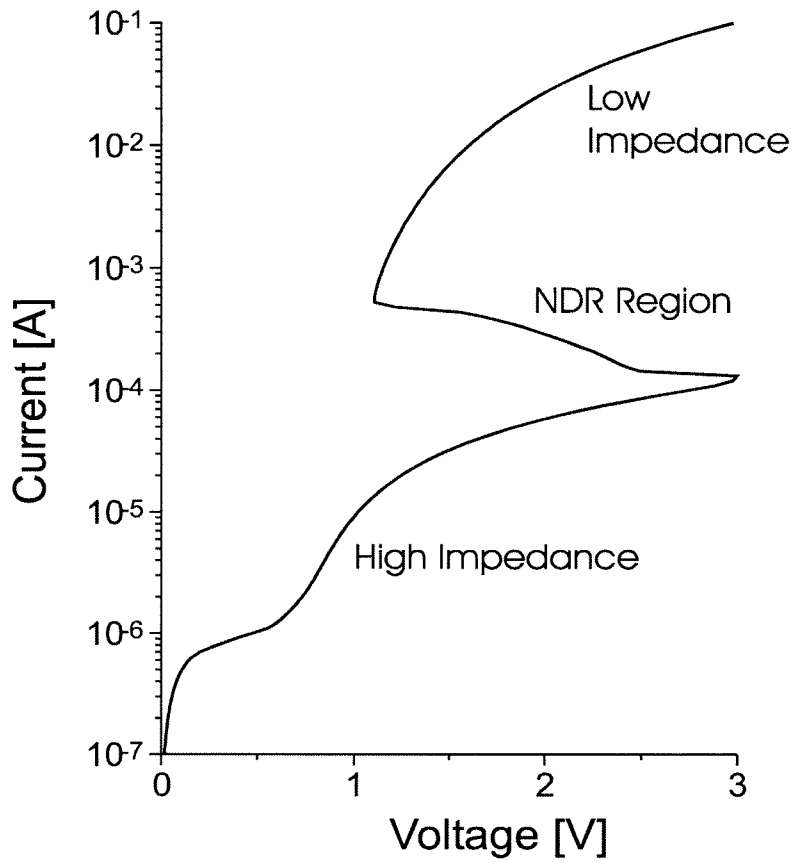

Figure 5.1: Thyristor like, "S" shaped I-V curve of a tunnel switch diode.

example, a static random access memory (SRAM) cell has been constructed from a single TSD element in the Si system [9]. Compared to rival conventional designs which require six transistors, the TSD-SRAM is both more compact due to its structural simplicity and faster because of the tunneling nature of the switching process.

There is much interest in an all antimonide TSD because such a device forms the much desired complement to the existing resonant interband tunneling diode (RTD) [11]. The "S" shaped I-V curve of the TSD is symmetrically opposed to the "N" shaped I-V curve of the RIT, and the two devices are in fact circuit duals of each other. The addition of a device with thyristor-like negative differential resistance will undoubtly bring more functionality to the burgeoning RIT-based antimonide high speed circuits [12]. From a scientific standpoint, the antimonide version of the device should advance understanding of TSD operation through another case study. The

role of the oxide tunneling barrier is not well understood in the Si device [13]. By replacing it with AlSb, which has a different barrier height and may have deep levels within its bandgap, more experimental evidence will be collected to shed light on the role of the barrier in TSD switching.

5.3 Tunnel Switch Diode Theory and Design

The tunnel switch diode structure generally consists of a tunnel barrier in series with a pn junction. As shown in Fig. 5.2, the antimonide implementation employs an AlSb barrier and a GaSb pn junction. For the pn junction polarity shown, the device is reverse biased when a negative voltage is applied to the AlSb barrier (not shown here). In this state, most of the bias is dropped across the pn junction and the device I-V characteristics follows that of a reverse biased pn diode.

When a small positive voltage is applied to the AlSb barrier, the device enters a high impedance state with most of the voltage dropped across the p-type GaSb epilayer. If the AlSb tunnel barrier is of the right thickness, electrons will partially accumulate in the p-GaSb layer and cause it to enter deep depletion (band diagram (a) in Fig. 5.2). The current in this high impedance state is due to generation in the p-GaSb layer. Hence it is proportional to the width of the depletion region and the square root of the applied bias.

As the voltage further increases, the device can be switched to the low impedance state in a number of ways. In the so called "punch through" mode of operation, the depletion region in p-GaSb extends deeper into the epilayer until it reaches the buried pn junction. Further bias causes the pn junction to be turned on, flooding the p-GaSb layer with electrons. If the AlSb tunnel barrier is not too thin, the electrons will accumulate near the interface between the p-GaSb and AlSb layers and create an inversion layer. The resulting high charge density at the interface is able to support a large electric field across the AlSb barrier, causing the tunneling current to increase. This results in high levels of hole injection which pulls down the hole Fermi level in p-GaSb and turns on the pn junction even more. This positive feedback mechanism

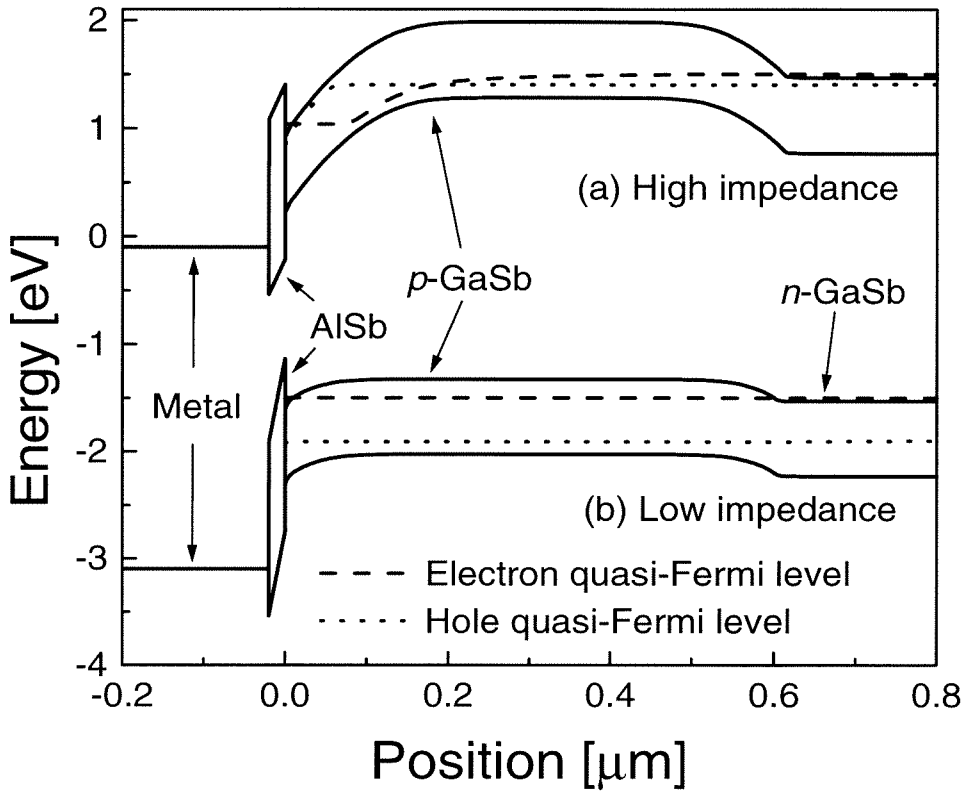

Figure 5.2: Band diagrams of an antimonide TSD under forward bias. (a) High impedance state with deep depletion in the p-GaSb epilayer. (b) Low impedance state with the pn junction turned on and most of the bias dropped across the AlSb barrier. The energy scale of the high and low impedance states are shifted for clarity.

continues until the device is switched into the low impedance state (band diagram (b) in Fig. 5.2). Since this process is initiate by "punching through" of the p-GaSb depletion layer to the buried pn junction, the switching voltage is given by the voltage required to deplete the entire p-GaSb layer:

$$V_{switch} = qN_c(w - w_o)^2/2\varepsilon_{GaSb} \tag{5.1}$$

where q is the electronic charge, w_o is the zero bias depletion width of the pn junction, and N_c,w, and ε_{GaSb} are the doping density, width, and dielectric constant of the p-GaSb epilayer, respectively [1].

If the doping level in the p-GaSb layer is sufficiently high, the electric field in the p-GaSb depletion layer may become large enough for avalanche processes to become significant before "punch through" occurs [1]. The avalanche action will cause electrons to accumulate at the p-GaSb/AlSb interface and start the same chain of events that lead to switching. The switching voltage for this avalanche induced process is given by

$$V_{switch} = 60(E_g/1.1)^{3/2}(N_B/10^{16})^{-3/4} \tag{5.2}$$

where E_g is the room temperature bandgap in eV, and N_B is the background doping in cm^{-3} [14].

A third possibility for switching exists when the metal electrode Fermi level goes below the p-GaSb valence band edge, allowing large hole currents to tunnel into the p-GaSb layer and turn on the buried pn junction [9]. This tends to occur for thick barriers with relatively strong electron accumulation at the AlSb/p-GaSb interface. In this case, a significant portion of the bias is dropped across the barrier in the high impedance state.

As shown by the band diagram (b) in Fig. 5.2, once in the low impedance state, most of the bias is dropped across the AlSb barrier and the device I-V characteristics assume the exponential behavior of a tunnel barrier. The low impedance state is sustained as long as there is enough electron current to support the inversion layer at the GaSb/AlSb interface and maintain the large bias drop across the tunnel barrier, or as long as there is enough hole tunneling into the p-GaSb layer to keep the pn junction forward biased. If these currents become low enough to be consumed by recombination at the pn junction, the device switches back to the high impedance state.

From the above discussion, it should be apparent that the tunnel barrier plays a critical role in the TSD switching action. In order for switching to occur, the tunnel barrier must have the right barrier height and thickness. If the barrier height is too low or the barrier is too thin, electrons will leak through and not accumulate at the

p-layer/barrier interface. Without a depletion region in the p-layer, the potential energy of the p-GaSb layer will follow that of the surface electrode. This means that the device will assume the highly conductive characteristics of a forward biased pn junction and will always be in a low impedance state (the pn junction is the conduction bottle neck here due to the ineffectiveness of the tunnel barrier). If the barrier height is too large or the barrier is too thick, the carriers are effectively blocked and there is no place for the accumulated electrons to escape. This will cause the surface of the p-type layer to invert and screen the field from the metal electrode. In this case, most of the bias falls across the barrier instead of the depletion region in the p-type layer. Since the barrier is not very conductive, the device is stuck in a high impedance state.

For Si devices, switching was obtained for oxide barriers with thicknesses that ranged from 15 Å to 40 Å [15, 16]. The AlSb barrier in the antimonide device is typically much thicker (greater than 100 Å) due to its smaller barrier height. To maximize the AlSb barrier height, the polarity of the pn junction is chosen such that the AlSb layer partially blocks the electron flow in the high impedance state. This is the desired configuration because AlSb is a more effective barrier for electrons than holes, i.e. the conduction band offset between AlSb and GaSb is 1.15 eV at the Γ point and 0.55 eV at the X point valley, which is larger than the valance band offset of 0.4 eV between these materials.

The typical structure of the antimonide TSD is shown in Fig. 5.2. Different devices were fabricated to study the structural dependence of device characteristics and deduce the TSD switching mechanism. As listed in Table 5.1, the AlSb barrier was varied from 100 Å to 500 Å to delineate its effect on switching. Since the p-type GaSb epilayer was unintentionally doped, the devices were expected to operate in the punch through mode with a switching voltage strongly dependent on the epilayer thickness. Hence the p-type GaSb layer thickness was varied among 100 Å AlSb samples to confirm this effect.

5.4 Growth and Fabrication

The antimonide tunnel switch diodes were grown by molecular beam epitaxy on Te doped (n=1x10^{18}/cm^3) wafers. Due to the lack of a suitable n-type dopant, the GaSb pn junction was formed at the substrate surface by depositing an unintentionally doped p-type GaSb buffer layer (p=5x10^{16}/cm^3). To improve the quality of the pn junction, the substrate was etched and thoroughly heated for oxide desorption prior to buffer layer growth. Note that the superlattice doping scheme described in Chapter 3 could not be applied here because the n-type superlattice could not be grown directly onto the substrate. The GaSb buffer layer constituted the p-type epilayer in the device and was grown at a substrate temperature of 520 °C. The AlSb barriers were grown at a slightly higher temperature, and a 30 second Sb soak was applied at the GaSb/AlSb interface to smooth out the growth front. At the end of the growth, the structure was capped by a 50 Å GaSb layer to prevent oxidation of the AlSb barrier.

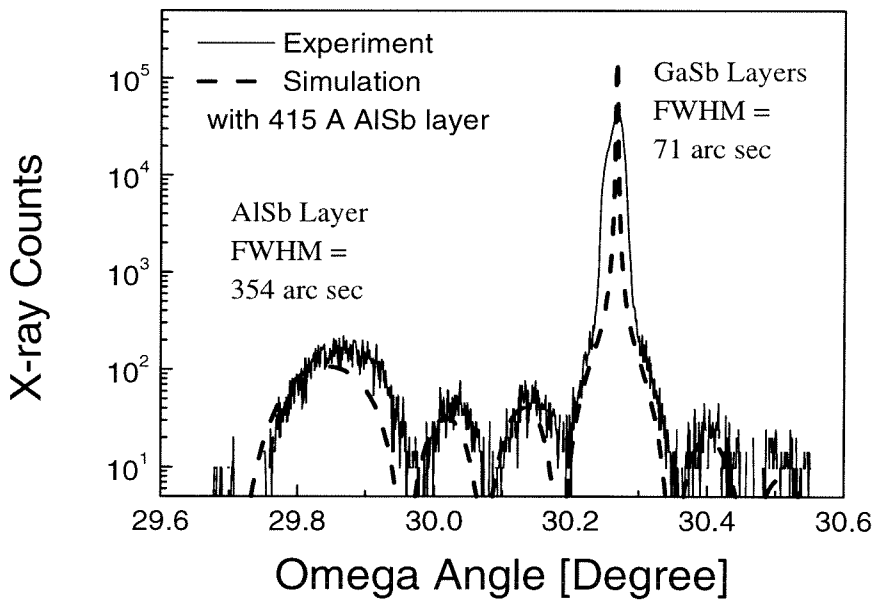

Figure 5.3: X-ray diffraction scan of an antimonide TSD structure.

Figure 5.3 shows the high resolution X-ray diffraction scan of a typical structure. The high quality of the growth was evidenced by the narrow full width at half maximum (FWHM) of 18 arc seconds for the GaSb epitaxial layer and the close agreement

between the experimental data and the simulated curve.

Following growth, the wafers were metallized *ex situ* with Au in a sputter deposition tool. Indium left over from the growth served as the back contact. Device mesas were defined by standard photolithography and ranged in size from 38 μm to 200 μm. Chlorine assisted dry etching was used as the final etch down and yielded highly reproducible surfaces with few etch defects.

5.5 Characterization Results

The TSD devices were characterized by using the HP 4156 semiconductor parameter analyzer. To accommodate the "S" shaped negative differential resistance region in the I-V curve, the analyzer was run in the current sweep mode instead of the usual voltage sweep mode. This prevented dramatic swings in device current from the switching action and allowed recording of the full I-V curve in one sweep. The main results of the characterization study are summarized in Table 5.1, which shows the structural dependence of TSD operation and the effect of current stressing on TSD switching.

Table 5.1: Antimonide TSD structures fabricated and the observed switching characteristics. Device size was 67 μm.

Device configuration		Switching voltage and current	
AlSb barrier	*p*-GaSb epilayer	Initial values	After stressing
100 Å	0.2 μm	2.3 V/2.0 mA (unstable)	1.2 V/1.0 mA
100 Å	0.4 μm	3.5 V/3.0 mA	1.2 V/1.0 mA
100 Å	0.6 μm	3.0 V/2.1 mA	1.3 V/0.2 mA
200 Å	0.6 μm	3.1 V/1.8 mA	1.2 V/0.3 mA
300 Å	0.6 μm	no switching observed	
500 Å	0.6 μm	no switching observed	

5.5.1 Effect of Barrier and Epilayer Thickness on Switching

As listed in Table 5.1, switching behavior was obtained for all devices with 100 Å and 200 Å AlSb barrier thicknesses. The typical I-V curve of a switching device is shown in Fig. 5.4.

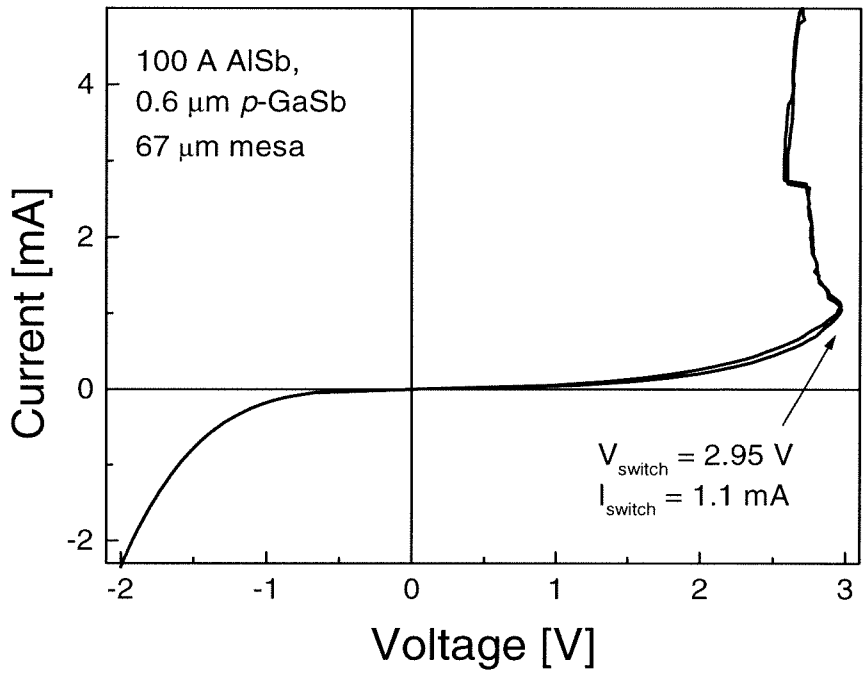

Figure 5.4: Typical I-V characteristics of antimonide TSD's.

It can be seen that the reverse current of the device was large and varied exponentially with voltage, indicating that tunneling through the buried pn junction was significant. The less than ideal quality of the pn junction was expected since it was formed at the substrate surface.

In the forward direction, switching from the high impedance state to the low impedance state occurred at voltages from 2.3 V to 3.5 V. The switching current densities ranged from 10 A/cm^2 to 300 A/cm^2, and did not change appreciably when the AlSb barrier thickness was increased from 100 Å to 200 Å for 0.6 μm epilayer samples. This did not agree with the model established by Simmons et al., which predicts lower switching currents for thick tunneling barriers [15]. Similar insensitivity of switching current to barrier thickness has also been observed in Si devices [16].

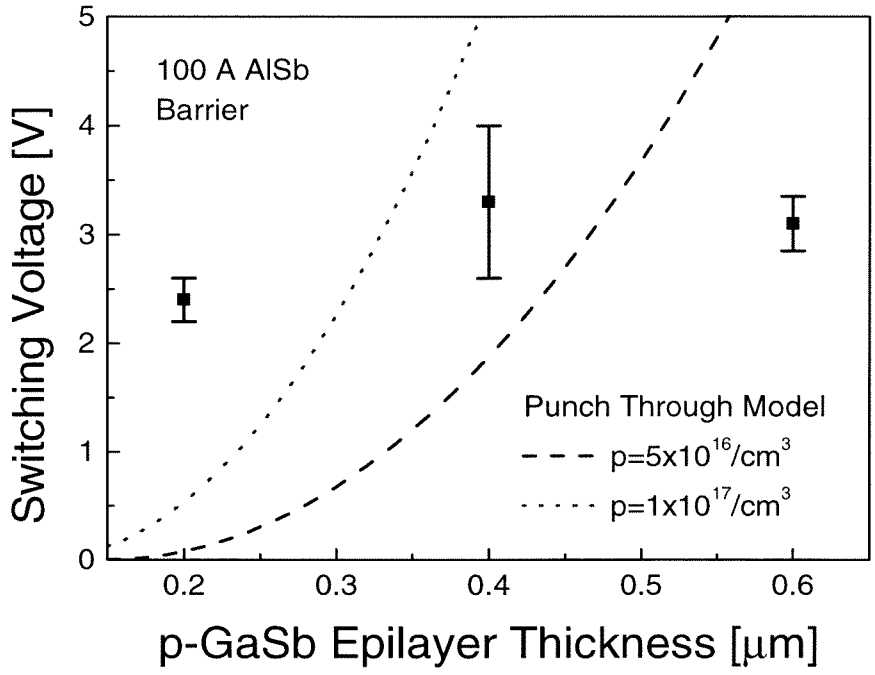

Figure 5.5: Effect of p-GaSb epilayer thickness on TSD switching voltage.

Figure 5.5 shows the observed dependence of switching voltage on p-GaSb epilayer thickness for 100 Å AlSb barrier samples. The predicted results from the punch-through model are also plotted in the same figure for comparison. It can be seen that the switching voltage was relatively independent of epilayer thickness and did not follow the predicted trend of the punch-through model. This is a surprising result because the device was expected to work in the punch-through mode due to the low background doping level of the p-GaSb epilayer. The switching could not be from the avalanche initiated process because it would have required a switching voltage of at least 10 V according to equation 5.2. This leaves the distinct possibility that the switching action was initiated by holes that tunnel across the AlSb barrier as the Fermi level in the metal electrode drops below the valence band edge of the p-GaSb layer. This is a plausible scenario for antimonide TSD's because of two factors:

1. The AlSb barriers were relatively thick and may support strong accumulation of elections at the GaSb/AlSb interface. This means that the field in the AlSb barrier can be fairly large and a significant amount of bias was dropped across

the barrier in the high impedance state, pulling the electrode Fermi level down with respect to the p-GaSb valence band edge.

2. The GaSb bandgap is smaller than the Si bandgap and it takes a smaller bias drop across the AlSb barrier to shift the Fermi level of the metal electrode to below the p-GaSb valence band edge.

The experimental evidence which may counter this hypothesis is that the switching voltage did not change much as the AlSb barrier thickness was increased from 100 Å to 200 Å. However, this may be explained by the fact that a larger bias was dropped across the thicker barrier due to stronger electron accumulation at the AlSb/GaSb interface.

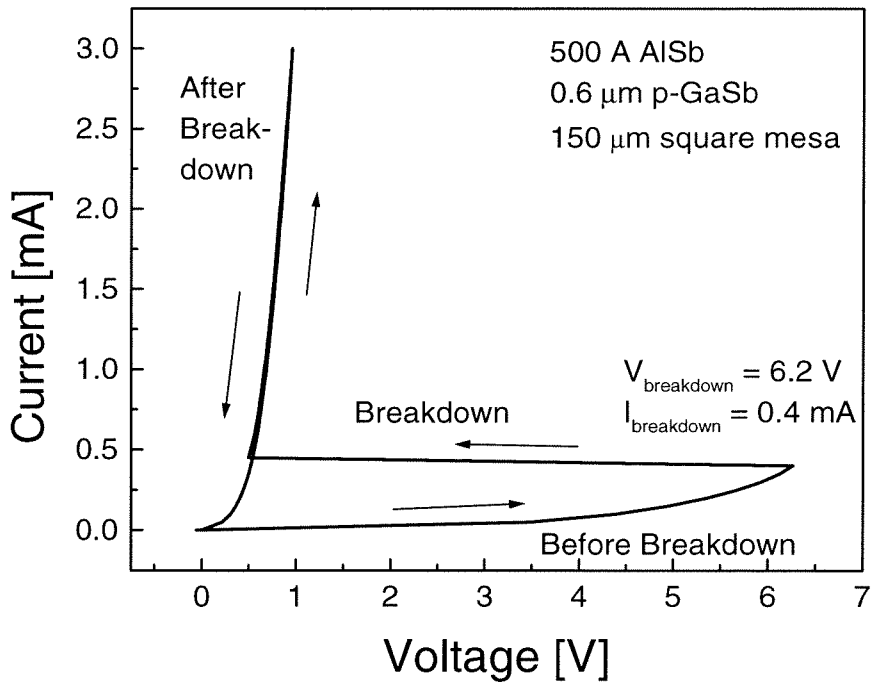

Figure 5.6: I-V characteristics and break down behavior of devices with thick AlSb barriers.

When the AlSb barrier was increase to beyond 300 Å, no switching was observed. As shown in Fig. 5.6, the device instead remained in a high impedance state until it physically broke down at a voltage of 5 to 7 volts. The post break down I-V

characteristics were pn diode like, indicating that the break down occurred in the AlSb barrier. This was as expected since most the bias was dropped across the barrier in the high impedance state of thick barrier devices.

5.5.2 Effect of Current Stress and Dual Mode Switching Behavior

In Si TSD studies, it was observed that the low impedance branch of the I-V curve shifted slightly upward when the device was current stressed [16]. As shown in Fig. 5.7, similar behavior was observed for the antimonide device. There was a visible shift in the low impedance branch as the device current was increased. The antimonide TSD physically broke down when the current density reached 10^3 A/cm^3. Similar to thick barrier devices, post breakdown I-V characteristic was pn diode like, indicating that the break down occured in the AlSb layer and most of the bias was dropped across the barrier in the low impedance state of the switching device.

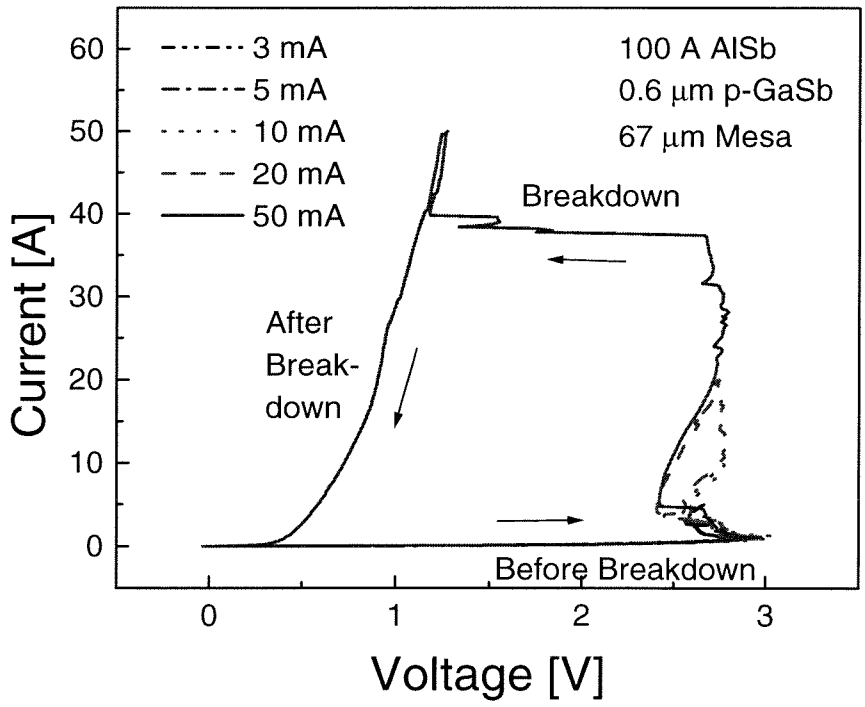

Figure 5.7: TSD break down from current stressing.

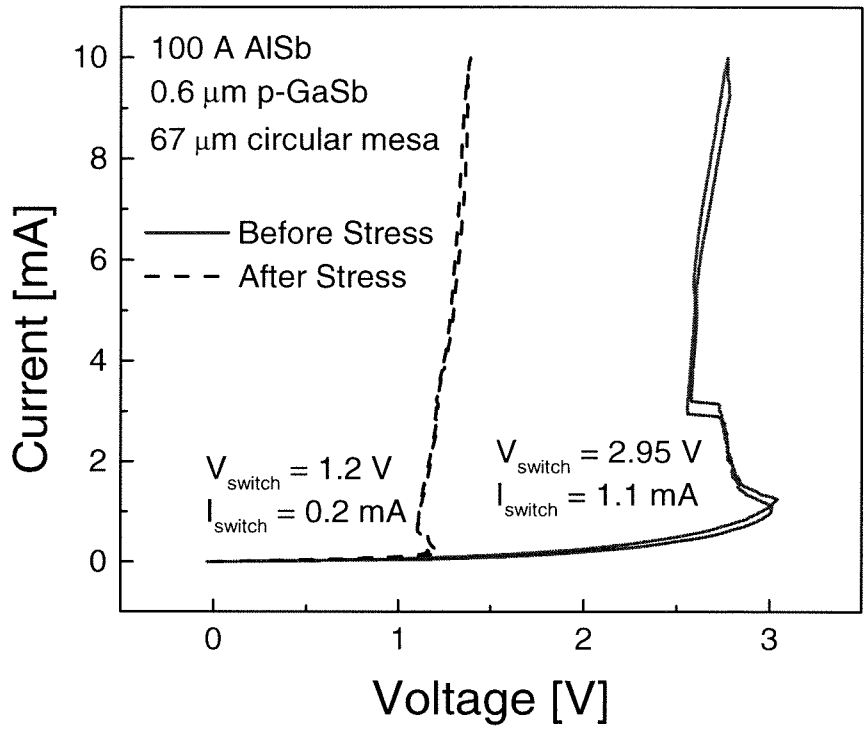

Figure 5.8: TSD I-V characteristics before and after current stressing.

For some devices, the switching voltages and currents were drastically modified following significant current stressing. As listed in Table. 5.1, this was observed for all device configurations that yielded switching. Figure 5.8 shows the typical I-V characteristics before and after current stressing. Unlike the gradual "burn in" process observed in Si devices, the switching voltages of the antimonide device tended to change abruptly during current stress and clustered around a fixed value (1.2 V). This is illustrated Fig. 5.9 where the virgin and after stress switching points of a number of devices are plotted. It is as if there are two low impedance branches in the I-V curve with two sets of switching voltages and currents. Most switching devices exhibited the branch with the higher switching voltage and current when first examined and moved to the other branch following current stressing. However, a few devices started out on the branch with the lower set of switching voltage and current. What is most interesting is that it was possible to "hop" the I-V curve from one low impedance branch to another by increasing the current level in the device.

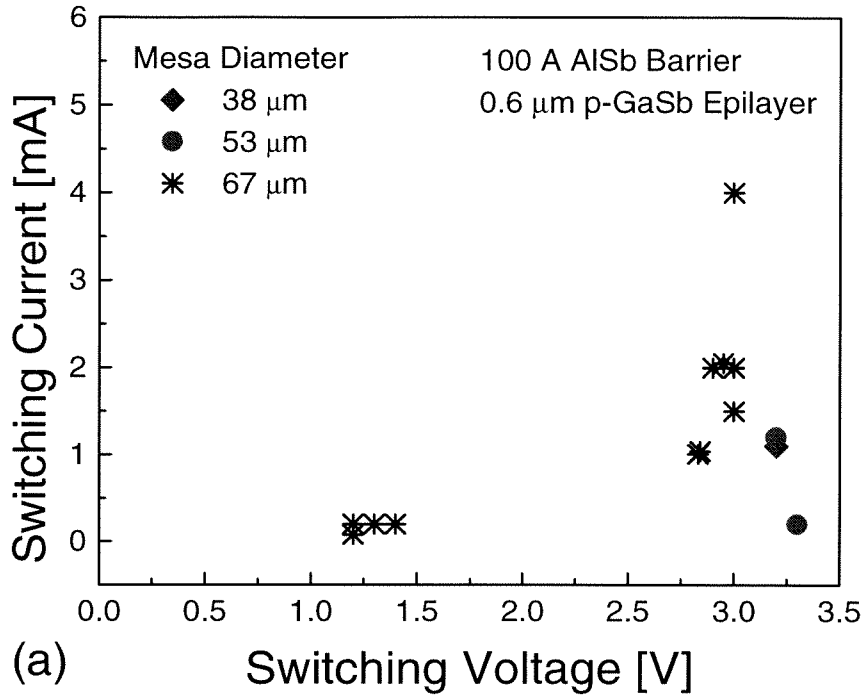

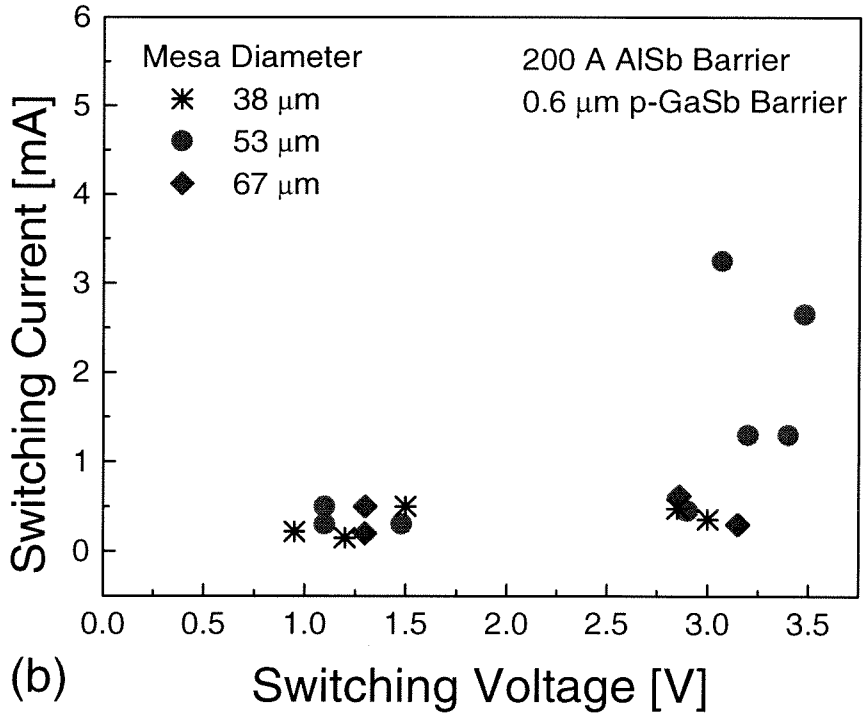

Figure 5.9: Clustering of switching voltages and currents. (a) 100 Å AlSb barrier, 0.6 μm p-GaSb epilayer. (b) 200 Å AlSb barrier, 0.6 μm p-GaSb epilayer.

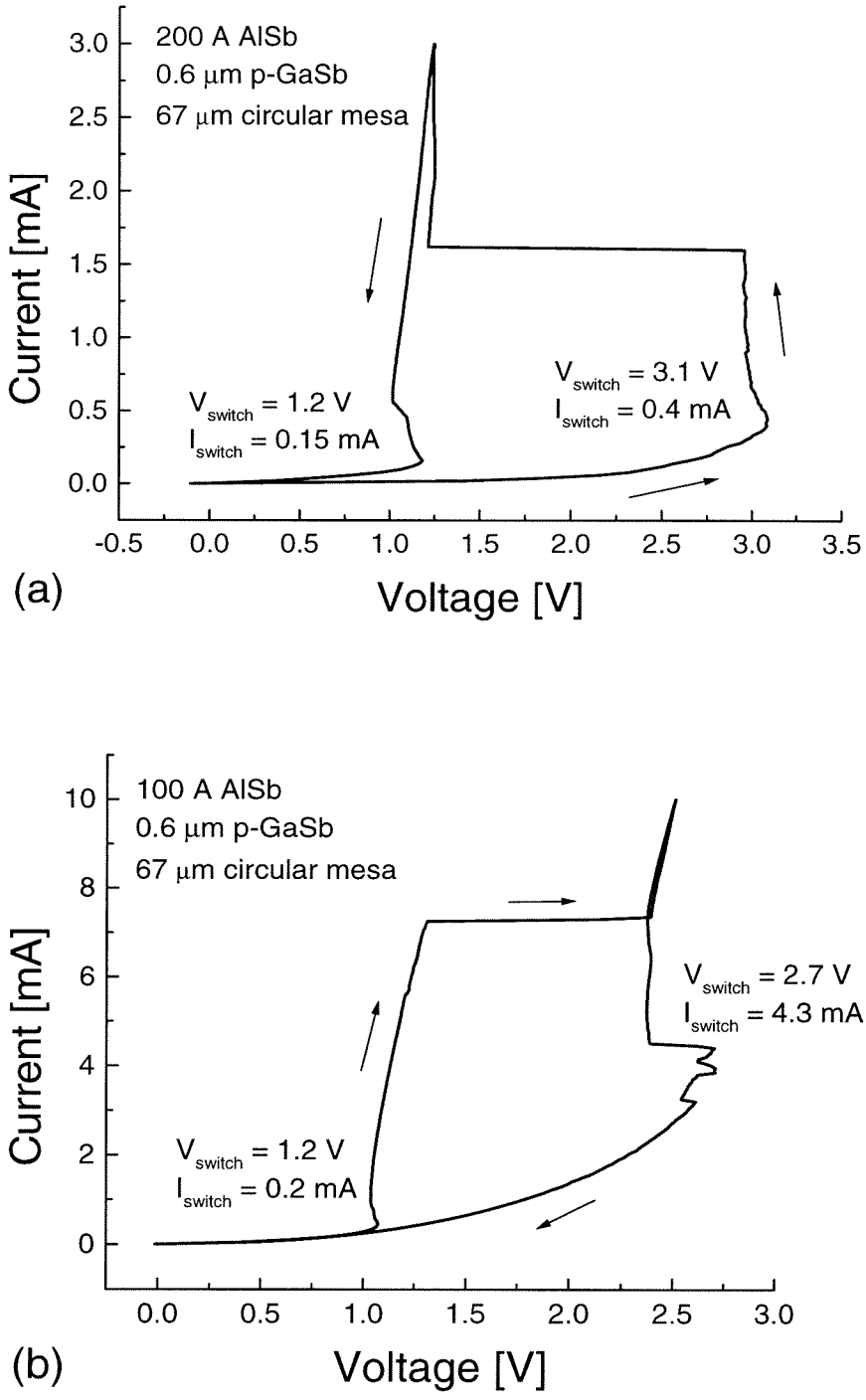

Figure 5.10: Hopping between stable I-V curves due to current stressing. (a) From high branch to low branch. (b) From low branch to high branch.

The "hopping" action could not be precisely controlled but was reversible, i.e. device I-V curves were observed to move back and forth between the two low impedance branches. This is illustrated by the double I-V sweeps in Fig. 5.10 where the current was swept up to a maximum value and then swept down back to the origin. In Fig. 5.10(a), the device was in the high branch of the I-V curve on the upward sweep and was induced to the low branch at a current of 1.5 mA. In Fig. 5.10(b), the device started out in the low branch on the upward sweep and abruptly moved over to the high branch when the current reached 7 mA.

The stress induced dual mode switching behavior again pointed towards a TSD switching process initiated by holes that tunnel across the AlSb barrier. We speculate that a deep level in AlSb was activated and deactivated by the large current and acted as a sink for the accumulation charge at the AlSb/GaSb interface. When the deep level was activated, charges can build up in the AlSb barrier layer, causing the electric field in the AlSb barrier to assume a sharper profile and a larger portion of the applied bias to drop across the barrier. This will result in a greater shift downward of the electrode Fermi level relative to the p-GaSb valence band edge, causing a decrease in the switching voltage.

5.6 Simulations

Since the TSD switching was strongly dependent on the AlSb barrier thickness, a computer model was used to simulate the I-V characteristics of device structures with different AlSb barriers. The simulation was previously developed by E. S. Daniel et al. for study of Si TSD devices [13, 17]. It was based on the Poisson and the carrier continuity equations [18] with boundary conditions modified to account for the tunneling contact, i.e.,

$$\nabla^2\phi - \frac{q}{\epsilon}(n - p - C) = 0 \tag{5.3}$$

$$\vec{\nabla} \cdot \vec{J}_n - qR(\phi, n, p) = 0 \tag{5.4}$$

$$\vec{\nabla} \cdot \vec{J}_p + qR(\phi, n, p) = 0 \tag{5.5}$$

with

$$\vec{J}_n = qD_n\vec{\nabla}n - q\mu_n n\vec{\nabla}\phi \tag{5.6}$$

$$\vec{J}_p = -qD_p\vec{\nabla}p - q\mu_p p\vec{\nabla}\phi \tag{5.7}$$

where ϕ is the electric potential, n and p are the electron and hole concentrations, q is the electron charge, ϵ is the semiconductor dielectric constant, C is the net concentration of ionized dopants $(N_d^+ - N_a^-)$, $\vec{J}_n$ and $\vec{J}_p$ are the electron and hole current densities, R is the net recombination rate, D_n and D_p are the electron and hole diffusion constants, and μ_n and μ_p are the electron and hole nobilities. The boundary conditions at the surface of the barrier are determined by the generation-recombination component and the tunneling current according to

$$\vec{e}_n \cdot \vec{J}_n = -qR_s + J_{n\,calc} \tag{5.8}$$

$$\vec{e}_n \cdot \vec{J}_p = qR_s + J_{p\,calc} \tag{5.9}$$

where $\vec{e}_n$ is a unit vector perpendicular to the AlSb/GaSb interface, R_s is the generation-recombination rate and $J_{n\,calc}$ and $J_{p\,calc}$ are the calculated electron and hole tunneling currents respectively [13].

To reduce the computational load, the equations were first discretized by using the Scharfetter-Gummel scheme [18, 19, 20] and the resulting set of nonlinear algebraic equations were solved iteratively by using the Newton-Raphson method. The multi-valued nature of the TSD I-V curve contributed much to the complexity of the simulation. In the negative differential resistance region, the device presented two stable current values for a fixed voltage, hence the convergence of the simulation to a particular solution was strongly dependent on the initial condition. The high impedance branch was obtained by adapting the conventional method where the previous voltage solution was the starting iteration point for the present voltage. The low impedance state was accessed by using a higher carrier life time, which favored diffusion of electrons from the substrate through the pn junction up to the barrier.

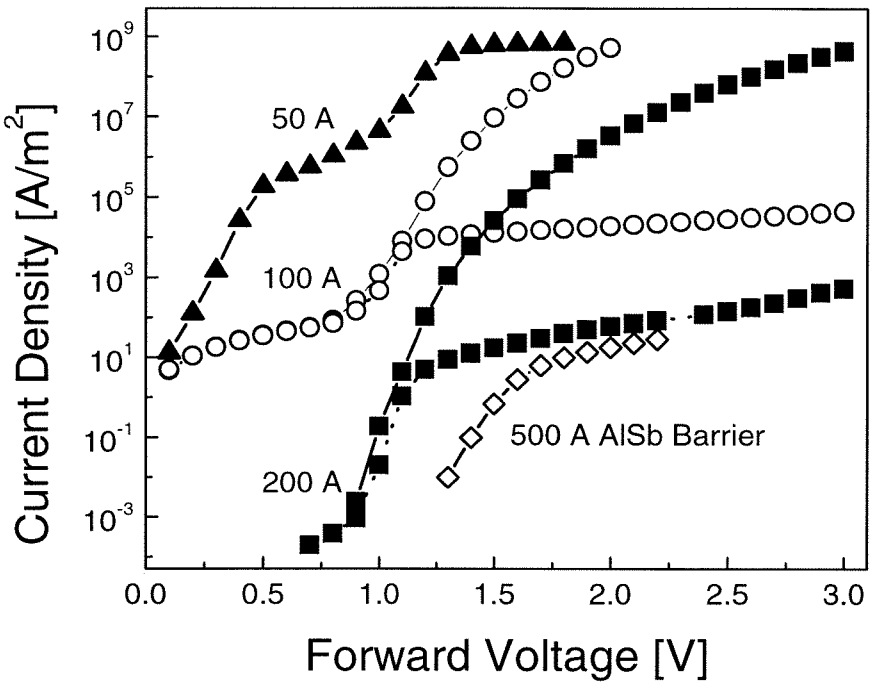

Figure 5.11: Simulated characteristics for TSD devices with 0.6 μm p-GaSb epilayer and different AlSb thicknesses. Bistable states were obtained for 100 Å and 200 Å barrier thicknesses.

The carrier life time was relaxed back to its original value once the solution converged towards a point on the low impedance branch. This point was subsequently used as the starting point to iteratively generate the rest of the low impedance branch.

Figure 5.11 shows the simulated I-V characteristics of TSD devices with AlSb barriers ranging from 50 Å to 500 Å. It can be seen that only the low impedance state existed for the 50 Å AlSb barrier device whereas the 500 Å barrier device yielded only the high impedance state. Dual impedance state behavior was obtained for AlSb barrier thicknesses of 100 Å and 200 Å, which agreed with experimental findings.

5.7 Summary and Conclusion

The main achievement in this section is the first time fabrication of a tunnel switch diode in the antimonide system. Successful TSD operation was found to depend critically on the AlSb barrier thickness. Thyristor like, "S" shaped I-V curves were obtained for structures with AlSb barriers less than 300 Å thick, as was predicted by the drift diffusion simulation model. The switching voltage and currents of the working devices had a weak dependence on the barrier and epilayer thickness and did not agree with the punch-through or avalanche model of operation. Based on the experimental observations, we propose that switching in the antimonide device is initiated by holes that tunnel across the AlSb barrier as the Fermi level in the metal electrode drops below the valence band edge of the p-GaSb epilayer. This switching mechanism differs from that of the Si device and is a result of the thicker tunnel barrier and narrower bandgap of the epilayer employed in the antimonide device.

Due to the relative novelty of the TSD device and the immaturity of the antimonide materials, the new device exhibited a number of unexpected behaviors. It was found that the I-V curves can be significantly altered by current stressing. There appeared to be two branches of the low impedance states with well defined switching voltages. The device can "hop" between the two sets of I-V curves when subjected to high levels of current stress. We speculate that this was due to charging and discharging of a deep level in the AlSb barrier. Such non-idealities indicate the importance of developing a better understanding of the AlSb barrier and the AlSb/GaSb interface as well as the need for high quality antimonide heterostructures.

Bibliography

[1] J. G. Simmons and A. El-Badry, *Solid–State Electron.* **20**, 955 (1977).

[2] H. Kroger and H. A. R. Wegener, *Appl. Phys. Lett.* **27**, 303 (1975).

[3] T. Yamamoto and M. Morimoto, *Appl. Phys. Lett.* **20**, 269 (1972).

[4] T. Yamamoto, K. Kawamura, and H. Shimizu, *Solid–State Electron.* **19**, 701 (1976).

[5] J. D. Hwang, Y. K. Fang, K. H. Chen, and H. Y. Chiu, *IEEE Trans. Electron Devices* **42**, 2246 (1995).

[6] N. T. Ali and R. J. Green, *IEEE Trans. Electron Devices* **42**, 1978 (1995).

[7] Y. K. Fang, K.-H. Wu, and C.-Y. Tsao, *IEEE Trans. Electron Devices* **44**, 34 (1997).

[8] H. Kroger and H. A. R. Wegener, *Solid–State Electron.* **21**, 643 (1978).

[9] H. J. Levy, Thesis, California Institute of Technology, 1995.

[10] H. J. Levy and T. C. McGill, U.S. Patent # 5,535,156, 1996.

[11] J. R. Söderström, D. H. Chow, and T. C. McGill, *Appl. Phys. Lett.* **55**, 1094 (1989).

[12] D. H. Chow, H. L. Dunlap, W. Williamson, III, S. Enquist, B. K. Gilbert, S. Subramaniam, P.-M. Lei, and G. H. Bernstein, *IEEE Electron Device Lett.* **17**, 69 (1996).

[13] E. S. Daniel, Thesis, California Institute of Technology, 1997.

[14] S. M. Sze, *Physics of Semiconductor Devices*, John Wiley Sons. Inc., New York, 1981.

[15] S. E-D. Habib and J. G. Simmons, *Solid–State Electron.* **22**, 181 (1979).

[16] P. O. Pettersson, A. Zur, E. S. Daniel, H. J. Levy, O. J. Marsh and T. C. McGill, *IEEE Trans. Electron Devices* **45**, 286 1998.

[17] E. S. Daniel, X. Cartoixà and T. C. McGill, to be published.

[18] S. Selberherr, *Analysis and Simulation of Semiconductor Devices*, Springer-Verlag, Wien, Austria, 1984.

[19] W. L. Engl and H. K. Dirks and B. Meinerzhagen, *Proc. IEEE* **71**, 10 (1983).

[20] C. M. Snowden, *Introduction to Semiconductor Device Modeling*, World Scientific, Singapore, 1986.

Part II

Ballistic Electron Emission Microscopy Study of III-V Heterostructures

Chapter 6 Ballistic Electron Emission Microscopy Theory and Experiment

6.1 Introduction to Chapter

It should be apparent from Part I of this thesis that band offsets and the interface properties of heterostructures play important roles in device research. In the avalanche photodiode work, the band offset at the pn interface was critical to dark current suppression. In the antimonide TSD work, device switching was strongly influenced by the band structure of AlSb barrier and surface states at the AlSb/GaSb interface. These critical properties are usually obtained from characterization techniques such as X-ray photo electron spectroscopy (XPS), photo electric, I-V, and C-V measurements. The drawback of these conventional approaches is that the results are laterally averaged over the whole interface or at least over macroscopic dimensions of more than a few μm. In Part II of this thesis, we describe local probing of interface properties by using ballistic electron emission microscopy (BEEM). This chapter serves as a short introduction and covers the basic theory and some important experimental issues relevant to the BEEM technique. The BEEM experimental apparatus used for subsequent study is also described.

6.2 BEEM Theory

6.2.1 Basic Operation of BEEM

The basic operation of BEEM is illustrated in Fig. 6.1. It is a three terminal technique based on the scanning tunneling microscopy (STM) setup [1, 2]. BEEM samples typically consist of a thin conductive layer, known as the base layer, on top of a

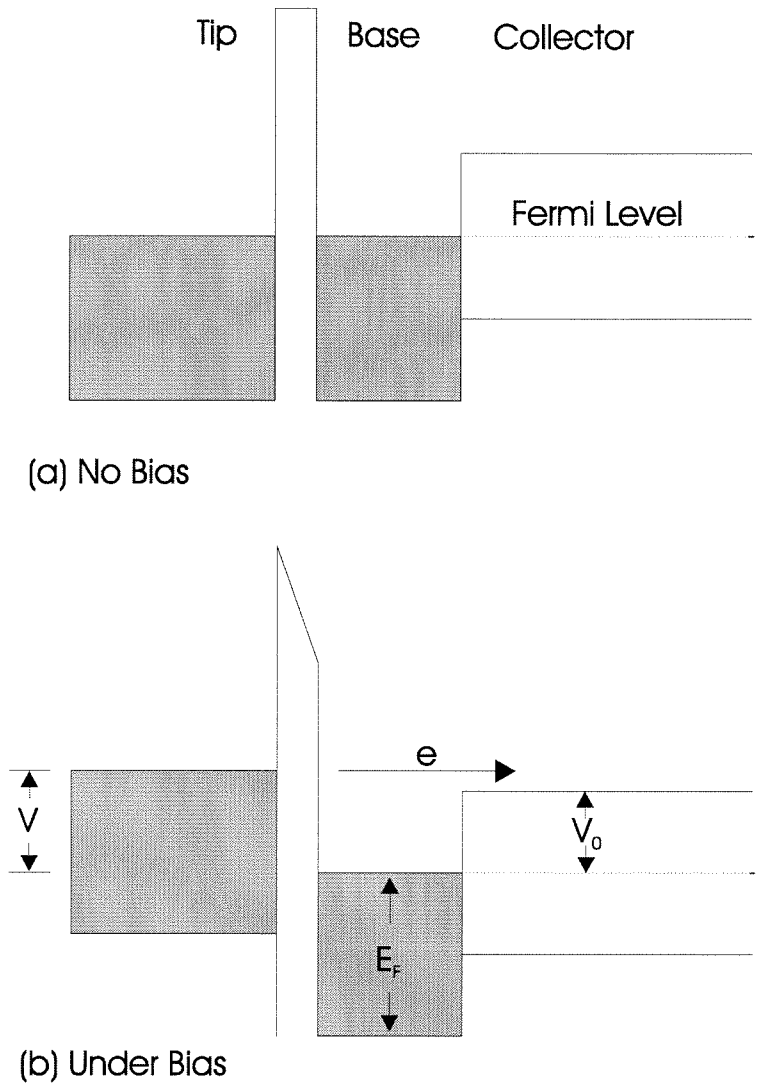

Figure 6.1: Basic operation of BEEM.

semiconductor of interest. The tip and base terminals support STM tunnel current while a new collector terminal at the back of the sample collects elections that leak into the semiconductor. At low tip bias, no BEEM collector current is observed because electrons injected from the tip do not have enough energy to overcome the potential barrier at the base collector interface. As the tunneling voltage increases and the STM tip potential rises above the conduction band edge of the underlying semiconductor, electrons can travel ballistically across the thin base region and enter the semiconductor unimpeded, giving rise to a BEEM collector signal.

The BEEM technique can be used to characterize samples in two ways: if the tip is held at a high enough bias for hot electron injection into the semiconductor, an image of the buried interface can be acquired from the BEEM collector signal while the STM image of the surface topography is being generated. Since the collector signal is dependent on hot electron transport into the underlying semiconductor, transport non-uniformities at the buried interface is directly imaged. Alternatively, the transport properties of a local area can be examined in detail by holding the STM tip stationary and observing the variation in BEEM collector current as the STM tip voltage is increased. This is known as BEEM spectroscopy. During this process, no external bias is applied between the collector and base terminals. The STM base current is also held constant by changing the tip sample separation as the tip bias is increased, which ensures that any change in the small collector signal reflects hot carrier injection into the semiconductor and not fluctuations in the large base current.

6.2.2 Parabolic Turn On Model

A model for the basic operation of BEEM has been proposed by Bell and Kaiser [2], who are the original inventors of the technique. They argued that the transverse momentum $k_{\|}$ of the electron should be conserved at the base collector interface in the absence of scattering. As shown in Fig. 6.2, this causes refraction of the electrons at the base collector interface, which gives rise to a critical angle of entry for propagation into the semiconductor. At bias voltage V, the maximum kinetic energy of the incident electron is $eV + E_F$ in the base layer and reduces to $eV - eV_0$ in the collector layer (Fig. 6.1). Since $k_{\|}$ is the largest when the transverse component accounts for all the electron energy in the semiconductor, the maximum transverse momentum is given by $k_{\|}^{max} = \sqrt{2m_s(eV - eV_0)/h^2}$. This results in a critical angle of incidence:

$$sin^2\Theta_c = \frac{(k_{\|}^{max})^2}{k^2} = \frac{m_s}{m}\frac{eV - eV_0}{eV + E_F} \tag{6.1}$$

Due to the small effective mass m_s of the semiconductor and the large Fermi en-

ergy E_F of the metal base layer, Θ_c is usually quite small and only electrons with small transverse momenta in the base may be collected. Thus any scattering in the base merely reduces the number of electrons collected and does not affect resolution. This focusing effect is the basis for the high lateral resolution capability of BEEM imaging [2, 3].

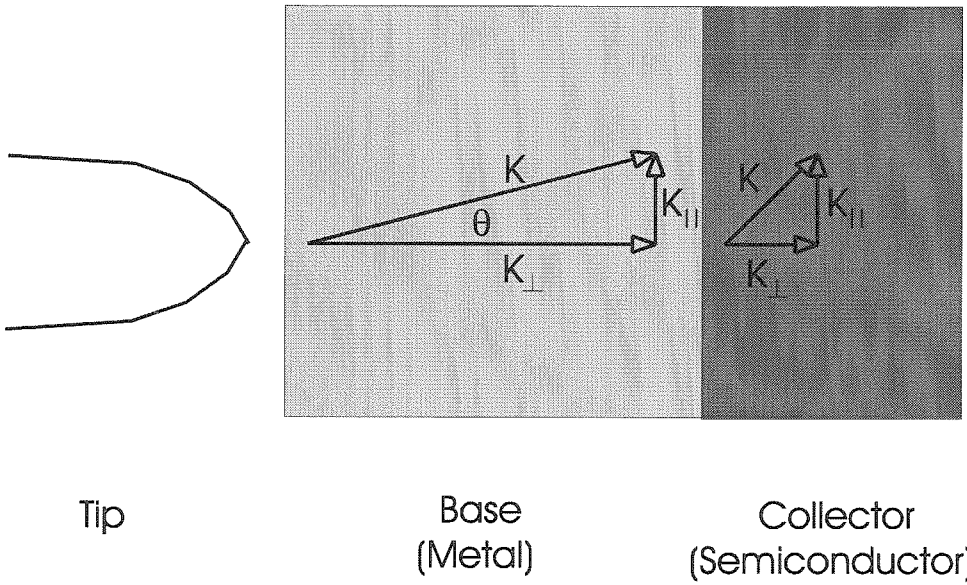

Figure 6.2: Conservation of transverse momentum at base collector interface.

The BEEM collector current at a given bias V can be found by integrating over electrons with energy higher than the band edge of the semiconductor and transverse momentum within the maximum allowed by $k_{\|}$ conservation [2]. If we assume that these "hot" electrons follow the Fermi distribution with the Fermi level at $V + E_F$, and use a step function to approximate for the Fermi function, the expression for the BEEM collector current becomes

$$I_c = C \int_{eV_0+E_F}^{eV+E_F} dE \int_0^{E_{\|}^{max}} dE_{\|} \tag{6.2}$$

where C is a proportionality constant, $E_{\|}$ is the transverse component of the electron energy given by $E_{\|} = \frac{hk_{\|}^2}{2m}$, and $E_{\|}^{max} = \frac{m_s}{m}(E - E_F - eV_0)$ from $k_{\|}$ conservation. This

simplified integral is easily evaluated and indicates that I_c behaves as

$$I_c = \frac{m_s}{m}(V - V_0)^2 \tag{6.3}$$

for voltages just above the turn on threshold V_0.

The parabolic turn on model can be used to extract multiple band edges from BEEM spectroscopy data. The approach has proved to be successful in a number of systems including metal on Si [1, 4, 5], GaAs [2, 6, 7], and GaP [8]. Note that for conduction band minima oriented about an off axis such as the L point in GaAs grown on (100) substrate, or the X point in Si grown on (111) substrate, the acceptance cone is centered at a large angle from the normal. Since the tunneling current is sharply peaked in the forward direction [9] and the acceptance angle is small, no BEEM turn on should result from these band edges unless there is significant scattering in the base layer. In reality, parabolic turn on's due to these off axis band edges can be observed [5], which indicates that the orientations of the hot electrons in the base layer are sufficiently randomized due to inelastic scattering [10]. The magnitude of these turn on's are reduced compared to the on axis conduction minima since fewer hot electrons are scattered into the off axis direction.

6.2.3 Sample Requirements

BEEM is a very powerful characterization technique due to its band structure sensitivity and local probing nature. However, In order to measure the minute BEEM collector signal, the sample must satisfy a number of stringent requirements [11]. This is illustrated in Fig. 6.3 which shows the band diagram and circuit model of a typical BEEM sample.

The first constraint is that the base to collector resistance R_1 must be large, which is often a problem for narrow bandgap semiconductors with small Schottky barrier heights or leaky heterostructures. The large resistance is needed to suppress collector noise current from micro volt fluctuations across the junction. Note that it is the zero bias resistance that matters because no bias is applied across the junction during

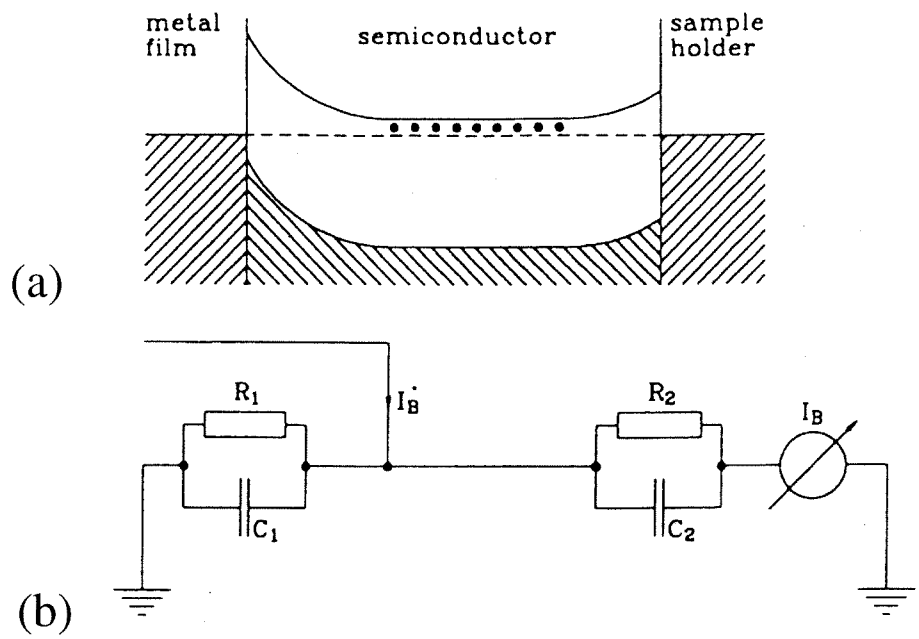

Figure 6.3: Sample requirement for BEEM [11]. (a) Band diagram. (b) Circuit model.

BEEM operation. In practice, BEEM device mesas are made as small as possible to increase R_1.

The second constraint is that the back contact must be a good ohmic contact. As shown in Fig. 6.3, the incoming collector current I_c may flow to ground via the base/collector interface (R_1) or the back contact (R_2). Since only those electrons flowing through the back contact are detected, the BEEM signal will be reduced or not even detectable if R_2 is too large compared to R_1.

These requirement are readily met in $Al_xGa_{1-x}As$ BEEM structures, which are examined in detail in the next chapter to clarify $Al_xGa_{1-x}As$ band structure ambiguities and verify the effectiveness of the BEEM technique. In Chapter 8, we attempt to apply BEEM techniques to antimonide structures which only partially satisfy the constraints outlined above. As will be shown later, this resulted in large noise in the BEEM signal and more limitations on sample configuration.

6.3 BEEM Experiment

6.3.1 Apparatus

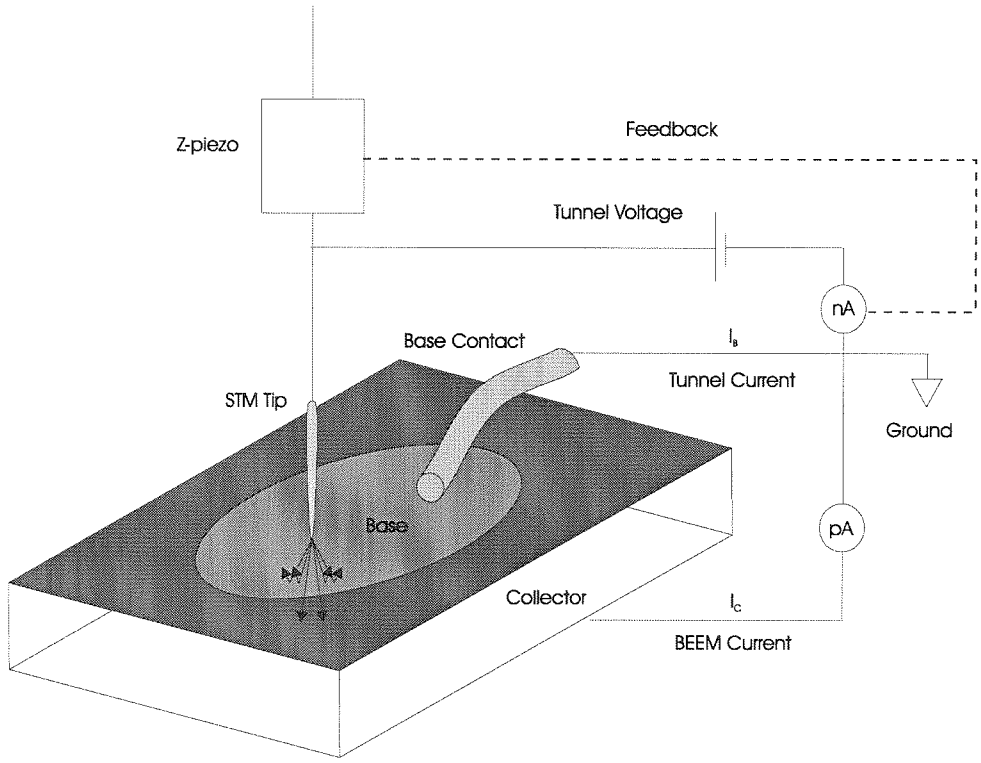

Figure 6.4: Experimental Setup for BEEM.

The samples in this study were examined by using a BEEM apparatus constructed by Rob Miles [12]. As shown in Fig. 6.4, the set-up was based on a Digital Instruments scanning tunneling microscope unit (Nanoscope III) and configured to operate in air at room temperature. The original microscope head was modified to ground the connections differently. The STM pre-amplifier had to be rebuilt so that the sample instead of the tip was grounded. The stock sample mount was also replaced by a custom made unit. In the new configuration, a fine Au wire was spring mounted against the top of the sample as the STM base contact. The sample was proxied to a copper plate via conductive silver paint. Since all BEEM samples were grown by molecular beam epitaxy on indium bonded blocks, the BEEM back contact was furnished by the indium on the back side of the sample left over from growth. During

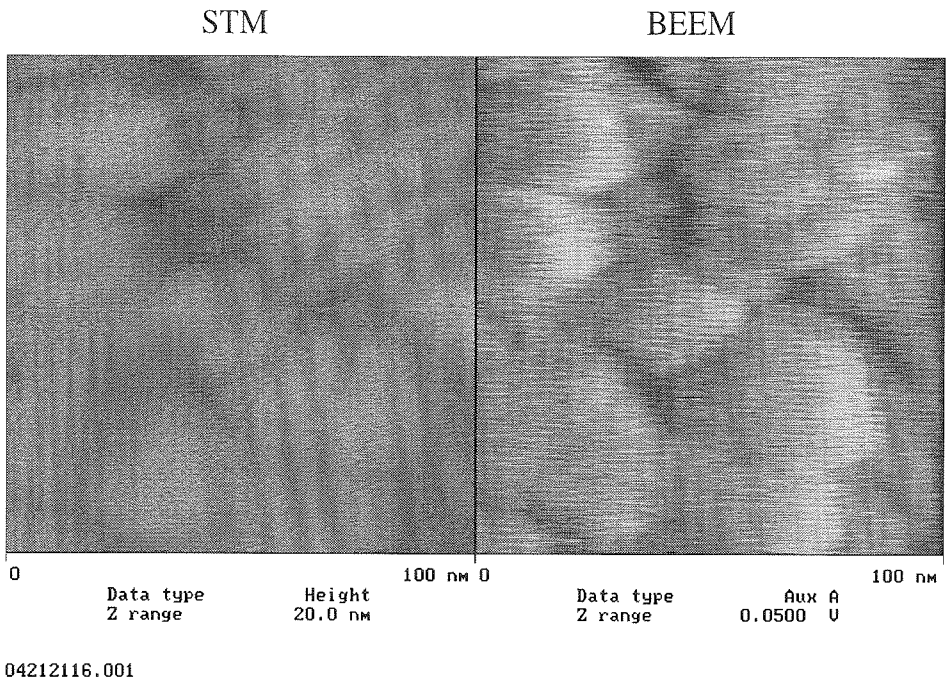

Figure 6.5: Artifact in BEEM image due to high scan speed.

operation, the BEEM collector current was first converted to voltage by a Keithley 427 picoammeter before being fed to the stock digital signal processing unit. Digital Instrument software was used to analyze the data and maintain control of the STM head.

6.3.2 Experimental Issues

When using the setup for BEEM imaging, it was critical to use a very low scan speed. If the scan speed is too high, the STM tip will be momentarily too close to the sample when the sample surface changes abruptly, resulting in a large BEEM signal. This is illustrated in Fig. 6.5, where BEEM image can be seen to echo the grain boundaries in the corresponding STM image. Such close correlation between the surface morphology and the measured signal is a tell tale sign of imaging artifact in scanning probe microscopy. To reduce this effect, it is important to have samples with a relatively smooth surface and lower the scan rate as much as possible.

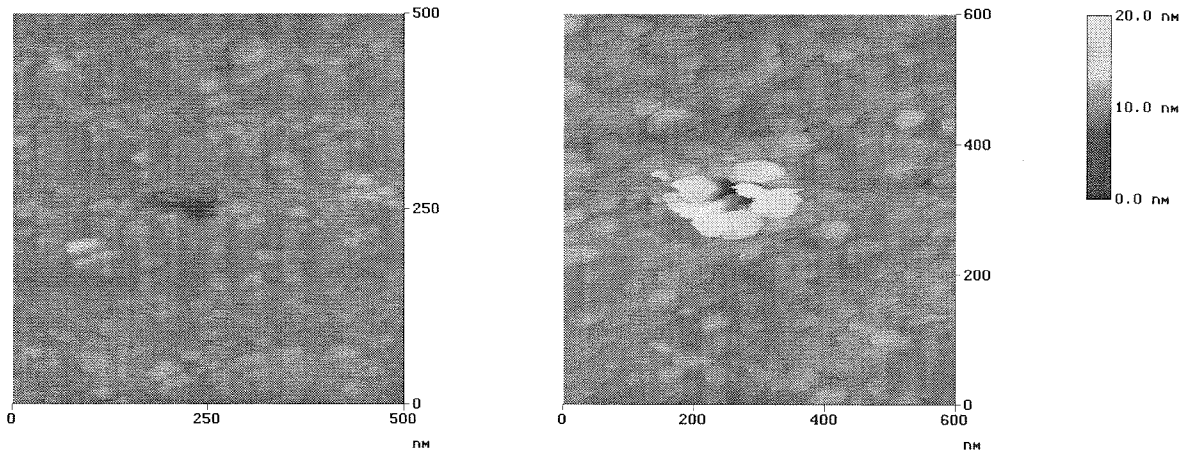

(a) Dent (b) Bump

Figure 6.6: STM images show surface modifications following BEEM spectroscopy at high tip voltages and currents.

During BEEM spectroscopy, the STM tip is parked at one location on the sample surface for an extended period of time. As shown in Fig. 6.6, this sometimes resulted in modification of the surface, which rendered the data unusable. We speculate that this was due to tip heating and increased tip/sample interaction under high current and voltage conditions. To prevent this from happening, it was found that the STM current and voltage must be kept below 10 nA and 2.5 V, respectively.

Since the experiment was carried out in air at room temperature, there was some tip drift even after the system had been given hours to equilibrate. To preserve spatial resolution, it is necessary to use a voltage ramp as fast as possible during BEEM spectroscopy. However, the system response time is limited by the junction capacitance of the BEEM device (see Fig. 6.3) and the integration time of the picoammeter. In practice, the ramp speed was increased as much as possible without inducing any change in the observed BEEM threshold.

Prior to the $Al_xGa_{1-x}As$ experiment, the BEEM spectroscopy set-up was tested and calibrated with the well known Au/Si(100) system, which is one of the first

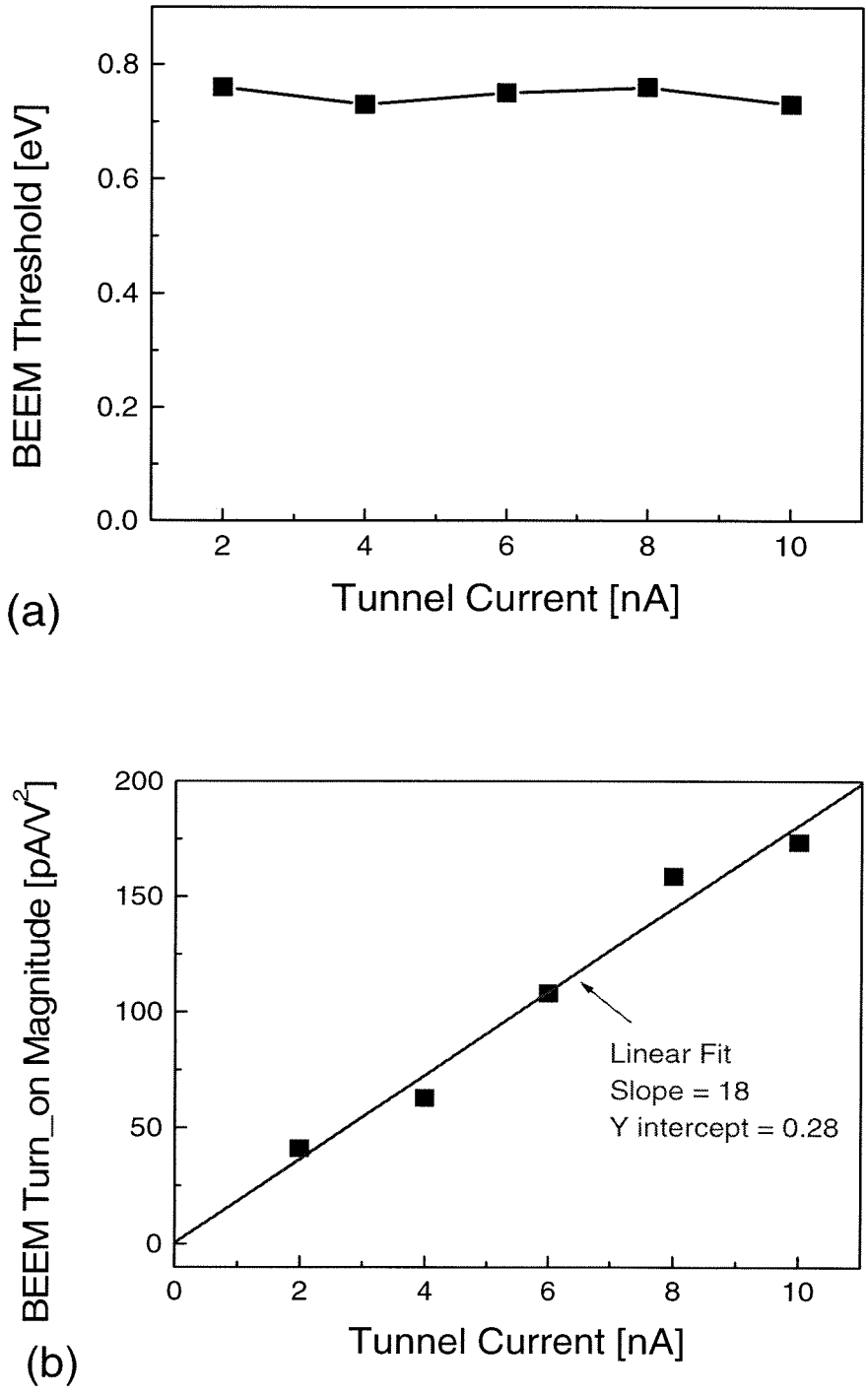

Figure 6.7: Calibration measurements from Au/Si system. (a) Effect of STM tip current on BEEM threshold. (b) Variation in the magnitude of BEEM turn on with STM tip current.

BEEM structures studied. We obtained a value of 0.77 eV for the Au on Si Schottky barrier height, in agreement with the established value [1, 4]. As shown in Fig. 6.7, the BEEM threshold was independent of the STM tip current, and the magnitude of the collector turn on was proportional to the tip current, indicating that the results were free of artifacts and the system had worked as expected.

Bibliography

[1] W. J. Kaiser and L. D. Bell, *Phys. Rev. Lett.* **10**, 1406 (1988).

[2] L. D. Bell and W. J. Kaiser, *Phys. Rev. Lett.* **61**, 2368 (1988).

[3] M. H. Hecht, L. D. Bell, W. J. Kaiser, and F. J. Grunthaner, Appl. Phys. Lett. **55**, 780 (1989).

[4] E. Y. Lee and L. J. Schowalter, *Phys. Rev. B* **45**, 6345 (1992).

[5] M. T. Cuberes, A. Bauer, H. J. Wen, D. Vandre, M. Pretsch and G. Kaindl, *J. Vac. Sci. Technol. B* **12**, 2422 (1994).

[6] A. E. Fowell, R. H. Williams, B. E. Richardson, A. Cafolla, D. I. Westwood and D. A. Woolf, *J. Vac. Sci. Technol. B* **9**, 581 (1991).

[7] T. -H. Shen, M. Elliott, A. E. Fowell, A. Cafolla, B. E. Richardson, D. Westwood, and R. H. Williams, *J. Vac. Sci. Technol. B* **9**, 2219 (1991).

[8] M. Prietsch and R. Ludeke, *Phys. Rev. Lett.* **66**, 2511 (1991).

[9] J. G. Simmons, *J. Appl. Phys.* **34**, 1793 (1963).

[10] L. J. Schowalter and E. Y. Lee, *Phys. Rev. B* **43**, 9308 (1991).

[11] M. Prietsch, *Physics Reports* **253** 163 (1995).

[12] R. J. Miles, Thesis, California Institute of Technology, 1995.

Chapter 7 BEEM Study of $Al_xGa_{1-x}As$

7.1 Introduction to Chapter

In this chapter, the capabilities of the BEEM technique are demonstrated through the case study of $Al_xGa_{1-x}As$ heterostructures. In particular, the study focuses on extraction of local $Al_xGa_{1-x}As$ Schottky barrier heights and band edges from BEEM spectroscopy measurement. The results are compared with existing data from other measurement techniques, which serves to clarify uncertainties in previous findings. In addition, BEEM imaging of the buried interface is demonstrated.

7.2 Motivation

Because of the technological importance of $Al_xGa_{1-x}As$, its various properties have been extensively studied. In particular, parameters of the $Al_xGa_{1-x}As$ band structure have been determined from a variety of measurements, including photo response [1], optical transmission and photo luminescence [2], variation of Hall electron concentration with temperature [3], and variation of electrical conductivity with temperature [4]. However, there is some uncertainty about the exact positions of Γ, L, and X band edges, especially at high Al concentrations where the bandgap of the material becomes indirect. Figure 7.1(a) shows the measured band edge shift with Al concentration from these studies. The band structure of GaAs is also shown in Fig. 7.1(b) for reference. It can be seen that band edge positions obtained from different measurement techniques can differ by as much as 150 meV. In addition, there is a lack of consensus about the $Au/Al_xGa_{1-x}As$ Schottky barrier height at different Al concentrations [5, 6], which can be partly attributed to the various sample preparation procedures available.

These issues are ideally addressed by BEEM, which not only provides imaging of

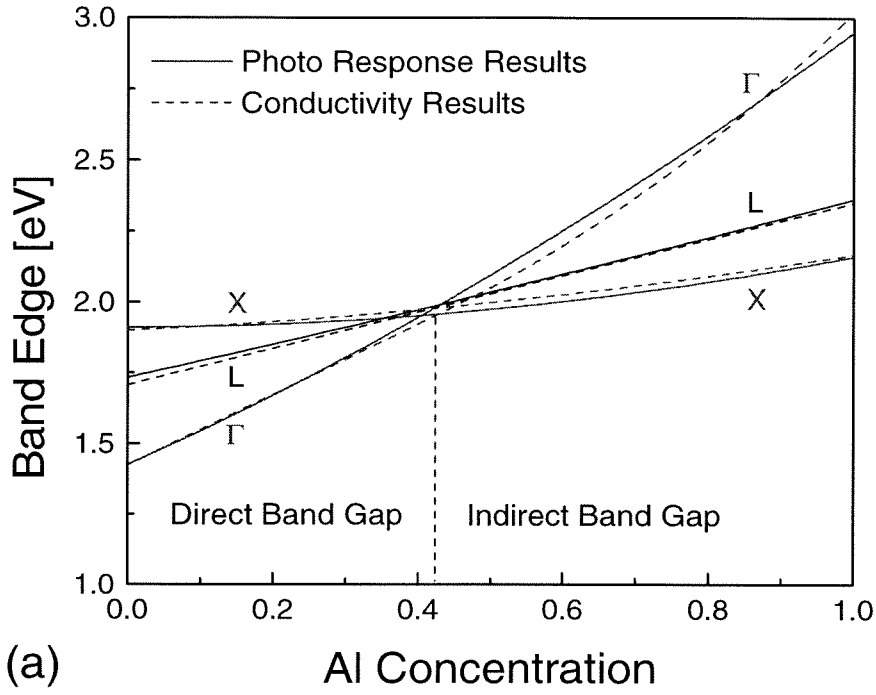

(a)

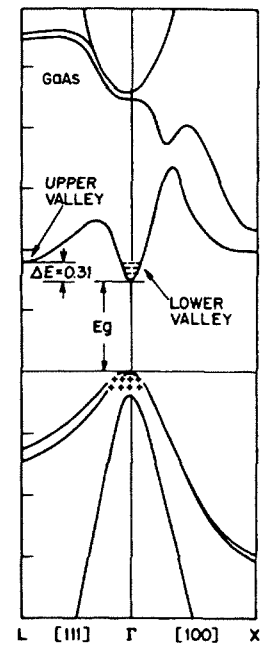

(b)

Figure 7.1: (a) Measured shift in $Al_xGa_{1-x}As$ band edges with Al concentration. (b) Band structure of GaAs.

the buried interface, but also allow extraction of the local Schottky barrier height and band edge positions from spectroscopy data. By varying the Al concentration in the $Al_xGa_{1-x}As$ BEEM sample, the Schottky barrier height and higher lying band edges of the material can be mapped out in both the direct and indirect bandgap regime. Of particular interest are the higher lying conduction band edges in $Al_xGa_{1-x}As$. Unlike the metal on semiconductor Schottky barrier height, the position of the higher lying band edge relative to the bottom of the conduction band is an inherent property of the material. It should not depend on interface chemistry and should also exhibit less local variation. Such information as measured by BEEM can be directly compared with results obtained from other techniques. Hence the $Al_xGa_{1-x}As$ BEEM study should clarify previous uncertainties about the various band edge positions and serve to verify the validity of the BEEM technique.

7.3 Sample Description and Preparation

The $Al_xGa_{1-x}As$ BEEM samples were grown by molecular beam epitaxy and metallized *ex situ* with a sputter deposition tool. Figure 7.2 shows the structure and band diagram of a typical sample. Highly doped (n=1 $\times$ $10^{18}/cm^3$) epi-ready GaAs (100) wafers were used as substrates to ensure that the back contact is conductive enough to support BEEM current. Following oxide desorption, a buffer layer was grown to grade the doping profile down to the level of the unintentionally doped $Al_xGa_{1-x}As$ epilayer. The doping in the buffer layer started out at n=1 $\times$ $10^{18}/cm^3$ for the first 0.2 μm and was gradually tapered down to n=2 $\times$ $10^{16}/cm^3$ over the next 0.1 μm. At the end of buffer growth, samples were soaked in As for 30 seconds, yielding the (2 $\times$ 4) reflection high energy electron diffraction (RHEED) pattern characteristic of reconstructed GaAs surface. An unintentionally doped $Al_xGa_{1-x}As$ layer was grown on top of the smoothed GaAs surface. The epilayers were kept thin to support transport of BEEM current, and the doping level was kept low in the epilayer and the buffer layer immediately below it to reduce effect of band bending.

Table 7.1 lists the exact configuration of the epilayer for various Al concentrations.

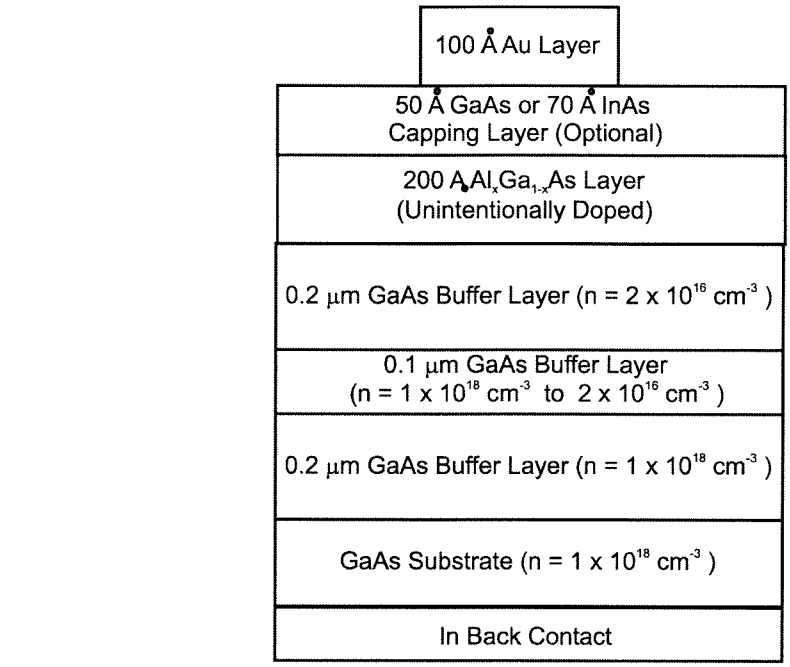

(a)

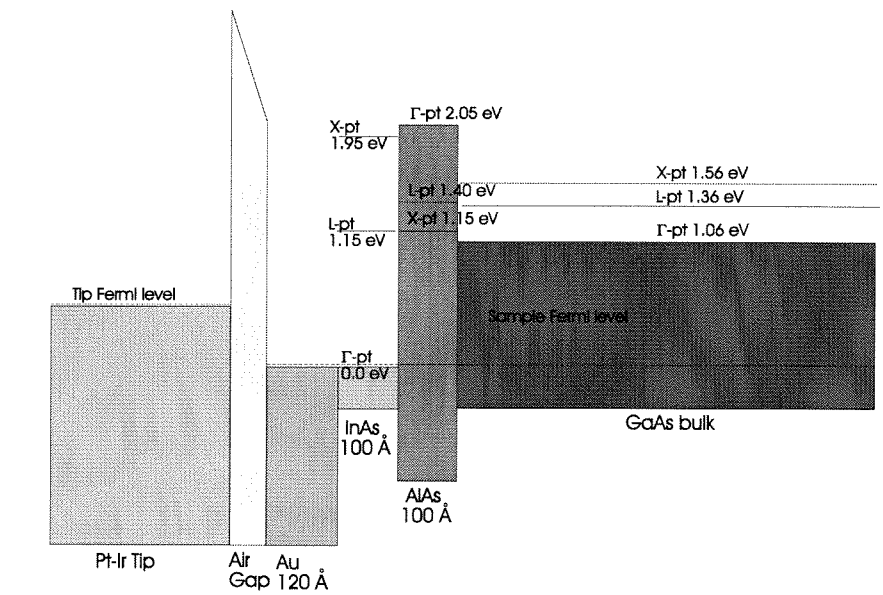

(b)

Figure 7.2: (a) Structure of $Al_xGa_{1-x}As$ BEEM sample. (b) Band diagram of BEEM sample with AlAs epilayer.

The $Al_xGa_{1-x}As$ layer was 200 Å thick for samples with low Al content ($x < 0.5$) and 100 Å thick for samples with high Al content. At $x = 0.25$, samples with epilayers of both thicknesses were grown to examine its effect on BEEM turn on threshold. At the end of the growth, samples with high Al content were capped off by either a 50 Å GaAs layer or a 70 Å InAs layer to prevent oxidation of the $Al_xGa_{1-x}As$ layer.

Table 7.1: List of $Al_xGa_{1-x}As$ BEEM structures studied.

Epilayer Composition	Epilayer Thickness [Å]	Cap Layer
GaAs		none
$Al_{0.11}Ga_{0.89}As$	200	none
$Al_{0.19}Ga_{0.81}As$	200	none
$Al_{0.25}Ga_{0.75}As$	100	none
$Al_{0.25}Ga_{0.75}As$	200	none
$Al_{0.25}Ga_{0.75}As$	500	none
$Al_{0.50}Ga_{0.50}As$	100	none
$Al_{0.50}Ga_{0.50}As$	100	GaAs
$Al_{0.50}Ga_{0.50}As$	500	none
$Al_{0.50}Ga_{0.50}As$	500	InAs
$Al_{0.80}Ga_{0.20}As$	100	GaAs
AlAs	100	GaAs
AlAs	100	InAs

A sputter-etch deposition system was used for post growth metallization. Gold was sputtered off a solid target by Ar plasma and deposited onto the sample at a rate of 0.7 Å/sec. Samples were placed behind a mask and patterned with arrays of Au dots 1 mm in diameter. As discussed in Section 6.2.3, the BEEM device should be as small as possible to reduce the background noise current. It was found that an area of 1 mm^2 was the practical limit due to sample placement and tip engagement restrictions. The Au layer thickness was monitored by a crystal oscillator and maintained at 100 Å for all samples. Atomic force microscopy (AFM) studies showed that the typical metal layer had a rms roughness on the order of 5 Å. For most samples, the surface morphology was smooth and appeared suitable for BEEM studies. The sputter deposition rate was varied for early samples and was found

to have little effect on BEEM results, indicating that sputter damage at the base collector layer interface was not a significant factor.

Prior to metallization, samples were taken out of the UHV growth environment and exposed to the ambient. Hence a 20 - 30 Å thick native oxide was present between the metal and semiconductor layer. However, it has been shown that the oxide layer does not affect BEEM results for Au/GaAs structures [7]. In fact, samples with native oxide layers support BEEM current more consistently over a longer period of time [7]. In our study, it was found that samples with native oxide layers were stable for up to several months. To minimize contamination from handling, a degreasing procedure was followed before the sample was introduced to the metallization chamber. It consisted of sequential ultra sonic rinse in trichloromethane, acetone, isopropanol and de-ionized water, with each rinse lasting 2 minutes. The procedure helped generate more consistent BEEM results, especially for samples that have been stored in air for a long time.

7.4 BEEM Imaging Results

The samples were examined by using the BEEM set-up described in the previous chapter (Section 6.3.1). Figure 7.3 shows BEEM images of the $Al_{0.11}Ga_{0.89}As$ sample on two different scales. In both cases, the tip bias was at 1.2 V, which was above the BEEM turn on threshold. It can be seen that the BEEM images bear little resemblance to the corresponding STM topography, which was clear evidence that the BEEM images were decoupled from their STM counterparts and were free of scan parameter induced artifacts. Figure 7.3(a) was typical in that the BEEM image of the buried surface appeared to be smooth and relatively featureless, which was a reflection of the high growth quality of the sample and the uniformity of the buried interface. In Fig. 7.3(b), the BEEM current over a large patch of area appeared to be suppressed even though the surface topography was relatively uniform, which clearly illustrates the effectiveness of using BEEM to image the buried interface.

Figure 7.4 shows a series of BEEM scans over the same area at different tip bias.

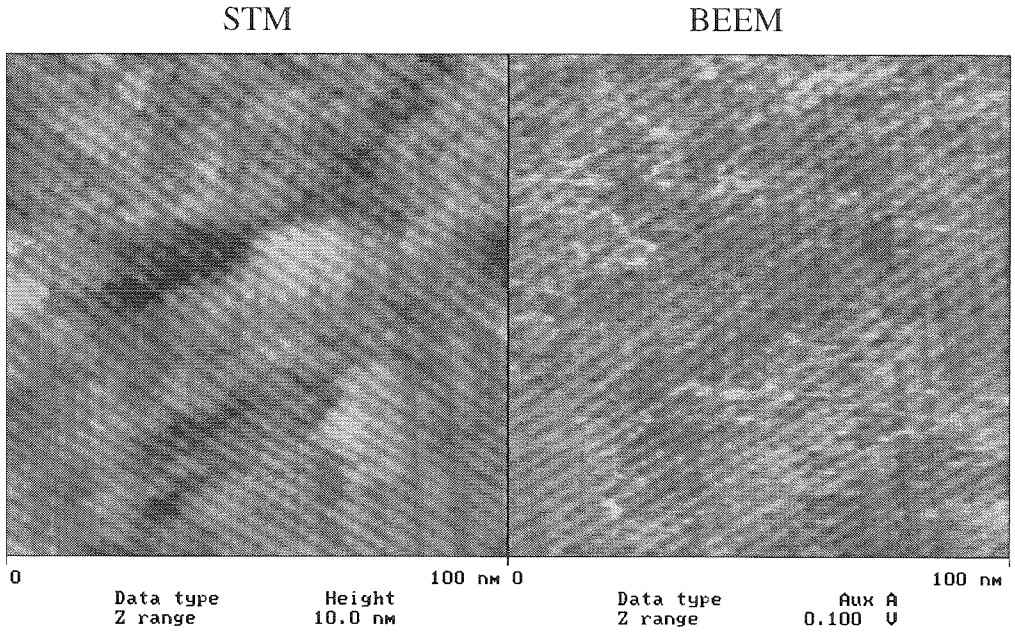

(a) 100 nm Area Scan

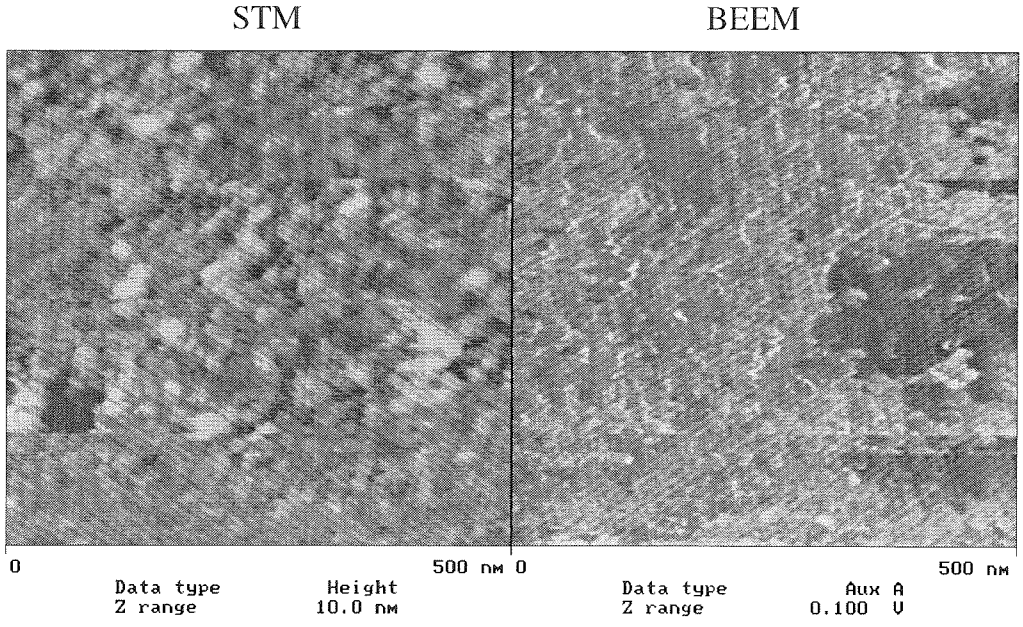

(b) 500 nm Area Scan

Figure 7.3: BEEM images of buried $Al_{0.11}Ga_{0.89}As$ interface. (a) 100 nm by 100 nm scan. (b) 500 nm by 500 nm scan.

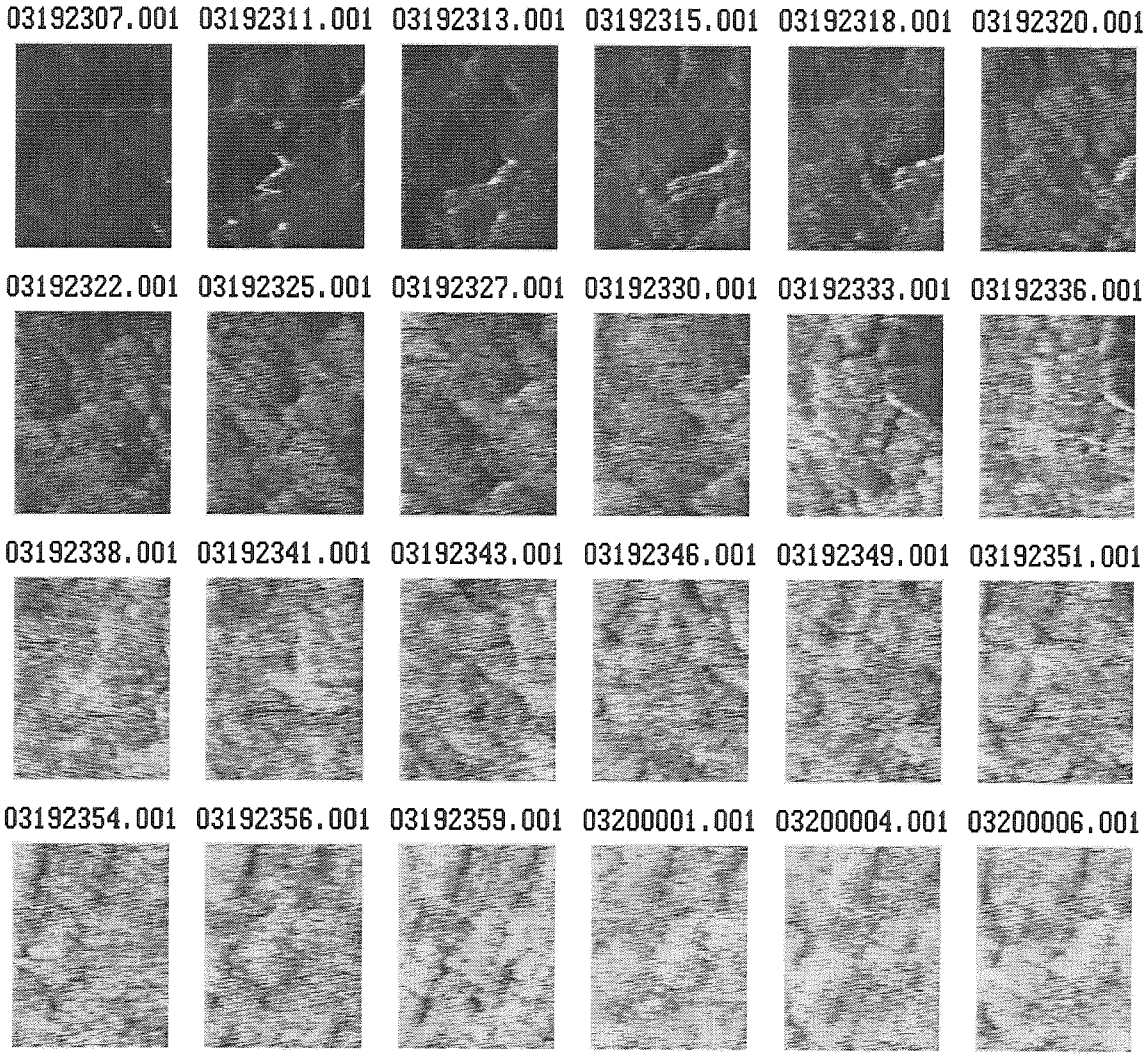

Figure 7.4: BEEM images at different tip bias. The tip bias varied from 0.8 V in the first picture to 2.2 V in the last picture. Scan area was 100 nm by 100 nm.

The tunneling current was held constant at 5 nA. As the tip bias was gradually increased to beyond the BEEM turn on threshold, the BEEM signal picked up and the image became brighter. In essence, this was similar to BEEM spectroscopy measurement except that an entire area instead of a single spot was examined. Due to tip drift, the images are slightly shifted from frame to frame. In the series of images shown, features can be seen to move to the right. If the data from different frames can be linked to each other through feature tracking software, then the BEEM I-V characteristics of a large number of positions can be simultaneously analyzed. This is potentially a very powerful technique as it will result in a mapping of BEEM threshold (Schottky barrier height) over a large area.

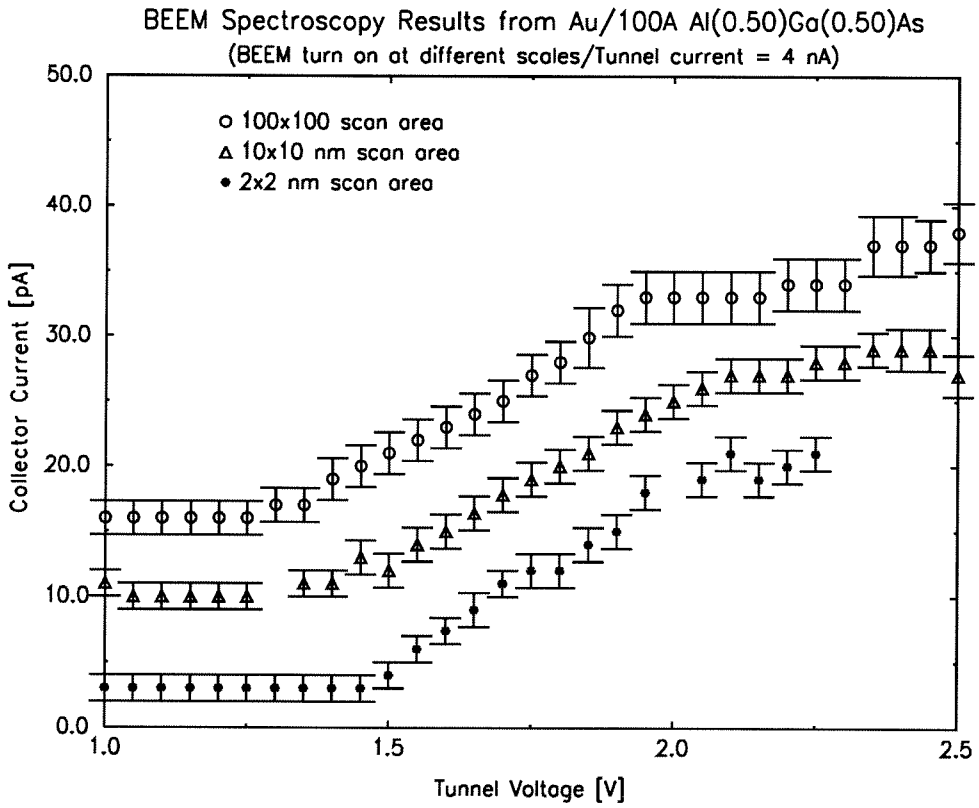

Figure 7.5: Average signal from BEEM images at different tip bias.

Such sophisticated analysis was not developed due to the limited scope of this study. A shot gun alternative was to plot the average BEEM current over the whole image as the tip bias was increased. Figure 7.5 shows three such plots from scans of

different sizes. The error bars in the plot represented the spread in BEEM signal over the whole image area. It can be seen that the results from the 10 nm and 100 nm scan area were similar to each other, whereas the 2 nm scan area yielded a significantly higher BEEM threshold. The greater variation in BEEM threshold for small scan areas may be genuine, but it may also be due to more severe tip drift in the smaller area scan. Regardless the origin of this difference, we can draw the conclusion that the local BEEM threshold (Schottky barrier height) appeared to be uniform for these samples over scales greater than 10 nm.

7.5 BEEM Spectroscopy Results

While direct BEEM imaging can reveal non uniformities in the buried interface, the local band structure of the sample is more accurately determined by using BEEM spectroscopy. In this process, the STM tip is held at a fixed position on the sample surface and the collector current is monitored as a funtion of tip voltage.

7.5.1 BEEM Turn on Threshold

Figure 7.6 shows a typical BEEM spectroscopy I-V curve from a sample. The data were averaged over 50 voltage ramps to improve the signal to noise ratio. Typically, the tip drifted 5 to 10 nm during the 10 minutes it took to complete the 50 ramps. Thus the spatial resolution of BEEM spectroscopy was drift limited and about an order of magnitude higher than the theoretical limit [14]. The resulting BEEM I-V curve should be considered an average over the same area.

The parabolic turn on model was applied to analyze the BEEM I-V curve due to its simplicity [14]. Hence the BEEM I-V curve was assumed to take on the form

$$I_c = \sum_{i=1}^{n} (V - V_i)^2 \tag{7.1}$$

Where I_c is the BEEM collector current, V is the tunnel voltage and V_i is the threshold voltage. Note that each term in the sum only came in when the tunnel voltage

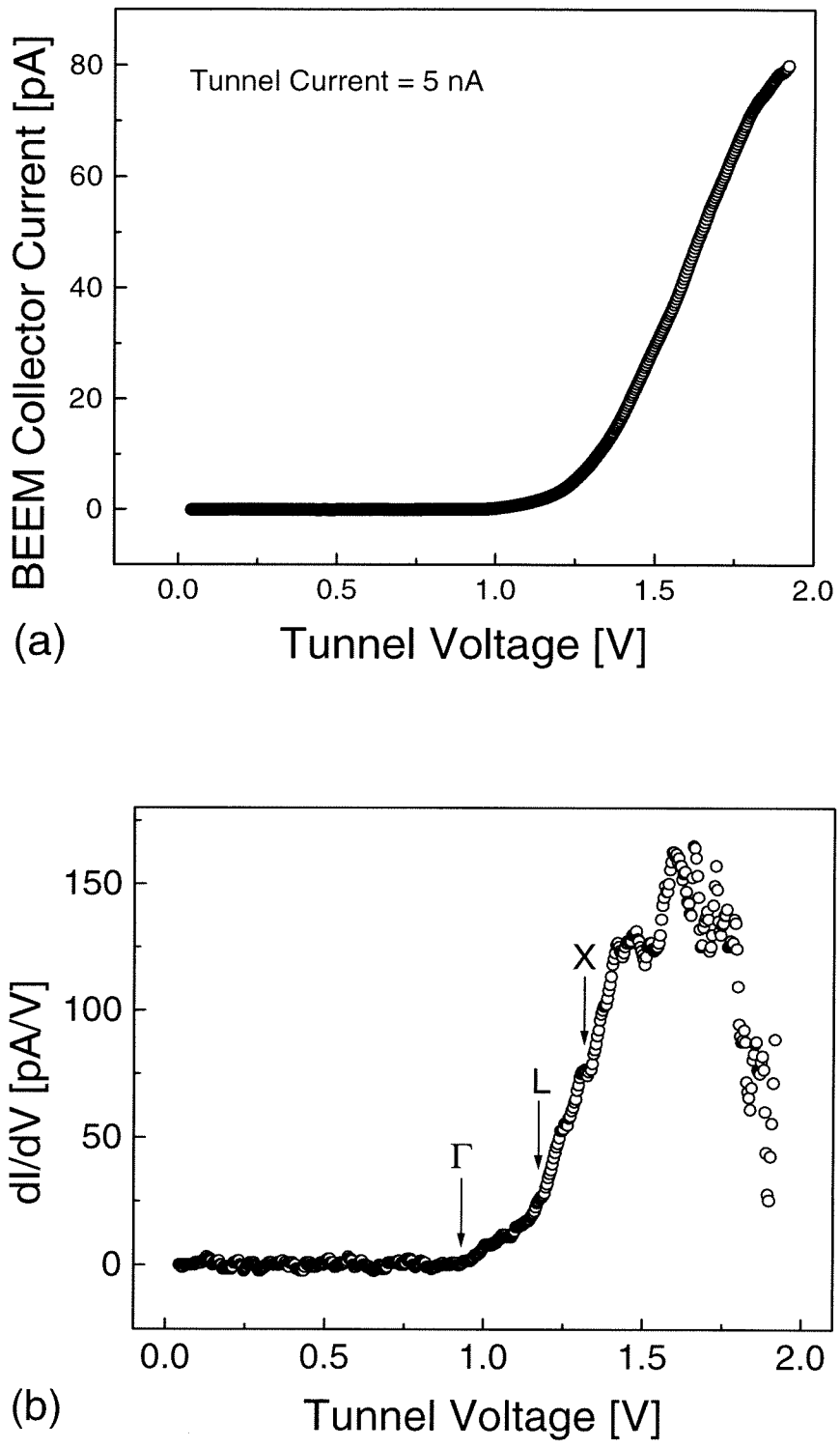

Figure 7.6: (a) BEEM spectroscopy curve from an $Al_{0.11}Ga_{0.89}As$ sample. (b) Extraction of BEEM threshold from differentiated curve.

was above the corresponding threshold. As shown in Fig. 7.6(b), differentiating the BEEM I-V curve generated a piece wise linear curve that clearly revealed the multi-threshold nature of the turn on. The I-V curve shown in Fig. 7.6 was obtained from an $Al_{0.11}Ga_{0.89}As$ sample. Three thresholds were extracted. According to Fig. 7.1, they corresponded to the Γ, L and X points in the $Al_{0.11}Ga_{0.89}As$ layer. Other samples with low Al concentrations ($x = 0, 0.11, 0.19, 0.25$) produced similar BEEM I-V curves. However, the third threshold, attributed to the X point, was not always evident in every run. This may be due to the comparatively large effective mass of the X valley [8], which tended to weaken the corresponding BEEM turn on (see equation 6.3). Samples with high Al concentrations ($x = 0.50, 0.80, 1$) also produced BEEM I-V curves that had robust two threshold fits. The thresholds, however, were attributed to the X and L points. For all samples, it was found that the parabolic turn on model broke down at about 0.5 V above the first threshold, which was expected due to increased scattering of energetic carriers in the metal layer [9].

7.5.2 Effect of Epilayer Thickness and Capping Layer

The $Al_xGa_{1-x}As$ layer thickness was varied for $x = 0.25$. As shown in Fig. 7.7, epilayer thickness variation beyond 100 Å did not significantly affect the measured BEEM thresholds. Thus the measured band edges may be considered bulk properties of $Al_xGa_{1-x}As$. This result agreed with findings from the Au/AlAs study by Kaiser et al., who showed that most of the thickness induced threshold shift occured over the first few monolayers of the semiconductor [10].

The effect of a capping layer is shown in Fig. 7.8. It can be seen that for both Al concentrations, the capping layer had only a slight effect on the BEEM thresholds. One may expect that a InAs capping layer will lower the apparent Schottky barrier height due to the negative Schottky barrier of InAs and band bending at the $InAs/Al_xGa_{1-x}As$ interface. The absence of this effect in our sample is attributed to relaxation at the $InAs/Al_xGa_{1-x}As$ interface. Due to the large lattice mismatch between InAs and $Al_xGa_{1-x}As$ (8 %), the critical layer thickness for InAs on $Al_xGa_{1-x}As$

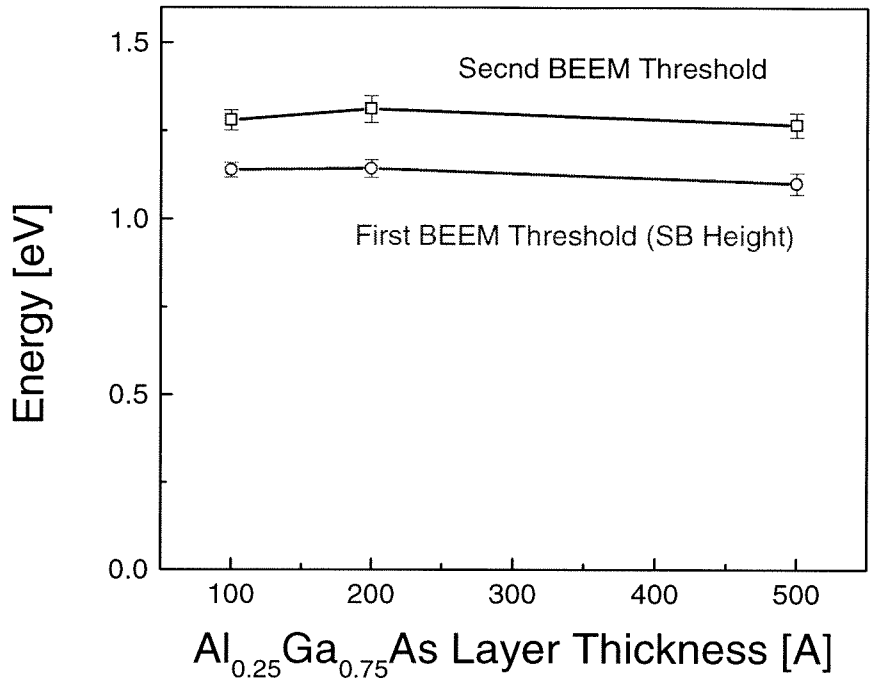

Figure 7.7: Variation of BEEM threshold with $Al_xGa_{1-x}As$ layer thickness.

is only a few monolayers. Hence the 100 Å thick InAs capping layer must have fully relaxed to its natural lattice template, resulting in a large number of dislocations and dangling bonds at the capping layer/$Al_xGa_{1-x}As$ interface, pinning the Fermi level to the middle of the indirect bandgap. It should be noted that the capping layer did help to prevent deterioration of the $Al_xGa_{1-x}As$ layer. The uncapped sample in Fig. 7.8 supported BEEM current for only a few days whereas the capped samples were stable for up to several months.

7.5.3 Variation of Band Edge and Schottky Barrier Height with Al Concentration

The BEEM turn on thresholds were interpreted as band edges in the semiconductor. The variation of these band edges with Al concentration x is shown in Fig. 7.9. The extent to which the parabolic model remained valid is also plotted in the same figure. Each data point represents 20 to 30 runs. Since results for $Al_{0.50}Ga_{0.50}As$ indicate that the capping layer did not significantly affect BEEM thresholds, we may

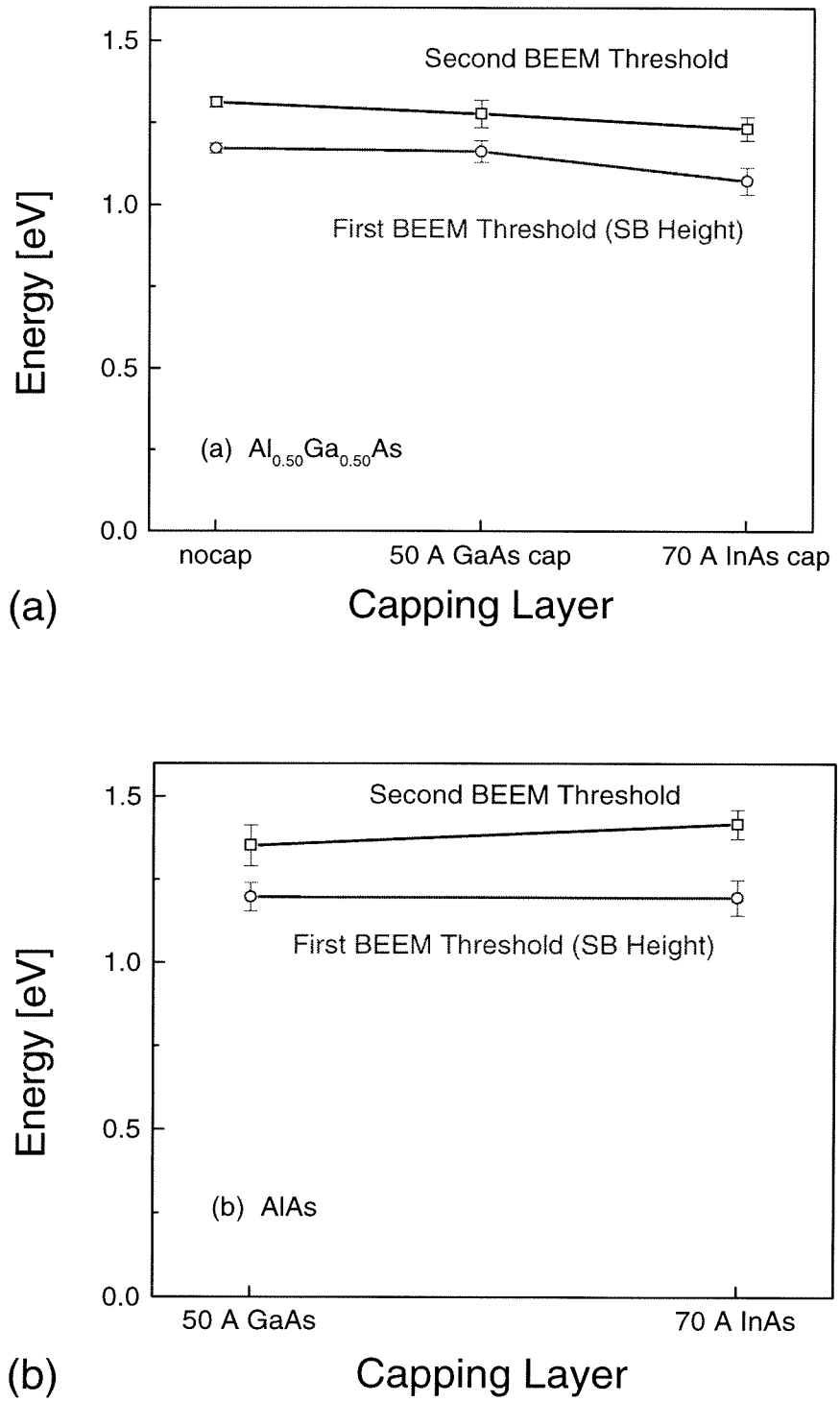

Figure 7.8: Effect of capping layer on BEEM threshold. (a) $Al_{0.50}Ga_{0.50}As$ sample. (b) AlAs sample.

view the energy position curves as continua. It can be seen that the Au Schottky barrier height increased with Al concentration x until the semiconductor changed from direct bandgap to indirect bandgap ($x > 0.45$). At higher Al concentrations, the Au Schottky barrier height stayed almost constant. The measured Schottky barrier height were consistent with the data reported in the literature [11, 10].

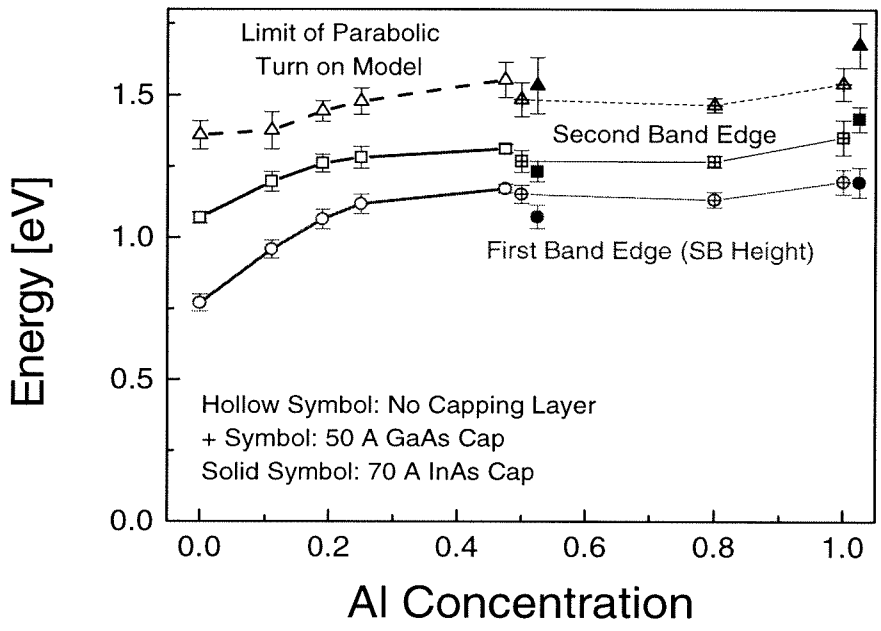

Figure 7.9: Variation of $Al_xGa_{1-x}As$ band edges with Al composition x. Multiple data points at $x = 0.50$ and $x = 1.0$ are slightly offset for clarity.

To more easily compare the Schottky barrier result with previous findings, it is helpful to plot the implied p-type Schottky barrier height, which is obtained by subtracting the n-type Schottky barrier height from the semiconductor bandgap. Plotted on the same graph as the bandgap, it reveals the position of the surface Fermi level relative to the valence band edge [12]. As shown in Fig. 7.10, the surface Fermi level stayed nearly constant at about 0.6 eV from the top of the valence band for $x < 0.4$. This agreed with the common anion rule [13] which states that the position of the Fermi level relative to the valence band edge in III-V and II-VI compound should only depend on the anion involved. As the material changes from direct bandgap to indirect bandgap at higher Al concentrations, the surface Fermi level moved towards

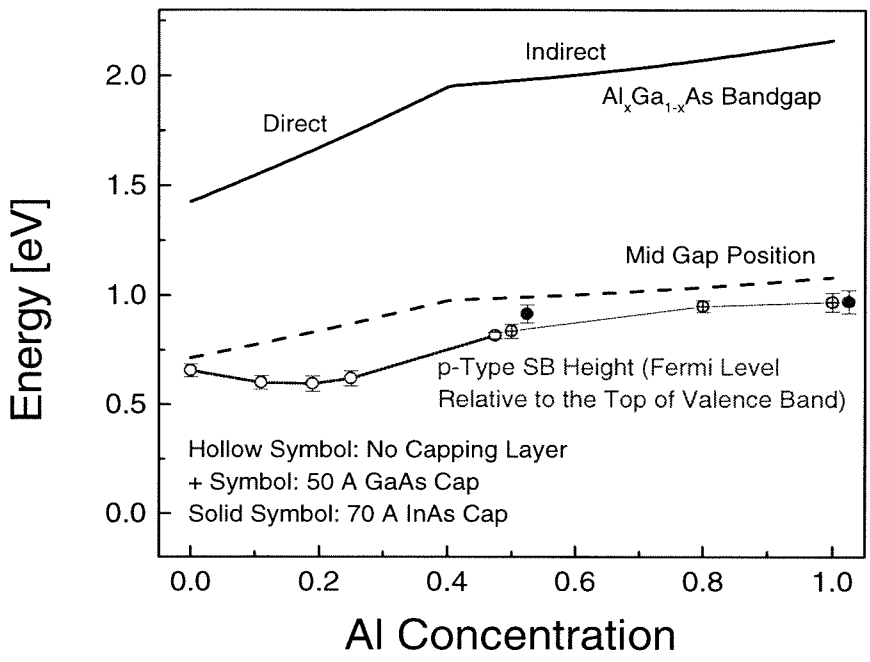

Figure 7.10: P-type Schottky barrier height inferred from BEEM data. Multiple data points at $x = 0.50$ and $x = 1.0$ are slightly offset for clarity.

and stayed close to the middle of the indirect bandgap. This may be due to Fermi level pinning from surface states created by the additional capping layer in these samples.

7.5.4 Mapping of the Relative Position of Band Edges in $Al_xGa_{1-x}As$

In general, Schottky barrier height depends on surface treatment and other details of sample preparation. For example, BEEM workers have obtained Au on GaAs Schottky barrier heights that range from 0.82 eV to 0.90 eV [14, 15]. The position of the higher lying band edge relative to the first band edge, however, is an intrinsic property of the semiconductor and should be independent of processing. Figure 7.11 shows the variation of this band edge difference with Al composition x. The plot is derived from the BEEM threshold data in Fig. 7.9 by subtracting the first threshold from the second threshold. The subtraction and error analysis was done for each

individual run. Note that the error bars in Fig. 7.11 are smaller than the sum of threshold error bars in Fig. 7.9, which shows that the band edge difference was an intrinsic property of the material and had less variation form sample to sample.

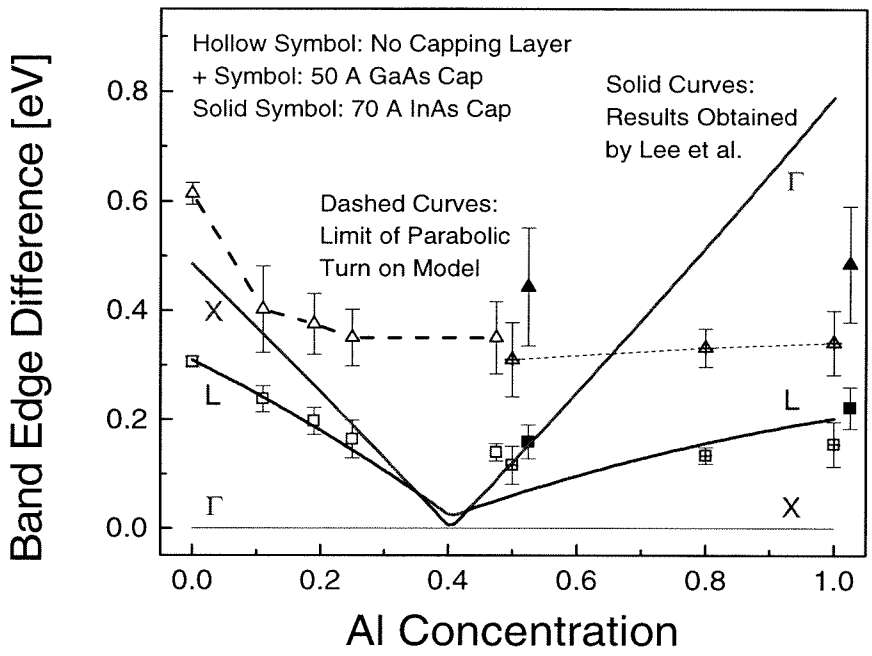

Figure 7.11: Relative positions of the higher lying band edges as measured by BEEM. Multiple data points at $x = 0.50$ and $x = 1.0$ are slightly offset for clarity.

These relative energy positions were compared with $Al_xGa_{1-x}As$ band structure data obtained from other techniques [1, 2, 3, 4]. It was found that the BEEM results agreed best with the conductivity findings by Lee et al., which are plotted in Fig. 7.11 for reference. For $x < 0.45$, where $Al_xGa_{1-x}As$ is a direct bandgap material, it can be seen that the BEEM threshold difference tracked well with the difference between the L and Γ points as obtained by Lee et al. For $x > 0.45$, where $Al_xGa_{1-x}As$ is an indirect bandgap material, there was more scatter in the data but BEEM threshold difference agreed well with the difference between the L and X points. Since the L point lies at an off angle from the (100) normal growth direction, its presence in BEEM threshold analysis indicates that there was significant scattering before the electrons reached the metal semiconductor interface [16]. The range over which the parabolic model remained valid is also plotted on the same figure. It can be seen that

the Γ point was out of range at high Al concentrations but the X point should have been observed as the third BEEM threshold at low Al concentrations. In fact, the X point turn on was present in some runs. However, it was a weak turn on due to the large effective mass of the X valley, and the results were not consistent enough for systematic analysis.

The spatial variation of the band edges are represented by error bars on the data points. Each error bar was the result of 20 to 30 local measurements. The size of the error bar ranged from 30 to 50 meV and was consistent with the level of uniformity observed in corresponding BEEM images (Section 7.4). Tip drift limited our spectroscopy resolution to about 5 to 10 nm, which was an order of magnitude higher than the theoretical limit [14]. This may have resulted in less measured variation since BEEM spectroscopy was averaged over the larger area.

7.6 Summary and Conclusion

BEEM techniques have been successfully applied to the Au/$Al_xGa_{1-x}As$ system. BEEM images were readily obtained and its capability for revealing sub-surface non-uniformities demonstrated. In addition, BEEM spectroscopy was used to map out the Schottky barrier height and the higher lying band edges in $Al_xGa_{1-x}As$ as the Al concentration x was varied. It was found that the indirect band edge (L point) contributed significantly towards the BEEM signal, which indicates that scattering was significant in the base region of the sample. Moreover, the relative positions of the higher lying band edges in $Al_xGa_{1-x}As$ were extracted from the BEEM spectroscopy data. Since these relative energy positions are intrinsic to the material and independent of sample preparation detail, the measurements represented direct probing of the semiconductor band structure. Comparison with the existing data showed good agreement between the BEEM measured values and the conductivity findings by Lee et al. [4]. The study clarifies previous uncertainties about the $Al_xGa_{1-x}As$ energy positions and demonstrates that BEEM is a effective tool for probing semiconductor band structure.

Bibliography

[1] H. C. Casey and M. B. Panish, *J. Appl. Phys.* **40**, 4910 (1969).

[2] B. Monemar, K. K. Shih, and G. D. Pettit, *J. Appl. Phys.* **47**, 2604 (1976).

[3] A. K. Saxena, *Phys. Stat. Solid. (B)* **105**, 777 (1981).

[4] H. J. Lee, L. Y. Juravel, J. C. Woolley, and A. J. SpringThorpe, *Phys. Rev. B* **21**, 659 (1980).

[5] J. S. Best, *Appl. Phys. Lett.* **34**, 522 (1979).

[6] Yu. A. Gol'dberg, T. Yu. Rafiev, B. V. Tsarenkov, and Yu, P. Yakovlev, *Sov. Phys. Semicond.* **6**, 398 (1972).

[7] A. A. Talin, D. A. Ohlberg, R. S. Williams, P. Sullivan, I. Koutselas, B. Williams, and K. L. Kavanagh, *Appl. Phys. Lett.* **62**, 2965 (1993).

[8] *Semiconductors: Group IV elements and III-V Compounds*, edited by O. Madelung, Spriner-Verlag, Berlin, 1991

[9] C. R. Crowell and S. M. Sze, *Physics of Thin Films, eds. G. Hass and R. F. Thun*, Academic Press, New York, 1967.

[10] W. J. Kaiser, M. H. Hecht, L. D. Bell, F. J. Grunthaner, J. K. Liu, and L. C. Davis, *Phys. Rev. B* **48**, 18 324 (1993).

[11] J. J. O'Shea, T. Sajoto, S. Bhargava, D. Leonard, M. A. Chin, and V. Narayanamurti, J. Vac. Sci. Technol. B **12**, 2625 (1994).

[12] E. H. Rhoderick and R. H. Williams, *Metal-Semiconductor Contacts*, Clarendon Press, Oxford, 1988.

[13] J. O. McCaldin, T. C. McGill, and C. A. Mead, *J. Vac. Sci. Technol.* **13**, 802 (1976).

[14] L. D. Bell and W. J. Kaiser, *Phys. Rev. Lett.* **61**, 2368 (1988).

[15] A. E. Fowell, R. H. Williams, B. E. Richardson, A. Cafolla, D. I. Westwood and D. A. Woolf, *J. Vac. Sci. Technol. B* **9**, 581 (1991).

[16] L. J. Schowalter and E. Y. Lee, *Phys. Rev. B* **43**, 9308 (1991).

Chapter 8 BEEM Study of AlSb and InAs/AlSb Superlattice

8.1 Introduction to Chapter

This chapter describes the application of BEEM technique to the InAs/GaSb/AlSb system. Two device relevant structures are studied: AlSb barrier and selectively dope InAs/AlSb superlattice. Due to the large background noise in these structures, BEEM images are not obtained. Instead, the study focuses on extraction of band structure and transport characteristics from BEEM spectroscopy measurement. In the AlSb case study, the impact of sample structure on BEEM background current is also addressed.

8.2 Motivation

There is much interest in applying BEEM to the antimonides due to the technological importance of the system [2, 3, 4, 5] and the unique properties of the various constituent materials. Compared to well known systems such as Au/Si and Au/$Al_xGa_{1-x}As$, the antimonides are distinctly under characterized by BEEM. To date, there have been few published BEEM results on antimonide heterostructures [1] Much of this is due to the experimental difficulty associated with the large BEEM background noise which arises from the type II band alignment and the small bandgaps of these materials. Because of this, the system remains largely unexplored and represents a stringent test ground for BEEM. A success here should yield a wealth of information and leave no doubt about the versatility and capability of the BEEM technique.

We have selected AlSb barriers and InAs/AlSb superlattices for this BEEM study

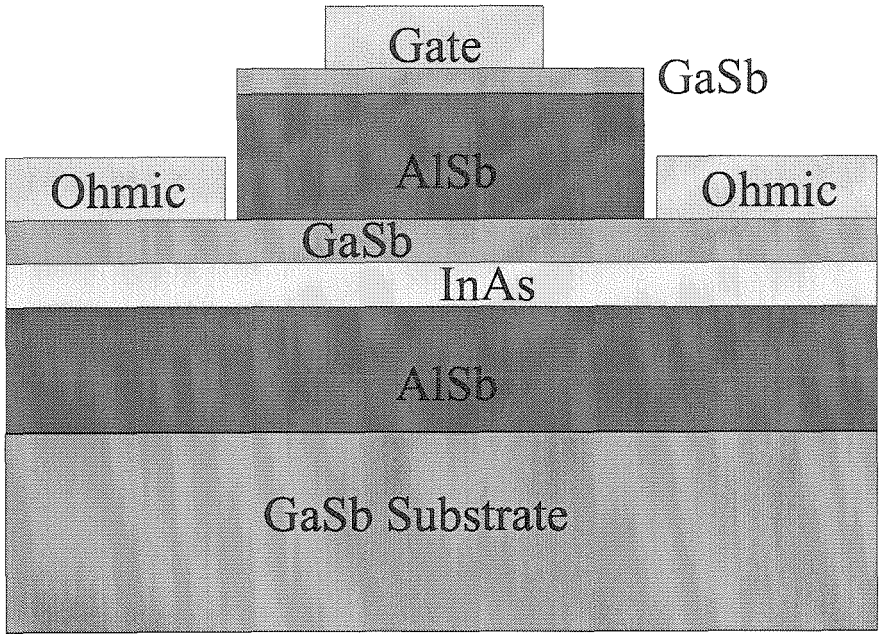

Figure 8.1: AlSb Schottky gate in dual channel mobility modulated transistor.

because these structures are highly relevant in current antimonide device research. Due to the lack of insulating oxide, AlSb is often used as the barrier in antimonide device structures. This has been demonstrated in the superlattice avalanche photodiode in Chapter 4 and the antimonide tunnel switch diode in Chapter 5. Another important example of this is the mobility modulated transistor [6] shown in Fig. 8.1, where AlSb is used as the gate insulator. This device is similar to a regular field effect transistor but employs a dual channel for conduction: InAs for electrons and GaSb for holes. Because the mobilities of the channels are vastly different (33000 cm^2/V-s for electrons in InAs and 850 cm^2/V-s for holes in GaSb), the conduction between the source and drain can be rapidly modulated by varying the field in the channel and changing the coupling between the channel wave functions. The device is in the on state when the wavefuctions are decoupled and the conduction is dominated by the fast InAs channel. It's turned off when the wavefuctions are coupled and the slow GaSb channel dominates the conduction. While this device is potentially interesting due to its fast switching speed, real world implementation has been problematic. One main reason is that the AlSb Schottky gate is very leaky [6, 7, 8]. It appears that the

Schottky barrier height of AlSb is lower than its bandgap would suggest.

This issue is ideally addressed by BEEM. The local Schottky barrier data from BEEM spectroscopy should make clear the dominating mode of transport in AlSb, i.e, whether the indirect X band edge contributes significantly to electron transport. As discussed in Chapter 2, such information is also highly relevant to the design of GaSb/AlSb superlattice avalanche photodiodes where electron ionization enhancement is critically dependent on the band offset differences within the superlattice [9].

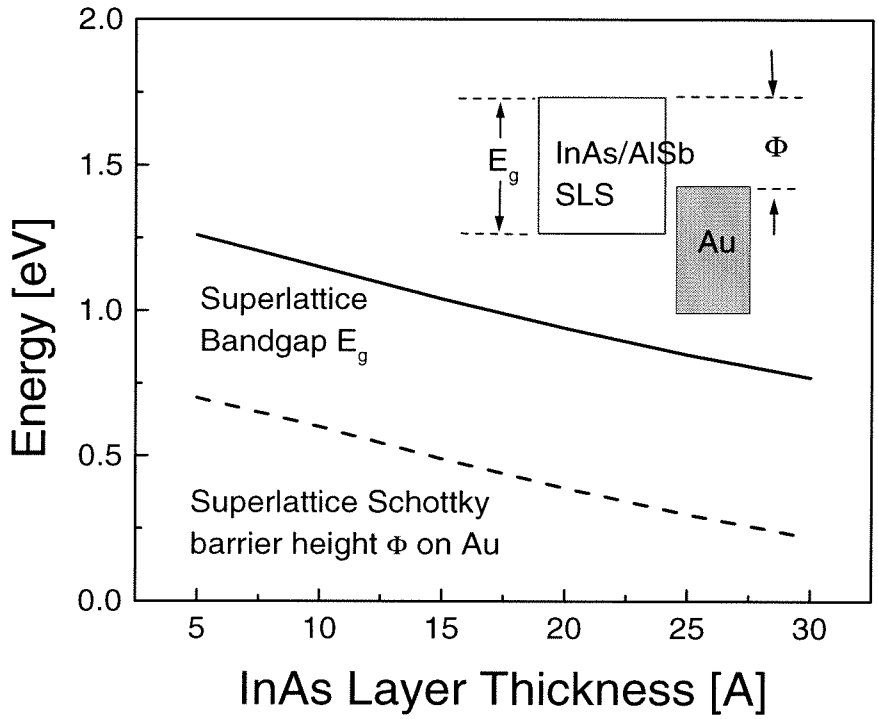

Figure 8.2: Calculated variation of InAs/AlSb superlattice bandgap and Schottky barrier height with InAs layer thickness [11].

The selectively doped InAs/AlSb superlattice is an interesting subject for BEEM study because of its heterostructure nature. To date, BEEM has not been used extensively to probe epilayers with a large number of hetero-interfaces. The properties of the superlattice and its application in antimonide avalanche photodiode have been described in detail in Chapters 3 and 4. As shown in Fig. 8.2, the bandgap and Schottky barrier height of the superlattice is readily tunable by adjusting superlattice

constituent layer thickness [10, 11]. In this study, InAs/AlSb superlattices of several different periods are examined. It is hoped that the resulting shift in band structure will be reflected in the BEEM data.

8.3 Sample Description and Preparation

The antimonide BEEM heterostructures examined in this study were all grown by molecular beam epitaxy. As shown in Fig. 8.3, the structure of the antimonide BEEM sample was similar to its $Al_xGa_{1-x}As$ counterpart. In the early phase of the study, a few AlSb epilayer samples were grown on highly doped p-type GaSb wafers. As will be discussed later, this resulted in unacceptably large background BEEM current. Hence subsequent samples were all grown on highly doped n-type (n=$5 \times 10^{17}/cm^3$ from Te doping) GaSb wafers. The high doping level ensured that the substrate would be conductive enough to support the collector current in the BEEM experiment (see Section 6.2.3).

Following oxide desorption under Sb over pressure, an unintentionally doped GaSb buffer layer was grown. Since the substrate was n-type and the background doping in the GaSb buffer layer was slightly p-type, the buffer layer was kept as thin as possible without compromising the growth quality of subsequent layers. At low growth rate, a 1000 Å thick buffer layer was found to be adequate. At the end of the buffer growth, samples were soaked in Sb, yielding the (1×3) reflection high energy electron diffraction (RHEED) pattern characteristic of reconstructed GaSb surface.

For AlSb studies, a 500 Å layer of unintentionally doped AlSb was grown over the smoothed GaSb surface. The thickness was selected so that bulk properties would be examined while at the same time the layer was thin enough to support transport of BEEM current. Because the AlSb layer was relatively thin, substrate temperature was kept at 520 °C, the same as for GaSb growth. RHEED for the AlSb layer was less streaky but still exhibited the characteristic 1×3 pattern. To prevent AlSb oxidation, samples were capped off at the end of the growth by either a 50 Å GaSb layer or a 100 Å InAs layer. Substrate temperature was lowered to 470 °C during growth of the

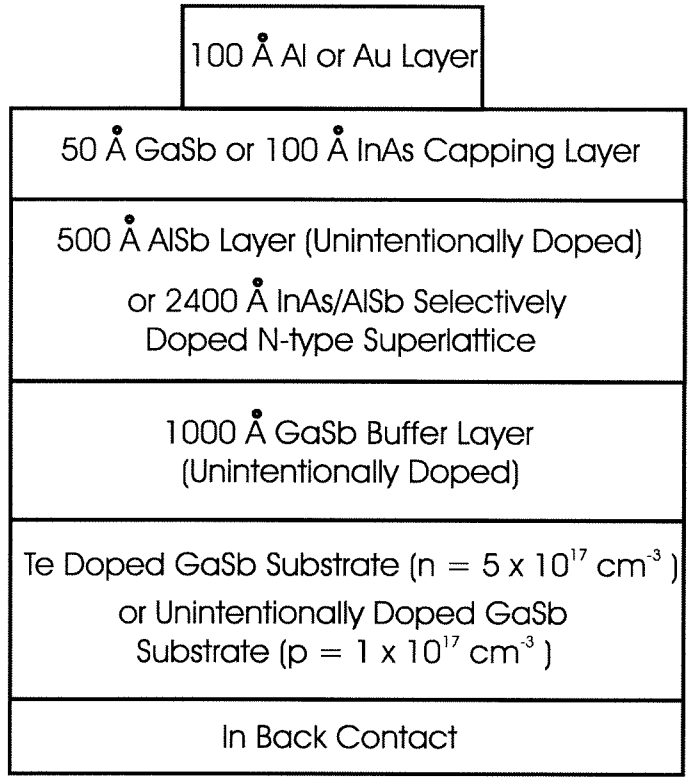

Figure 8.3: Structure of antimonide BEEM sample.

InAs capping layer.

For InAs/AlSb superlattice studies, the superlattice epilayer were grown following the recipe outlined in Chapter 3. The substrate temperature had to be lowered to prevent excessive As incorporation in the antimonide layers. The structural quality of the superlattice was significantly improved when the growth temperature was lowered to 420 °C, at which point the GaSb surface turned Sb rich and the RHEED pattern changed from 1×3 to 1×5. During growth of the InAs constituent layer, the Si dopant cell shutter was opened, and As flux was minimized by using the valved cracker while maintaining an As stabilized growth front. A 10 second Sb soak was applied between each InAs and AlSb interface to ensure a InSb like interface, which is known to produce material of superior quality [12]. RHEED pattern remained streaky throughout the growth and exhibited sharp 2×4 and 1×3 reconstructions for the InAs and AlSb layers, respectively. Samples were grown with superlattice periods of 17Å, 24 Å, and 48 Å. The period thickness was split between the InAs and AlSb

layer to better balance the compressive and tensile strain in these layers. The total thickness of the superlattice was kept constant for all samples at 2400 Å. To prevent oxidation, the superlattice was capped with 50 Å of GaSb following completion of the last AlSb layer.

Similar to the $Al_xGa_{1-x}As$ study, the sputter-etch deposition tool was used for post growth metalization. Aluminum and gold were sputtered off solid targets by Ar plasma and deposited onto the sample at rates up to 0.4 Å/sec, which resulted in arrays of metal dots 1 mm^2 in area, and up to 100 Å in thickness. Indium left over from growth served as the back contact. The surface of the front contact metal layer was comparable to that of $Al_xGa_{1-x}As$ samples, and appeared to be smooth and suitable for BEEM studies. Prior to metalization, samples were taken out of the UHV growth environment and exposed to the ambient. Hence the top 20 - 30 Å of the cap layer was oxidized. The native oxide may have stabilized the surface since the samples yielded the same characteristics after storage of up to several weeks. To minimize contamination from handling, the samples were subjected to a sequential ultra sonic rinse in acetone, isopropanol and de-ionized water before being introduced to the metalization chamber, as in the $Al_xGa_{1-x}As$ BEEM study.

8.4 Results from AlSb Study

8.4.1 Effect of Sample Configuration

As discussed in Section 6.2.3, in order to read the minute BEEM signal, it is necessary to have a large junction resistance across the metal to semiconductor interface at zero bias so that noise current due to micro-volt fluctuation in the system is suppressed. This was not a problem in the $Al_xGa_{1-x}As$ study because the Schottky barrier height of $Au/Al_xGa_{1-x}As$ was relatively large (greater than 0.8 eV). In antimonide BEEM samples, the junction may be too conductive due to the type II band alignment and the narrow bandgap of GaSb. To determine the conductive characteristics of samples with different configurations and examine their suitability for subsequent

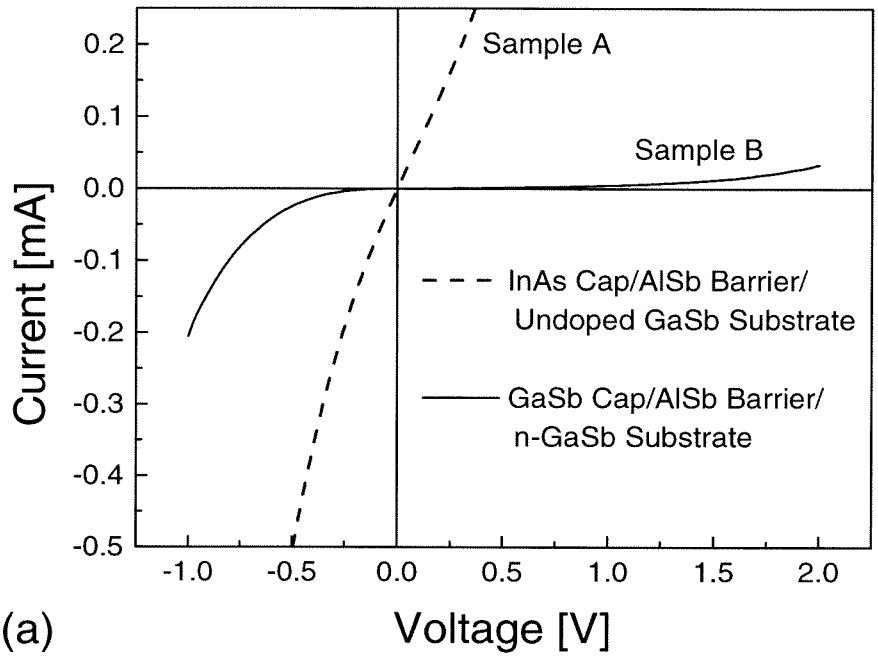

(a)

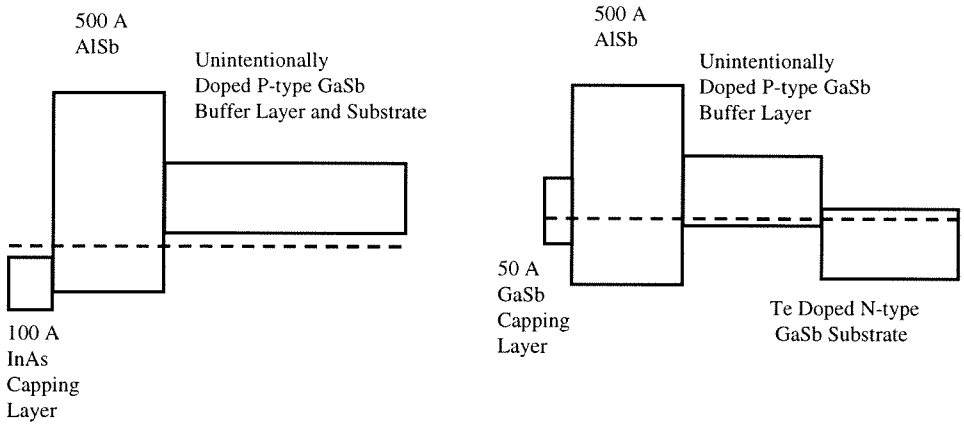

Sample A Sample B

(b)

Figure 8.4: (a) I-V characteristics of two types of AlSb BEEM samples. Mesa size was 1 mm. (b) Corresponding band diagrams.

BEEM experiment, I-V measurements were taken from these samples prior to the BEEM study.

Figure 8.4(a) shows the results from two types of AlSb samples. Sample A was from an early growth on unintentionally doped p-type GaSb substrate and capped by an InAs layer. Sample B was grown on n-type GaSb substrate and capped by GaSb, which was the standard configuration for most AlSb samples and all superlattice samples. The band diagrams of these samples are shown in Fig. 8.4(b). It can be seen from Fig. 8.4(a) that sample A was much more conductive than sample B. This is because the AlSb barrier did not effectively block the tunneling current that resulted from the type II band alignment between InAs and GaSb. In sample B, tunneling was reduced due to the absence of InAs layer and the blocking action of the underlying n-type substrate. When sample A was inserted in the BEEM setup, a large background BEEM current was observed, completely overwhelming the collector signal and rendering the device unsuitable for BEEM study. This was not surprising considering the steep slope of the sample A I-V curve at zero bias. By contrast, the BEEM background current was much smaller in sample B due to its larger resistance at the origin.

8.4.2 BEEM Characterization

Despite the improvement in BEEM noise current, sample B was still too noise and too unstable for BEEM imaging. However, BEEM spectroscopy was readily obtained from AlSb samples with the B type configuration. Figure. 8.5(a) shows two such BEEM I-V curves. Each curve was taken from a different place on the sample surface and took approximately 10 seconds to generate. Tip drift rates were about a few nm per minute after the system was given time to equilibrate. Since there was large variation from one run to another, BEEM scans were not averaged in order to preserve spatial resolution in the experiment.

The BEEM I-V curve was analyzed by using the parabolic turn on model [13],

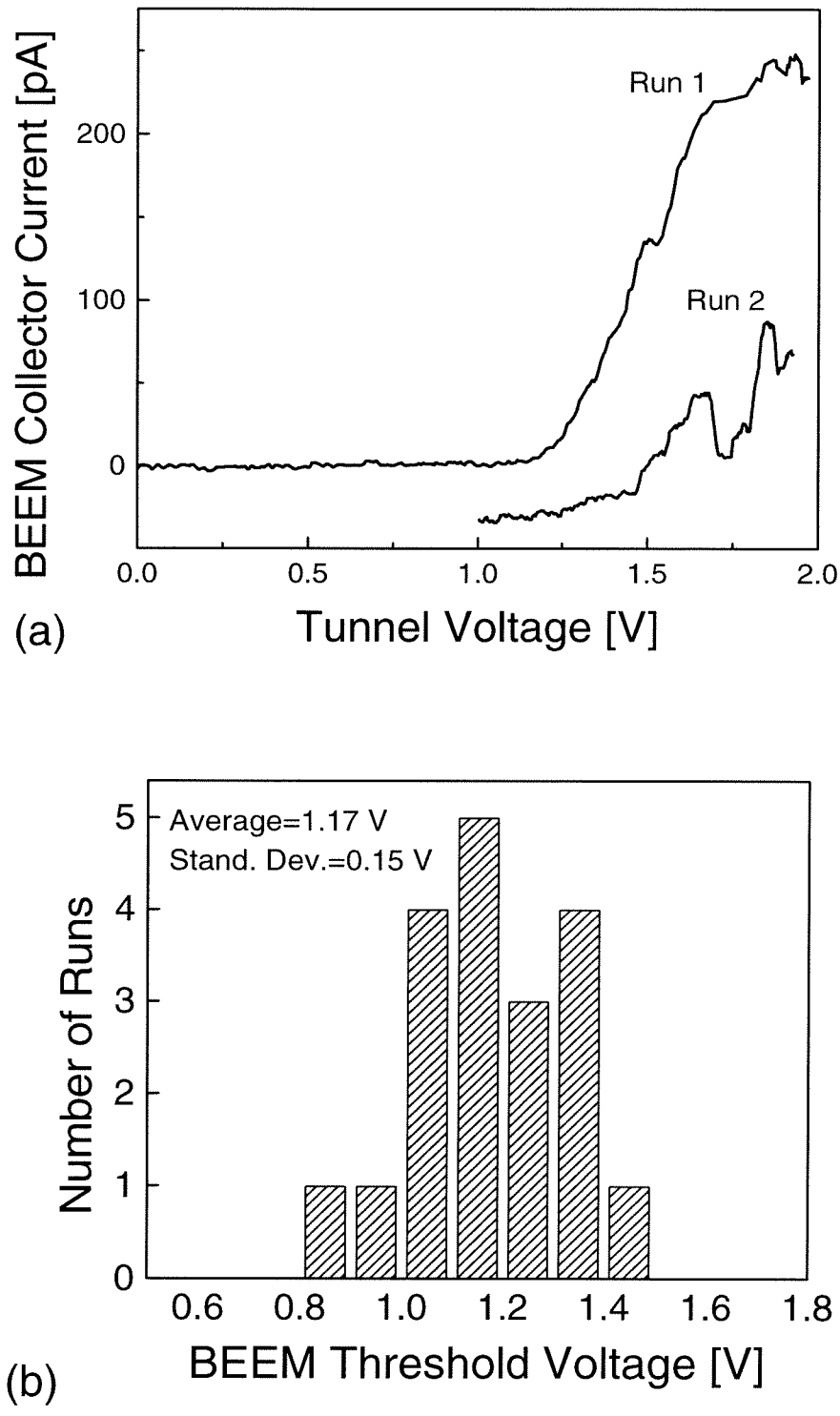

Figure 8.5: (a) BEEM I-V curves for AlSb samples. The tunneling current was held constant at 10 nA. (b) BEEM threshold statistics.

which assumes that the BEEM threshold behavior takes on the form

$$I_c = \sum_{i=1}^{n} (V - V_i)^2 \tag{8.1}$$

Where I_c is the BEEM collector current, V is the tunnel voltage and V_i is the threshold voltage. By examining a large number of runs, it was found that the turn on voltage centered around 1.17 eV with a standard deviation of 0.15 eV. This was in fair agreement with the result obtained by Walachova et al [1] in their study of InAs/AlSb double barrier heterostructures. The band structure of AlSb is shown in Fig. 8.6. It can be seen that the BEEM turn on threshold should be attributed to the conduction band minimum near the AlSb X point, whereas the L and Γ point of AlSb lie higher and could not be delineated from the BEEM data. This indicates that electron transport in AlSb was dominated by the indirect band minima. Hence the electron barrier height of AlSb was much lower than that given by the Γ point. This is an important result and has many implications in antimonide device research. In particular, electron ionization enhancement in GaSb/AlSb superlattices depend critically on the conduction and valance band offset difference between GaSb and AlSb. The smaller conduction band offset implied by the BEEM result means that the ionization enhancement effect will be weaker than previously thought.

As shown in Fig. 8.5(b), there was significant variation among the individual BEEM I-V curves. The large variation in individual BEEM threshold indicated unevenness at the metal semiconductor interface. This is in contrast with BEEM study of AlAs, where the BEEM turn on voltage exhibited minimum variation across the wafer (see Section 7.5.4). Since transport across a barrier varies exponentially with the barrier height, the I-V characteristics over a large area is dominated by regions with small local barriers. Hence the large spread in the AlSb BEEM threshold was consistent with the fact that the barrier height in AlSb Schottky structures was often lower than expected.

It should be noted that the BEEM current background noise in the AlSb sample was on the order of 5 pA, which was higher than similarly prepared AlAs samples

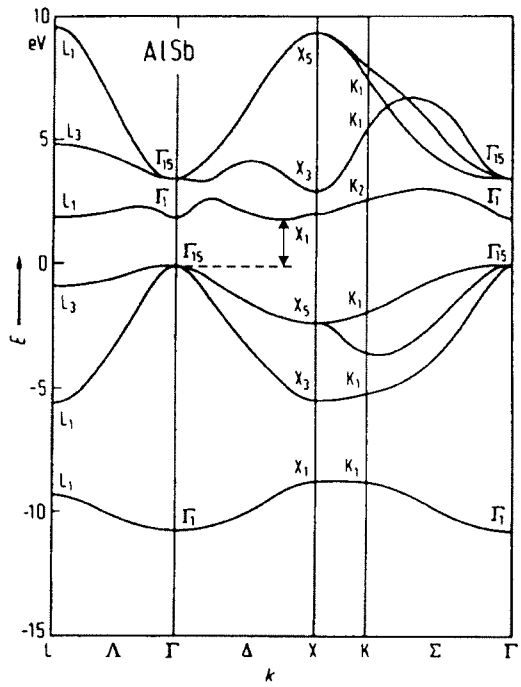

Figure 8.6: Band structure of AlSb.

even through the barrier height in both systems was about 1.2 eV. We attribute this discrepancy to the fact that the background doping was p-type for AlSb and n-type for AlAs. The increased background BEEM current was accounted for by additional hole thermionic emission over the smaller hole barrier height of AlSb. The dominance of hole current was evident in the I-V response of the sample to ambient light.

8.5 Results from Superlattice Study

8.5.1 Effect of Superlattice Period

Background noise was also a significant problem in BEEM spectroscopy of InAs/AlSb superlattices. This is because the effective superlattice bandgap is substantially smaller than that of AlSb, even for samples with a very short period. The smaller bandgap of the superlattice epilayer led to reduced Schottky barrier height at the metal to semiconductor interface. As the result, the BEEM noise current was not adequately suppressed due to the small zero-bias resistance of junction.

The superlattice structures fabricated for this study had InAs/AlSb period thicknesses of 8 Å/9 Å, 12 Å/12 Å, and 24 Å/24 Å. As shown in Fig. 8.2, the corresponding bandgaps were 1.2 eV, 1.15 eV, and 0.88 eV, and the expected Schottky barrier height of Au/superlattice structure were 0.62 eV, 0.56 eV, and 0.32 eV, respectively. The bandgaps and Schottky barrier heights could be made larger by growing structures with shorter superlattice period, but the structural quality of the material deteriorated rapidly as the superlattice period was decreased. In fact, X-ray rocking curves for samples with the 8 Å/9 Å configuration showed multiple splits at the superlattice peak, indicating that the layer had relaxed from too much strain. The inferior quality of these samples rendered them unsuitable for BEEM studies. The 24 Å/24 Å longer period sample exhibited the best structural integrity but its bandgap and Schottky barrier heights were too small to keep background BEEM current at a reasonable level. Thus only the 12 Å/12 Å period samples was deemed suitable for BEEM experiments.

8.5.2 Results from 12 Å/12 Å, InAs/AlSb Superlattice

Figure 8.7 shows a high resolution X-ray diffraction scan of the 12 Å/12 Å period superlattice. The sharp X-ray diffraction satellites were indicative of the good structural quality achieved. The I-V curve of the metalized device is shown in Fig. 8.8 and indicated that the underlying superlattice was n-type. The curve deviated significantly from ideal Schottky diode behavior at high voltages. But the low voltage portion of the curve yielded a Schottky barrier height of 0.6 eV [14].

When these samples were inserted in the BEEM set-up, the background BEEM current noise was on the order of 100 pA, which overwhelmed any conventional BEEM signal that would be present. Due to the large noise and the associated instability, BEEM images could not be obtained. However, it was found that after the surface was stressed by running a high voltage and current (-3 V and 50 nA) through the STM tip, the metal layer could be deformed resulting in regions where the metal layer was tenuous. When the STM tip was placed over these regions, thresholds

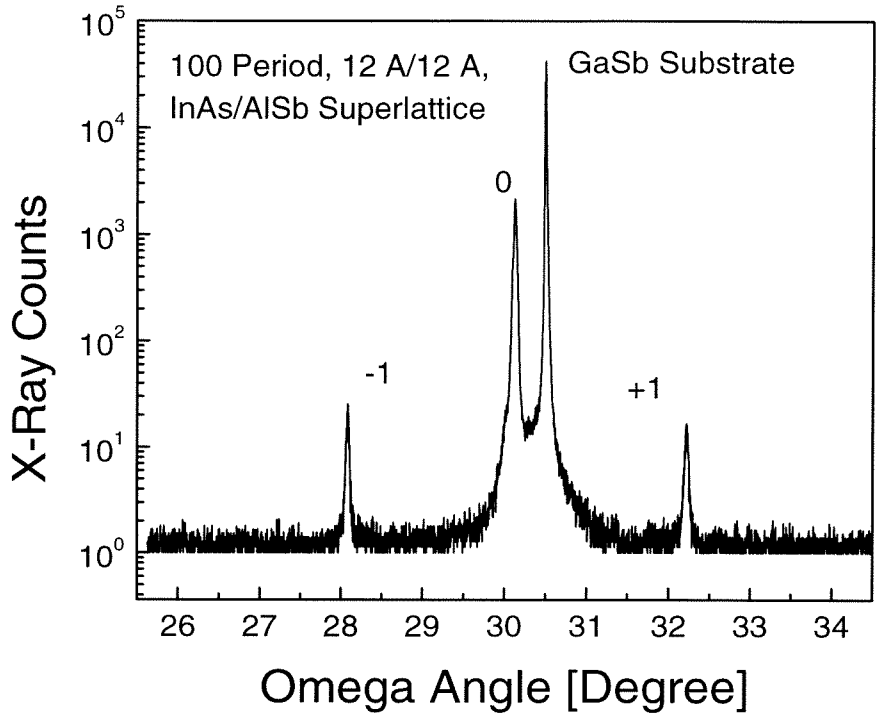

Figure 8.7: High resolution X-ray diffraction scan from the 12 Å/12 Å, InAs/AlSb superlattice BEEM sample.

could be observed in the BEEM spectroscopy curve. Figure 8.9 shows some typical BEEM scans after the stress treatment. The threshold occured at around 0.8 eV for the Au/superlattice system and could be reproduced by retracting the STM tip and using it to stress a new region.

8.6 Summary and Conclusion

We have applied BEEM techniques to the InAs/GaSb/AlSb material system. Due to the large background noise, BEEM images were not obtained. However, BEEM spectroscopy was applied with various degrees of success to analyze the Schottky barrier height and band structure of AlSb barriers and InAs/AlSb superlattices.

The Al/AlSb system yielded a BEEM threshold of 1.17 eV, which was attributed to transport through the conduction band minimum near the AlSb X point. This indicates that the low lying, indirect band edge of AlSb contributes significantly to

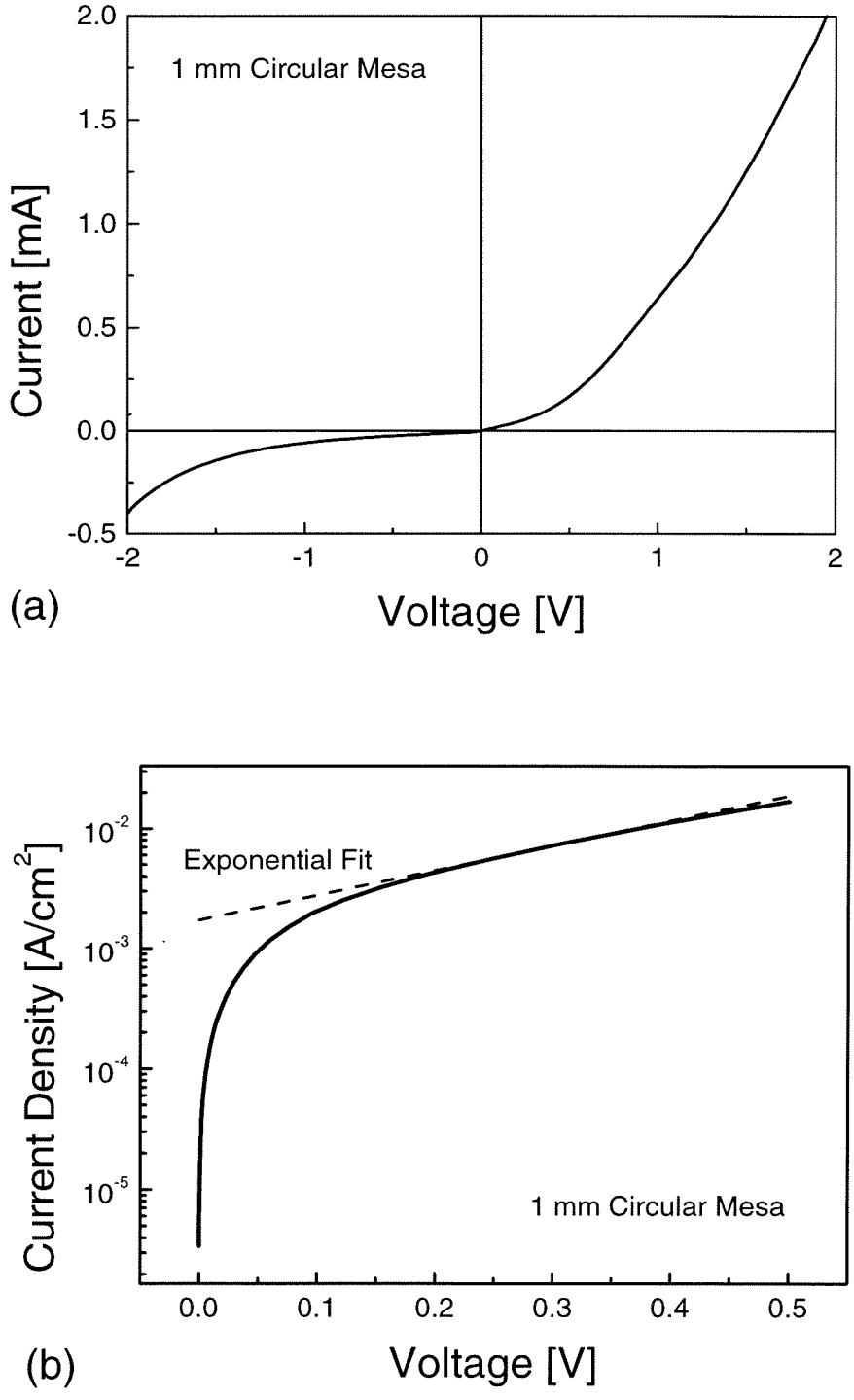

Figure 8.8: Current-voltage characteristics of 12 Å/12 Å, InAs/AlSb superlattice BEEM samples. (a) Liner plot. (b) Extraction of Schottky barrier height from Log plot.

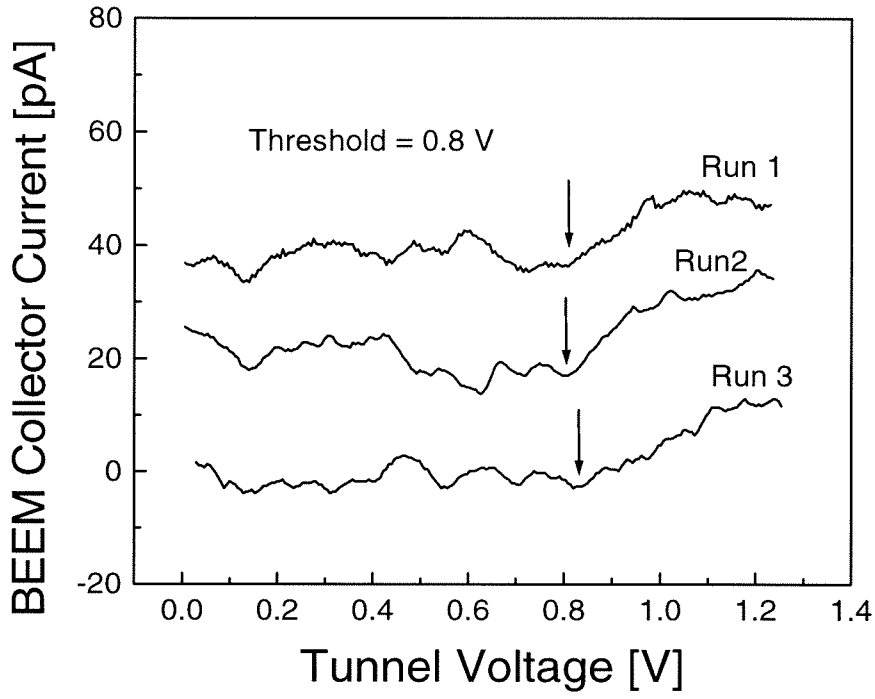

Figure 8.9: BEEM spectroscopy curves from 12 Å/12 Å, InAs/AlSb superlattice sample. Tunnel current was held constant at 10 nA.

electron transport and must be accounted for in device design. A large spread in the AlSb BEEM threshold (0.2 eV) was also observed, indicating degradation of the AlSb barrier due to local fluctuations at the metal semiconductor interface. The finding is consistent with the fact that the observed Schottky barrier height is often lower than expected.

In the case of selectively doped n-type superlattice, BEEM spectroscopy was hampered by considerable background BEEM current due to the small bandgap and low Schottky barrier height of the superlattice. The expected shift in BEEM threshold from superlattices of different period could not be observed, and BEEM scans yielded a threshold of 0.8 eV for the Au/24 Å period superlattice system only after considerable stressing of the metal layer.

The important issue in BEEM study of antimonides appear to be the large background current associated with the type II band alignment and small bandgaps of these materials. The problem may be partially rectified through careful design of

the surface capping layer and the underlying substrate in the antimonide BEEM structure. In particular, the junctions formed by InAs cap/thin AlSb barrier/p-GaSb were found to be especially leaky, whereas the GaSb cap/thin AlSb barrier/n-GaSb configuration yielded working BEEM samples.

Bibliography

[1] J. Walachova, J. Zelinka, J. Vanis, D. H. H. Chow, J. N. Schulman, S. Karamazov, M. Cukr, P. Zich, J. Kral, and T. C. McGill, *Appl. Phys. Lett.* **70**, 3588 (1997).

[2] H. Lee, P. k. York, R. J. Menna, R. U. Martinelli, D. Z. Garbuzov, S. Y. Narayan, and J. C. Connolly, *Appl. Phys. Lett.* **66**, 1942 (1995).

[3] R. H. Miles, D. H. Chow, Y-H. Zhang, P. D. Brewer, and R. G. Wilson, *Appl. Phys. Lett.* **60**, 1921 (1995).

[4] D. H. Chow, R. H. Miles, C. W. Nieh, and T. C. McGill, *J. Cryst. Growth* **111**, 683 (1991).

[5] D. H. Chow, H. L. Dunlap, W. Williamson, III, S. Enquist, B. K. Gilbert, S. Subramaniam, P.-M. Lei, and G. H. Berstein, *IEEE Electron Device Lett.* **17**, 69, (1996).

[6] E. S. Daniel, Thesis, California Institute of Technology, 1997.

[7] M. Drndic, M. P. Grimshaw, L. J. Cooper, and D. A. Ritchie, *Appl. Phys. Lett.* **70**, 481 (1997).

[8] M. J. Yang, F.-C. Wang, C. H. Yang, and B. R. Bennett, and T. Q. Do, *Appl. Phys. Lett.* **69**, 85 (1996).

[9] G. F. Williams, F. Capasso, and W. T. Tsang, *IEEE Electron Device Lett.* **3**, 71 (1982).

[10] D. H. Chow, Y. H. Zhang, R. H. Miles, and H. L. Dunlap, *J. Cryst. Growth* **150**, 879 (1995).

[11] J. N. Schulman and R. H. Miles, unpublished.

[12] G. Tuttle, H. Kroemer, and J. H. English, *J. Appl. Phys.* **67**, 3032 (1990).

[13] L. D. Bell and W. J. Kaiser, *Phys. Rev. Lett.* **61**, 2368 (1988).

[14] *S. M. Sze, Physics of Semiconductor Devices*, John Wiley Sons. Inc., 1981.